Summer 2020

SYNTHESIS OF CARBIDE CERAMICS VIA REDUCTION AND CARBURIZATION OF OXYANIONS ADSORBED ONTO AN ACTIVATED CARBON MATRIX

Grant Wallace

SYNTHESIS OF CARBIDE CERAMICS VIA REDUCTION AND
CARBURIZATION OF OXYANIONS ADSORBED ONTO AN ACTIVATED
CARBON MATRIX

by

Grant Wallace

A dissertation submitted in partial fulfillment of the

requirements for the degree of

Doctor of Philosophy:

Materials Science

Montana Technological University

2020

SYNTHESIS OF CARBIDE CERAMICS VIA REDUCTION AND CARBURIZATION OF OXYANIONS ADSORBED ONTO AN ACTIVATED CARBON MATRIX

By

GRANT CURTIS WALLACE

B.S. Chemistry, Centre College, Danville, Kentucky, 2012
M.S. Metallurgical and Mineral Processing Engineering, Montana Technological University, Butte, Montana, 2015
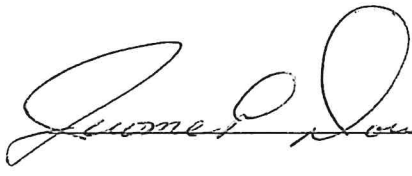
Dissertation
presented in partial fulfillment of the requirements
for the degree of

Doctor of Philosophy
in Materials Science

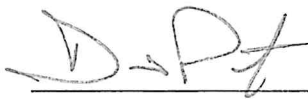Montana Technological University
Butte, MT

August 2020

Approved by:

_____ 29-Jul-20
Jerome Downey, Ph.D. P.E., Chair
Metallurgical and Materials Engineering Dept.

Paul Gannon

_____
Paul Gannon, Ph.D.
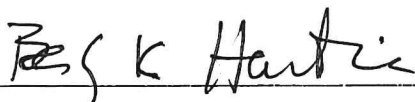Chemical and Biological Engineering Dept., Montana State University

_____ 2020/7/28
Dario Prieto Ph.D.
Mechanical Engineering Dept.

_____ 29 July 2020
K.V. Sudhakar, Ph.D. P.E.
Metallurgical and Materials Engineering Dept.

_____
Larry Twidwell, D.Sc., Professor Emeritus
Metallurgical and Materials Engineering Dept.

_____
Beverly K. Hartline, Dean
Montana Technological University Graduate School

Wallace, Grant, Materials Science Doctor of Philosophy, 2020

Synthesis of Carbide Ceramics via Reduction and Carburization of Oxyanions Adsorbed onto an

Activated Carbon Matrix

Chairperson: Jerome P. Downey

Carbide ceramics rank high among the hardest and most chemically resistant materials. Their ability to resist physical and chemical attack under conditions where more traditional materials fail make them very desirable for a number of industrial applications. Their use is limited, however, due to the expensive and energy-intensive methods required to produce them commercially.

A more versatile and energy-efficient process for commercial carbide production has been developed by synthesizing micron/sub-micron carbide ceramic particles through the adsorption and subsequent carburization of anions on an activated carbon matrix. Oxyanion solutions containing sodium tungstate, sodium molybdate, or sodium metasilicate are adsorbed onto activated carbon to produce anion-loaded precursors. These precursors are carburized in the presence of a reducing atmosphere consisting of hydrogen, carbon monoxide, and methane to produce carbide crystals on the activated carbon surface. In this study, tungstate (WO_4^{2-}), molybdate (MoO_4^{2-}), and silicate (SiO_3^{2-}) anions were evaluated. Silicon carbide (SiC) whiskers and mixed crystals of tungsten carbide (WC), tungsten semicarbide (W_2C), and tungsten (W) were formed via carbothermal reduction using inert and reducing gas atmospheres at temperatures much lower than current commercial practice. Mixed crystals of WC, W_2C, and W were synthesized at 950 °C under an atmosphere of 80% CH_4, 10% H_2, and 10% CO. Molybdenum carbide (Mo_2C) was synthesized at temperatures as low as 850°C under an atmosphere consisting of 80% CH_4, 10% CO, and 10% H_2. Under optimal conditions, conversion to Mo_2C and WC exceeded 90%. SiC was synthesized at temperatures as low as 1200 °C under H_2. Separation of the WC/W_2C/W crystals from the activated carbon matrix has been demonstrated using surfactant-aided density separation methods.

Response surface modeling was used to determine optimal conditions for tungstate, molybdate, and silicate adsorption as well as the optimal carburization conditions for the W-loaded and Mo-loaded precursors. Results show that the carburization process is feasible and that it is possible to mathematically model and statistically optimize the production and carburization of the activated carbon precursors.

Keywords: Carbide Synthesis, Carbide Ceramics, Statistical Modeling,

Dedication

To Greer for all of her love and support, as well as all of my friends and family who have been there for me along the way.

Acknowledgements

I would like to thank my advisor, Dr. Jerry Downey, for all of his advice and support during my time in the MUS Materials Science Ph.D. Program. I would also like to thank the members of my committee: Dr. Dario Prieto, Dr. K. V. Sudhakar, Dr. Larry Twidwell, and Dr. Paul Gannon. Thank you all for being a part of this process. I would also like to thank Gary Wyss for all of his help with the characterization equipment as well as Dr. Rick LaDouceur and Dr. Larry Twidwell for helping with the statistical analysis of my data. I also need to thank Dr. David Hutchins and Katie Schumacher who were not only great officemates, but who also helped extensively with building and troubleshooting the furnace apparatus I used for much of my carburization work. I also need to thank Jan Chorney for all of her help in the lab as well as her work on all of the reports that were sent to the Army Research Laboratory as part of this work. I am also grateful to Trenin Bayless for his work on the separation work affiliated with this project, as well as Liz Raiha, Auva Speiser, Maureen Chorney, and Daisy Margrave who have continued much of my work as they pursue their graduate degrees. I also want to thank all of the undergraduate research assistants who helped me gather the data used in this project: Alaina Mallard, Liz Raiha, Auva Speiser, Marc D'Aberle, Xavier Vorhees, and Hayden Hammontree. Without the help of all of these students in the lab, I would not have been able to accomplish all that I have presented in this work. Special thanks go to my friend Scott Gibson for some unusual mechanical repairs as well as all of the small projects, and time spent at the guitar shop that kept me sane. Lastly, I would like to thank my former undergraduate advisor, Dr. Preston Miles, for setting me on the path that led me to Butte and Montana Tech in the first place.

Table of Contents

List of Tables

List of Figures

List of Equations

1. Introduction

Ceramic carbides include a wide range of materials that vary greatly in terms of structure and properties. Metal carbides are some of the hardest materials in existence and certain metal carbides, such as tungsten carbide (WC), possess hardness values approaching that of diamond as well as being resistant to wear and chemical attack at relatively high temperatures. Because of their ability to resist corrosion and abrasion, carbides are uniquely applicable to a number of industrial applications where traditional metals and alloys do not perform as well. Such applications include high-temperature cutting tools, drill bits, surgical implements, and alloying agents [1]. Due to their brittle nature, metal carbides are mixed with a softer metal binder, usually cobalt, to produce sintered parts. These carbide-cobalt materials are commonly referred to as hardmetals or cemented carbides.

Other ceramic carbides, such as silicon carbide (SiC) and boron carbide (B_4C), are also characterized by extremely high hardness and wear resistance. Despite their similarities to the hardmetals in terms of mechanical properties, they differ greatly in terms of their physical/chemical structure. While hardmetals generally consist of an interstitial compound of metal and carbon, silicon carbide is a covalently bonded structure [1].

Current methods of producing ceramic carbides are energy intensive. Most carbides are produced at relatively high temperatures (>1500°C) by reacting metals or oxide powders with a source of carbon. Extensive milling operations are typically required to reduce the carbides into a fine powder for further use [1].

1.1. Interstitial Carbides

Interstitial carbides are produced by introducing carbon atoms as inclusions into a metal lattice. Transition metal atoms, particularly Group VI elements, have significantly larger atomic

radii than the carbon atoms which enables the carbon atoms to enter the metal lattice without inducing excessive strain. Although some degree of covalent bonding exists between the metal and carbon atoms, metallic bonding behavior is dominant [2]. Because of the interstitial carbon inclusions, non-stoichiometric carbide compounds can form during carburization to produce metastable secondary carbides. The resulting stable carbide species is directly related to the amounts of carbon and metal that are present during carburization.

1.1.1. Tungsten Carbide (WC)

Since its first synthesis by Moissan in 1893 [3], WC has been valued for its high hardness and its ability to resist abrasion and chemical attack at elevated temperatures. The hexagonal WC crystal structure differs from the cubic crystal structure of elemental tungsten due to the diffusion of carbon into the interstices between tungsten atoms during carburization. Implementation of hardmetals into cutting and drilling tools has increased the lifespan of these tools dramatically when compared to similar tools made of steel [4]. Examples of the chemical, physical, and mechanical properties of WC are presented in Table I.

Table I: Properties of WC [4]

Property	Value Range	Units
Density	15.25-15.88	g/cm^3
Melting Point	2,727-2,920	°C
Compressive Strength	3.35-6.83	GPa
Hardness	17.0-36.0	GPa
Young's Modulus	600-686	GPa
Poisson's Ratio	0.2-0.22	-

Because of these properties, WC-based hardmetal are used extensively in the wear parts of cutting and drilling tool industries, and demand for WC is projected to continue increasing over the next decade [5]. Global production of tungsten metal was 76,400 tons in 2012; however, global production values are difficult to report as most tungsten producers in the United States

have elected to withhold production values [6]. Research has also shown that tungsten carbides possess catalytic properties. Tungsten carbides have been shown to have catalytic abilities that are comparable to precious metal catalysts such as platinum and palladium, making carbides a more economical option for the catalysis of numerous chemical reactions [7]–[10].

In commercial tungsten carbide production, tungsten oxide powders are first reduced under a hydrogen (H_2) atmosphere at temperatures ranging from 700 $^{\circ}$C to 900 $^{\circ}$C to form elemental tungsten powder. The tungsten powder is mixed with carbon and heated under H_2 again at significantly higher temperatures (1400-1600 $^{\circ}$C) to convert the tungsten powder into tungsten carbide. Finally, the tungsten carbide powder is crushed, ground, and sieved to produce commercial tungsten carbide powder [11]. Carbide powders with different particle size distributions are produced depending on the intended application. In the case of WC-Co hardmetal, submicron particle sizes are desired in many applications as it has been shown that the hardness and abrasive resistance of sintered parts composed of WC hardmetal improve as the WC particles decrease in size [12].

Research has shown that the application of reducing gases, especially carbon-containing reducing gases, can significantly reduce the temperature at which carburization occurs [13]. In addition to providing the reducing conditions that facilitate the carburization process, carbon-containing reducing gases also act as a carbon source for the carburization reaction. This behavior improves the carburization reaction kinetics by allowing solid-gas reactions to occur simultaneously with the slower solid-solid carburization reaction between the solid carbon source and the non-carbon solid material being used to form the carbide of interest. Reducing gas atmospheres have been implemented in multiple WC synthesis routes with various W sources used to produce WC and WC-Co hardmetal powders. Solid tungsten oxides have been converted

to WC under CH_4/H_2 at temperatures below 1000 °C [14]–[17][14]. Other tungsten compounds, such as ammonium paratungstate (APT) and tungsten blue oxide ($WO_{2.90}$), were also used with mixtures of CH_4 and H_2 to synthesize WC at 850 °C [18]. Tungsten oxide (WO_3) was also found to produce WC in the presence of carbon monoxide (CO) at temperatures as low as 700 °C [19].

Powder metallurgy methods, such as spray drying and chemical vapor deposition, have been used in conjunction with carburizing gas atmospheres to produce nanocrystalline WC and WC hardmetal powders [20]–[22]. These synthesis routes have used a number of W-based precursors including tungsten chlorides (WCl_6 and WCl_4) [23], [24] and tungsten hexacarbonyl ($W(CO)_6$) [25].

The use of aqueous solution precursors has also shown promise in synthesizing nanocrystalline and submicron WC powders. Often with these solution-based routes, the synthesized WC is supported on a substrate although some studies have synthesized WC-Co powders from solutions containing C, W, and Co without the use of a carbon substrate [26]. However, these synthesis routes require multiple drying stages before carburization can occur. Yan, et al. synthesized WC supported on graphitized carbon by adsorbing tungsten onto an ion exchange resin from a solution of ammonium metatungstate and potassium ferrocyanide. The resin was then carburized at 650-800 °C to produce WC supported on carbon [27]. Zawrah was also able to synthesize WC-Co nanocomposites by dissolving tungstic acid and cobalt nitrate in ammonium hydroxide and nitric acid. The solution was dried and decomposed before being dispersed in a solution containing polyacrylonitrile and the dried product was carburized at 900-1000 °C under an Ar/H_2 atmosphere [11].

Carbon-supported WC was also synthesized by a vapor phase impregnation method by Hugot, et al. By this method, a mixture of WC, W_2C, and W particles were synthesized on a carbon support at 800-950 °C in a CH_4/H_2 using WCl_6 as a tungsten source [28].

1.1.2. Molybdenum Carbide (Mo_2C)

Another interstitial metal carbide, Mo_2C is very similar to WC in its chemical, physical, and mechanical properties. Similar to WC, Mo_2C has a hexagonal crystal structure and is formed from the diffusion of carbon atoms into the interstices of the Mo metallic network. Molybdenum carbide can take on an alternative orthorhombic crystal structure that is only stable at temperatures above 1475 °C [2]. It is also characterized by high hardness values and abrasion resistance. A collection of the chemical, physical and mechanical properties of Mo_2C are presented in Table II.

Table II: Properties of Mo_2C [2], [29]

Property	Value Range	Units
Density	8.20	g/cm^3
Melting Point	2,505-2,692	°C
Compressive Strength	901	MPa
Hardness	15.5-24.5	GPa
Young's Modulus	535	GPa

Molybdenum carbide is sometimes used in place of WC to form cemented carbides and carbide coatings for cutting tools and wear parts. It is also used as a hardening agent in Mo-alloy steels as it is formed during the steelmaking process [2]. Aside from their capabilities as a structural materials, molybdenum carbides have also shown promise as less-expensive catalysts for a number of chemical processes including hydrogen evolution [30]–[32], hydrogenation [33], [34], and hydrodesulfurization [35]–[37]. Molybdenum compounds have been used as catalysts in the form of pure carbide powders [38] as well as a constituent of composite materials where

the carbide catalysts are supported on a structure of alumina (Al_2O_3) [32], [35] , silica (SiO_2) [32], [39], or carbon [40].

Commercially, Mo_2C is synthesized by the direct carburization of blended Mo and C powders under H_2 at temperatures exceeding 1500 °C [2]. However, much like the process currently used to produce WC, this synthesis route tends to produce a coarse final product that does not possess the small particle sizes desired for producing sintered products or the high surface areas required for catalytic use. Catalysis researchers have developed a number of alternative synthesis routes to produce molybdenum carbide. The most commonly used method of synthesizing Mo_2C for catalysis has been the temperature-programmed reduction (TPR) method where a molybdenum source, typically MoO_3 or MoO_2, is subjected to a reducing/carburizing gas atmosphere at elevated temperatures. Variations on the TPR method have been used with different gas atmospheres and Mo sources. Lee, et al. synthesized Mo_2C from 0.5 g samples of MoO_3 using TPR with a H_2/CH_4 gas atmosphere consisting of varying amounts of CH_4 at temperatures below 930 K [38]. Nanocrystalline Mo_2C was also synthesized by Covington, et al. from MoO_3 using both CH_4/H_2 and CO/H_2 atmospheres with the TPR method. Carburization temperatures for this method ranged from 950-1050 °C and resulted in macrocrystal "flakes" of Mo_2C being formed with crystallite measurements reported by XRD analysis to be below 10 nm [41]. Other variations of the TPR method have been performed using other hydrocarbon gases such as propane [36] and ethane [33]. Variants on the TPR method have used ammonium heptamolybdate as a solid precursor to synthesizing Mo_2C at approximately 600 °C [36], [42], [43].

The use of solution chemistry in the production of Mo_2C has shown promise in producing small carbide particles suitable for catalysis. Molybdate salts have been shown to readily

dissolve in aqueous solutions and have also been shown to adsorb well onto various substrates including activated carbon [44]–[46]. Solutions of ammonium heptamolybdate and sucrose were used to synthesize Mo_2C using multiple TPR procedures by Vitale, et al. Mo_2C was synthesized at temperatures as low as 250-400 °C over a carburization time of 24-72 h at higher temperatures (800 °C) allowing for synthesis to be completed in as little as 30 minutes [34]. A sonochemical approach for synthesizing Mo_2C-SiO_2 nanoparticles was also developed by Arul Dhas, et al. A slurry mixture consisting of 1 g molybdenum hexacarbonyl ($Mo(CO)_6$) and 0.3 g of silica microspheres in 100 mL of decane was subjected to ultrasonic irradiation under an Ar atmosphere to produce Mo_2C. Carbide powders were collected from solution via centrifugation [39].

1.2.   Covalent Carbides

1.2.1. Silicon Carbide

Unlike the interstitial carbides, covalent carbides exhibit predominately covalent bonding between the carbon, and non-carbon, components of the carbide ceramic. Silicon carbide forms a lattice of Si-C tetrahedral structures that can be arranged into more than 200 different polytypes. Examples of some of the more common SiC polytypes are presented in Figure 1.
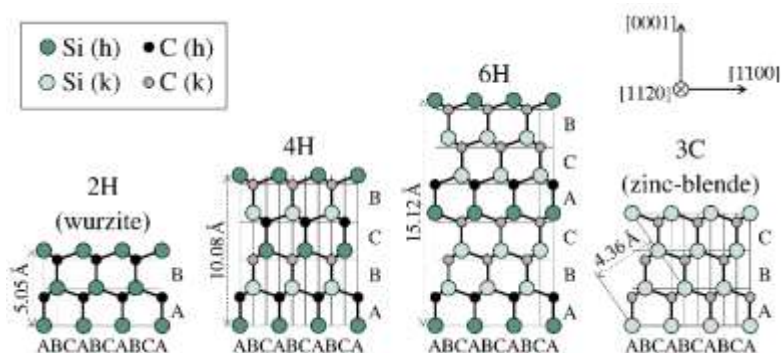
Figure 1: Polytypes of SiC [47]

Lighter than the hardmetals, SiC is often used in ceramic body armor, brake discs, and high-pressure valves and nozzles [48]. Some of the material properties of SiC are presented in Table III.

Table III: Properties of SiC [49], [50]

Property	Value Range	Units
Density	3.1	g/cm^3
Melting Point	1477-1682	°C
Compressive Strength	3.90	GPa
Hardness	27.5	GPa
Young's Modulus	410	GPa
Poisson's Ratio	0.14	-

Due to its thermal and electrical conductivity, along with its ability to resist oxidation at elevated temperatures, SiC is also being considered as a replacement for pure silicon as a semiconductor material [51]. Silicon carbide has been used as a component of a number of electronic devices including UV photodiodes and blue light LEDs [52].

Commercial production of SiC is carried out by the Acheson Process, that has been used to produce SiC since its initial synthesis by Acheson in 1891 [53]. Although some minor improvements and scale-up have occurred over the years, the Acheson Process has undergone relatively little change since its original development. This process involves using a direct resistance furnace with a graphite electrode to heat a mixture of carbon, salt, and silica sand to temperatures exceeding 1800 °C to convert the silica sand to SiC [48].

Alternative SiC synthesis routes have been developed in order to reduce carburization temperatures and produce SiC products with specific morphologies and smaller particle sizes that are not attainable through the Acheson Process. Research has shown that the SiC carburization temperature can be lowered by the use of carbothermal reduction in the presence of inert or reducing gas atmospheres (H_2). Xiang, et al. synthesized SiC from pellets of graphite and quartz

using varying mixtures of Ar and H_2 at temperatures as low as 1200 °C. Complete carburization of the quartz powder was found to occur more rapidly under H_2 than under Ar with higher temperatures also inducing more rapid carburization rates [54]. A carbothermal reduction process was also used by Martin, et al. to produce SiC nanocrystals from a precursor material consisting of sugar suspended within a silica nanoparticle sol-gel. This precursor was then freeze-dried and carburized within a temperature range of 1550-1800 °C under Ar and a vacuum of 0.02 kPa. This process produced SiC particles with an average crystallite size of approximately 20 nm [55]. Carbothermal reduction processes have also been used to synthesize SiC from other precursor materials such as wood and rice hulls [56]–[58]. Silicon carbide has also been produced by a number of other synthesis routes including chemical vapor deposition, synthesis in sodium vapor, pyrolysis of Si-containing polymers, and laser/plasma activated gas-phase chemical reactions [57], [59].

The use of sodium silicate solutions has shown promise in the development of precursors for SiC synthesis. Silicate solutions have been used by Gogotsi, et al. to produce wood chips impregnated with silicate that were then used to produce SiC via carbothermal reduction in Ar at 1400 °C. The SiC produced by this method formed nanofibers, or SiC whiskers, which were capable of being used for structural applications or as a filtration media [56], [58]. Sodium silicate solutions were also used by Mengning, et al. to produce SiC nanostructures supported on single-walled carbon nanotubes via carburization under an Ar/H_2 atmosphere at 1300-1500 °C [60].

2. Theory

2.1. Carburization Thermodynamics and Kinetics

A review of the important thermodynamic and kinetic considerations regarding carburization is presented in this section. In addition to the presentation of literature sources, predominance area diagrams and thermodynamic models for the three carburization systems investigated in this research were prepared using HSC Chemistry 9 software (version 9.0). The thermodynamic models were prepared by means of the free energy minimization algorithm used in HSC Chemistry 9. More detailed information on the input data used to construct the models is available in the appendix.

2.1.1. Tungsten Carburization

Conventional carburization of tungsten has been determined to occur through the following chemical reaction:

$$W_{(s)} + C_{(s)} \rightarrow WC_{(s)} \tag{1}$$

However, this reaction does not account for some of the intermediate reactions that actually take place during the carburization process. Because the commercial carburization of tungsten with solid carbon is generally carried out under a constant flow of H_2, it is believed that the carburization reaction is aided by the conversion of the solid carbon to methane in the presence of H_2 [61]. The conversion of carbon to methane changes the carburization process from a solid-solid reaction to a gas-solid reaction. Alternatively, the carburization of tungsten can be written as a two-step reaction as shown by Equations (2) and (3).

$$C_{(s)} + 2H_{2(g)} \rightarrow CH_{4(g)} \tag{2}$$

$$W_{(s)} + CH_{4(g)} \rightarrow WC_{(s)} + 2H_{2(g)} \tag{3}$$
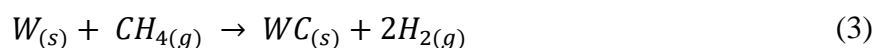
Through this two-step sequence, the H_2 essentially catalyzes the carburization reaction by improving the reaction kinetics [61]. Iwai, et al. determined that the Gibbs free energy of formation of WC from the reaction presented in Equation (3) can be calculated by the following expression:

$$\Delta G = -52330 + 14.06T \ J/mol \, , (900\,°C \ \leq T \leq 1300\,°C) \ [62]. \tag{4}$$

In addition to the reaction that produces WC, competing W-C reactions can produce W_2C instead of WC according to the following reactions [61]:

$$2W_{(s)} + C_{(s)} \ \rightarrow \ W_2C_{(s)} \tag{5}$$

$$2W_{(s)} + CH_{4(g)} \ \rightarrow \ W_2C_{(s)} + H_{2(g)}. \tag{6}$$
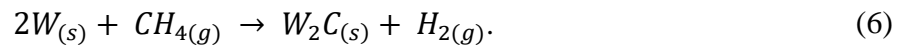
The carbide species formed are directly related to the relative amounts of carbon and metal that are present during carburization. This behavior can be observed in the binary phase diagram for the W-C system shown in Figure 2.
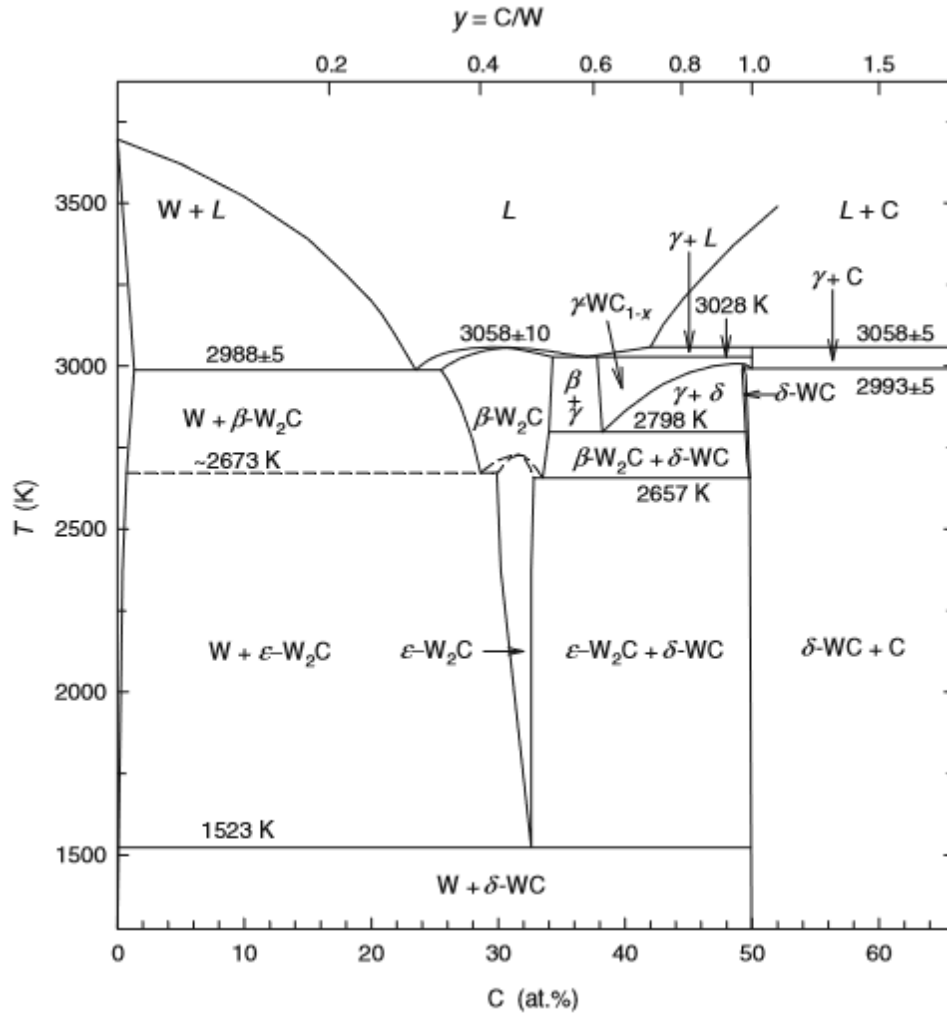
Figure 2: Phase Diagram of the Tungsten-Carbon System [63]

In the W-C phase diagram, stable non-stoichiometric and non-monolithic species are present at varying concentrations of carbon. The most prevalent of these species is the bi-metallic W_2C also known as tungsten semi-carbide or lower tungsten carbide [63]. Although W_2C is not thermodynamically stable at equilibrium until 1500 °C, it is often detected in carburization products at temperatures below 1500 °C, an indication that W_2C acts as an intermediate phase during the production of WC. A nonstoichiometric species, WC_{1-x}, also forms at elevated temperatures (>2700 °C). The formation of these metastable phases can be restricted by lowering carburization temperature and using higher concentrations of carbon in order to

force the production of the more commercially desirable monolithic tungsten carbide species. Both WC and W_2C have hexagonal crystal structures.

The stability of the monocarbide phase, WC is further demonstrated by the phase stability diagram of the W-C-O system at 950 °C presented in Figure 3. The stability of each species is presented on a logarithmic scale as a function of CO and O_2 partial pressures. This diagram was prepared using the thermodynamic calculation software, HSC Chemistry 9.
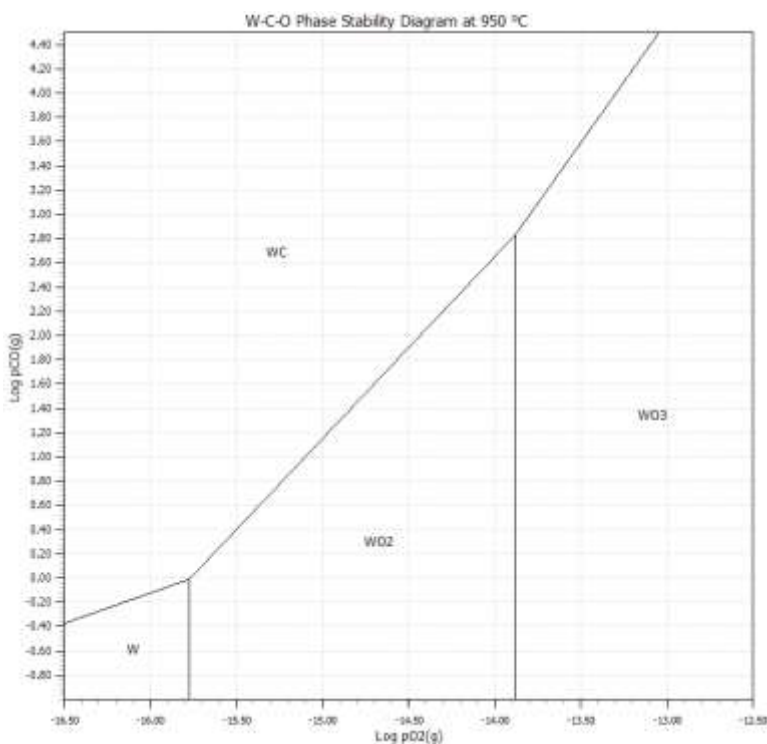
Figure 3: Phase Stability Diagram of the W-C-O System at 950 ºC

From a thermodynamic standpoint, WC should be the only carbide phase present at 950 °C over a wide range of gas compositions, especially in the absence, or near-absence, of oxygen.

A thermodynamic model of W-carburization from a tungstate-loaded activated carbon precursor is presented in Figure 4. Carburization is modeled based on a system containing the dissolved tungstate anion (WO_4^{2-}), an excess of carbon to represent the activated carbon substrate, and a gas mixture consisting of CH_4, H_2, and CO. The diagram presents a number of

chemical species, both products and reactants, as their equilibrium concentrations in kmols as a function of temperature in °C.
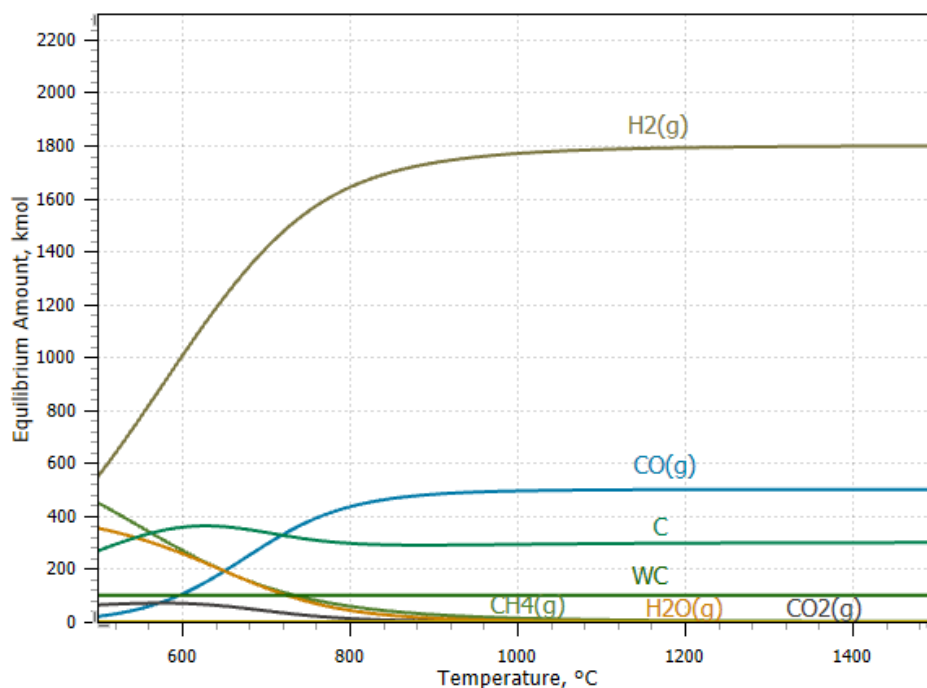
Figure 4: Thermodynamic Model of W-Carburization (HSC Chemistry)

The thermodynamic model further illustrates the stability of WC. The model predicts the complete conversion of the present tungsten species to WC at temperatures well below 1000 °C as well as the presence of a substantial excess of carbon. The relatively constant amount of solid carbon and the rapid decrease in CH_4 concentration indicates that carburization in this system will likely occur primarily through the interactions between the tungsten species and the gaseous carbon sources.

The reaction rate of the tungsten carburization reaction in the presence of reducing gases (H_2 and CH_4) depends on a number of factors including the partial pressures of the reducing gases, the size (effective diameter) of the tungsten particles, and the nature of the tungsten source material. Research has indicated that the initial reaction between tungsten particles and carbon-containing gases is controlled at the surface of the tungsten particles by the CH_4-W reaction. As

the surface of the tungsten particles are carburized, the reaction mechanism changes to one controlled by CH_4 diffusion through the carburized surface layer [1]. Thermodynamically, WC is more stable than W_2C and it is generally accepted that W_2C often acts as a metastable intermediate carbide phase during the carburization process. Provided an adequate carbon source, and a lack of kinetic impediments, carburization of W particles is expected to result in the formation of WC [14], [19], [61].

The kinetics of the carburization of tungsten particles in the presence of CH_4 were investigated by Wadsworth et al. Their findings indicated that carburization rate is a first order reaction that depends on the partial pressure of CH_4. It was determined that carburization was initialized by CH_4 adsorption onto the tungsten particle surfaces and the subsequent formation of W_2C and H_2. The mechanism by which the process occurs is represented by the following series of equations:

$$2W^*_{(S)} + CH_{4(g)} \rightarrow W_2CH^*_2 + H_{2(g)} \tag{7}$$

$$W_2CH^*_2 \rightarrow W_2C^* + H_{2(g)} \tag{8}$$

$$W_2C^* \rightarrow W_2C \tag{9}$$
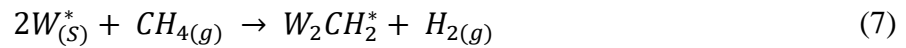
where W^* represents the active sites present within the tungsten lattice and W_2C^* represents the adsorbed carbon atom that remains after the CH_4 reacts with the available tungsten [14]. These equations in combination with the random walk theory were used to produce an expression to relate the adsorption rate to the equilibrium constants of Equations (7), (8), and (9) as well as the partial pressures of CH_4 and H_2. The adsorption reaction equation is presented in Equation (10):

$$\frac{dn}{dt} = P_{CH_4} k_7 \left[1 - \left(\frac{P^2_{H_2}}{P_{CH_4}} \right) \left(\frac{1}{K} \right) \right] \text{[14]} \tag{10}$$

where the rate of adsorption with respect to time is represented by *dn/dt*, k_6 represents the

equilibrium constant for Equation (7), and *K* represents the combined equilibrium constants for

the forward and reverse reactions presented in Equations (7), (8), and (9) (*K = k₇k₈k₉/k₇'k₈'k₉'*).

Experimentation, combined with this adsorption equation, allowed the authors to determine an

enthalpy of activation value of 12.4 kcal/mol. Following initial carburization, the mechanism

changes from one controlled by CH_4 adsorption to one that is controlled by bulk diffusion of

carbon through a layer of carburized tungsten to produce WC [14].

Reaction mechanisms have also been proposed for producing WC from tungsten oxide

precursors. Generally, the proposed mechanisms require reduction of various tungsten oxide

species to metallic tungsten before carburization to WC with W_2C formed as an intermediate

phase [64], [65]. Koc et al. proposed an alternative reaction was possible by carbon coating

tungsten oxide powders and inducing carburization in a H_2/Ar atmosphere at temperatures

between 1000 and 1400 °C. It was determined that W_2C formation could be bypassed as

carburization occurred by producing WC around an inner core of metallic tungsten. This reaction

relies on the formation of activated carbon from the carbon coating the surface of the tungsten

oxide particles according the following reaction sequence:

$$WO_3 + W_xO_y \rightarrow W_{18}O_{49} + WO_2 + W \rightarrow WO_2 + W \rightarrow WC \text{ [15]}. \tag{11}$$
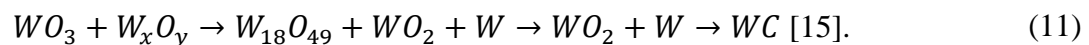
Regardless of the type of tungsten oxide used, it has been accepted that reduction to metallic

tungsten must occur before carburization to WC can take place [7], [19], [20], [23]–[25], [66].

2.1.2. Molybdenum Carburization

As another group of interstitial carbides, the molybdenum carbide system shares a

number of similarities with the tungsten carbide system. Commercial synthesis of Mo_2C from

blends of solid Mo and C is defined by the chemical reaction:

$$2Mo + C \rightarrow Mo_2C \tag{12}$$

Again, like the reaction for commercial WC production, the carburization of Mo metal particles can be expressed as a reaction with methane due to a reaction between solid carbon and the reducing H_2 atmosphere commonly used in this production of metal carbides. The reaction between Mo and CH_4 to produce Mo_2C can be written as:

$$2Mo + CH_4 \rightarrow Mo_2C + 2H_2. \tag{13}$$

An expression for the Gibbs free energy of the carburization reaction via methane decomposition was determined experimentally by Iwai, et al. From their work, the Gibbs free energy of formation for Mo_2C can be expressed as:

$$\Delta G = -68270 + 8.23T \; J/mol, (900\,°C \leq T \leq 1300\,°C) \; [62]. \tag{14}$$

Because Mo produces interstitial carbides, it is possible to form multiple carbide species depending on the amount of Mo and C present in a given system as well as the temperature of the Mo/C mixture. This behavior can be observed in the binary phase diagram of the Mo-C system presented in Figure 5.
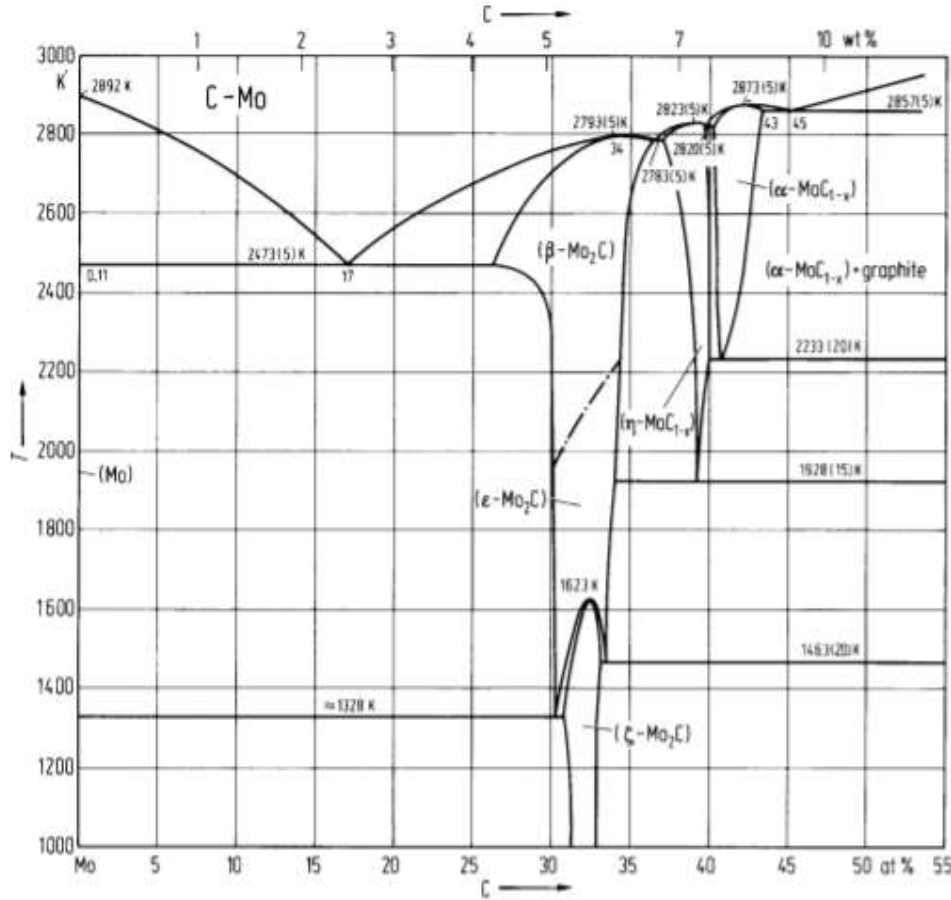
Figure 5: Phase Diagram of the Molybdenum-Carbon System [2]

The carbide species, Mo_2C, is shown to form with the addition of 30-35 atomic % C and, as temperature and carbon content increase, the presence of stable non-stoichiometric carbide species can be produced in the form of the MoC_{1-x} compound. These stable, nonstoichiometric carbide species are the result of the inherently unstable nature of the monocarbide MoC. MoC often reverts to either Mo_2C or the nonstoichiometric MoC_{1-x} species. MoC can form, but often requires higher carburization temperatures and increased pressure [67] or through the addition of stabilizing agents [67]–[69]. Mixed crystals of MoC and Mo_2C have been synthesized at lower temperatures (<1000 °C) for catalysis operations using a Mo-containing, organic-inorganic hybrid composite compounds [30]. The crystal structure of these interstitial carbides is altered as

the operating temperature increases while the stoichiometric composition of the carbides remains the same.

The phase stability diagram of the Mo-C-O system at 850 °C is presented in Figure 6. The stability region of each species is presented on a logarithmic scale as a function of CO and O_2 partial pressures.
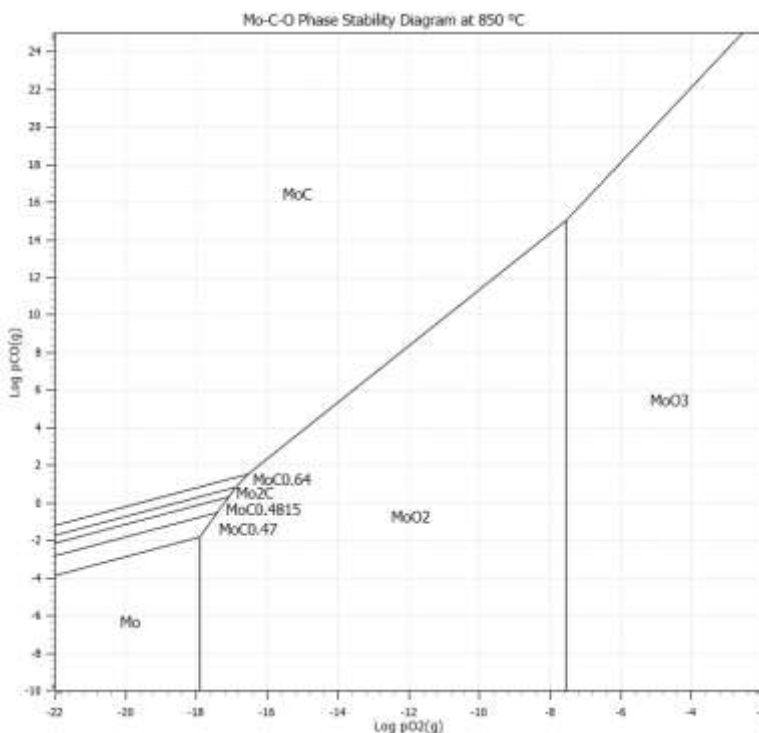
Figure 6: Phase Stability Diagram for the Mo-C-O System at 850 ºC

The phase stability diagram shows that region in which Mo_2C is thermodynamically stable is relatively narrow and requires very low O_2 partial pressures. Although the MoC stability region is large, only a small portion exists below atmospheric conditions showing the need for high pressures to allow for its synthesis.

A thermodynamic model of Mo-carburization from a molybdate-loaded activated carbon precursor is presented in Figure 7. Carburization is modeled based on a system containing the dissolved molybdate anion (MoO_4^{2-}), and a gas mixture consisting of CH_4, H_2, and CO. The

diagram presents a number of chemical species, both products and reactants, as their equilibrium concentrations in kmols as a function of temperature in °C.
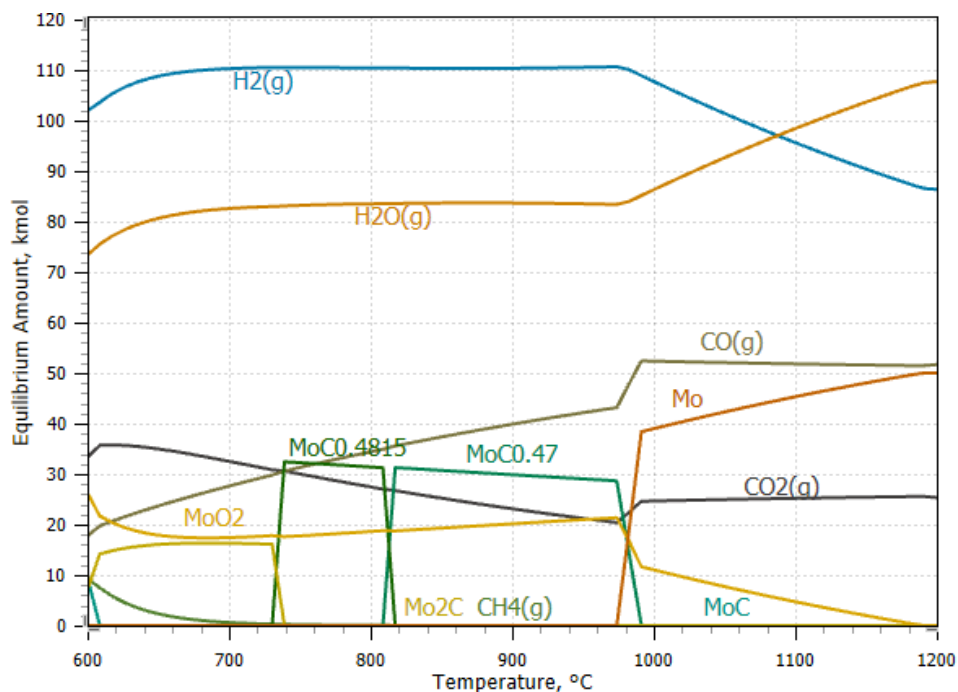
Figure 7: Thermodynamic Model of Mo-Carburization (HSC Chemistry)

The thermodynamic model shows the increased complexity of the Mo-carburization reaction compared to W-carburization. The model predicts the stability of Mo_2C at lower temperatures (600-740 °C) with nonstoichiometric carbide species becoming the dominant carbide species present at higher temperatures. While some MoC is briefly present at 600 °C, the concentration of this species rapidly decreases with increasing temperature and remains essentially nonexistent over the rest of the temperature range.

The synthesis of Mo_2C is governed by the diffusion of carbon into the Mo metallic lattice through a layer of carbide reaction product. The kinetics for the carburization of a Mo plate to form Mo_2C at 1000-1400 °C in the presence of CH_4 and graphite were investigated by Rosa. Carburization experiments showed that Mo_2C growth exhibited a parabolic relationship where the thickness of the carbide layer grew as a function of time such that,

$$X_c = (K_p t)^{1/2} + A \text{ [70]}, \tag{15}$$

where X_c represents the thickness of the carbide layer in cm, K_p represents the parabolic rate

constant in cm^2/h, t represents carburization time in h, and A represents a temperature-specific

constant. The rate constant for the growth of Mo$_2$C within the observed temperature range can be

expressed by the following equation:

$$K_p (cm^2/s) = 32.63 \pm 1.52 e^{[(-319.06 \pm 5.12)/RT]} \text{ [70]}, \tag{16}$$

where T represents the carburization temperature within the range of 1000-1400 °C, and R

represents the Ideal Gas Constant in units of J/mol K.

The diffusion mechanism of carbon through the Mo$_2$C product layer into the Mo lattice is

graphically represented in Figure 8.
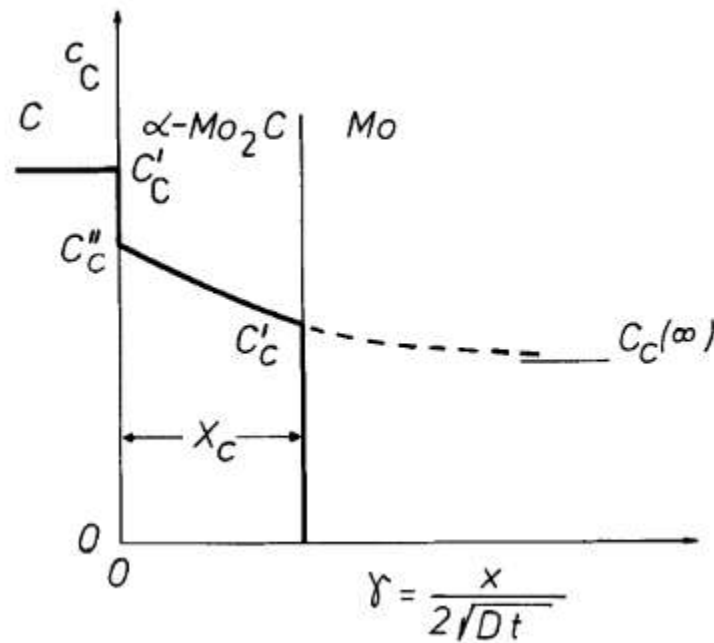
Figure 8: Carbon Diffusion in the Formation of Mo$_2$C [70]

In the graphical representation, *C*, represents the carbon phase, the region labelled, *Mo$_2$C*,

represents the carbide layer being formed with a thickness of X_c, and Mo represents the Mo

metallic lattice. The concentration of carbon at the carburization medium/carbide interface is

represented by C'$_C$, while C_C^∞ represents the carbon concentration achieved as the distance of diffusion, x, approaches infinity. C_c' and C_c'' represent carbon concentration within the carbide layer. By applying Fick's second law of diffusion to experimental carburization data, Rosa defined the diffusion coefficients of C in Mo$_2$C at 1000 °C, 1100 °C, 1200 °C, 1300°C, and 1400 °C according to the expression:

$$D_c = 68.86 \pm 1.51e^{[(-294.77\pm4.98)/RT]} \tag{17}$$

where T represents the carburization temperatures within the range of 1000-1400 °C, and R is the ideal gas constant (8.31 J/mol K). An activation energy for carbon uptake was determined to be 294.77 kJ/mol [70].

The kinetics of the carburization of molybdenum oxides to form Mo$_2$C have also been investigated. Chaudhury, et al. investigated the carburization of MoO$_3$ in the presence of solid carbon at temperatures below 900 °C. Thermogravimetric and gas composition analyses showed that MoO$_3$ was first reduced to MoO$_2$ forming CO and CO$_2$ from the oxidation of the solid carbon. Following the formation of MoO$_2$, this oxide was then converted to Mo$_2$C according to the following chemical reaction:

$$2Mo_{2(s)} + 4.175C_{(s)} \rightarrow Mo_2C_{(s)} + 2.35CO_{(g)} + 0.825CO_{2(g)} \text{ [71]}. \tag{18}$$

The experimental results obtained by Chaudhury et al. showed that the carburization of MoO$_3$ with solid carbon proceeded through the formation of an intermediate metallic Mo phase. The authors proposed that this Mo intermediate phase was the result of poor diffusion of carbon from the C-Mo$_2$C interface to the interior of the Mo-containing particles where there existed a Mo$_2$C-MoO$_3$ interface. Poor diffusion through the C-Mo$_2$C interface resulted in the formation of a layer of metallic Mo between the Mo$_2$C layer and the un-carburized core of the MoO$_3$ particles. Eventually, this Mo layer is carburized to form Mo$_2$C via the diffusion of C through the Mo$_2$C

layer and the rate controlling mechanism is the diffusion of carbon-containing gases (CO/CO_2) through the product layer [71].

The carburization mechanism for Mo-oxides appears to depend on the nature of the carbon source used during the carburization process. Hanif, et al. used hydrocarbon gases with H_2 to carburize MoO_3 powders at 400-700 °C via the TPR method. While Hanif, et al. also observed the initial reduction of MoO_3 to MoO_2, the authors observed that an oxycarbide intermediate, MoO_xC_y, was detected at 600 °C under CH_4/H_2 and C_2H_6/H_2 atmospheres. This oxycarbide was subsequently converted to Mo_2C at 700 °C [33]. The proposed reaction pathway is presented in Figure 9.
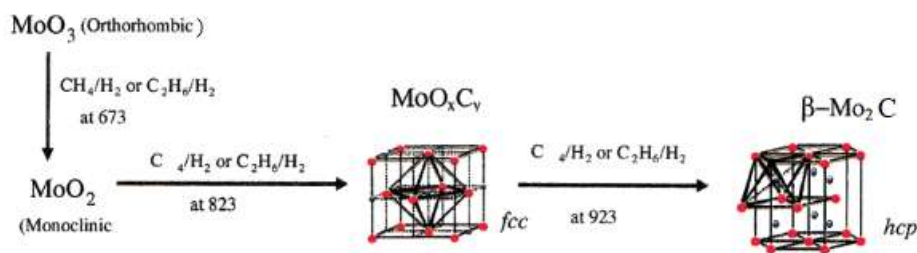
Figure 9: Gas Carburization Reaction Pathway of MoO₃ [33]

2.1.3. Silicon Carburization

Because of the covalent nature of the Si-C bond, the Si-C system does not contain the metastable, non-stoichiometric species that exist within the interstitial carbide systems. This behavior can be observed in the Si-C binary phase diagram presented in Figure 10.
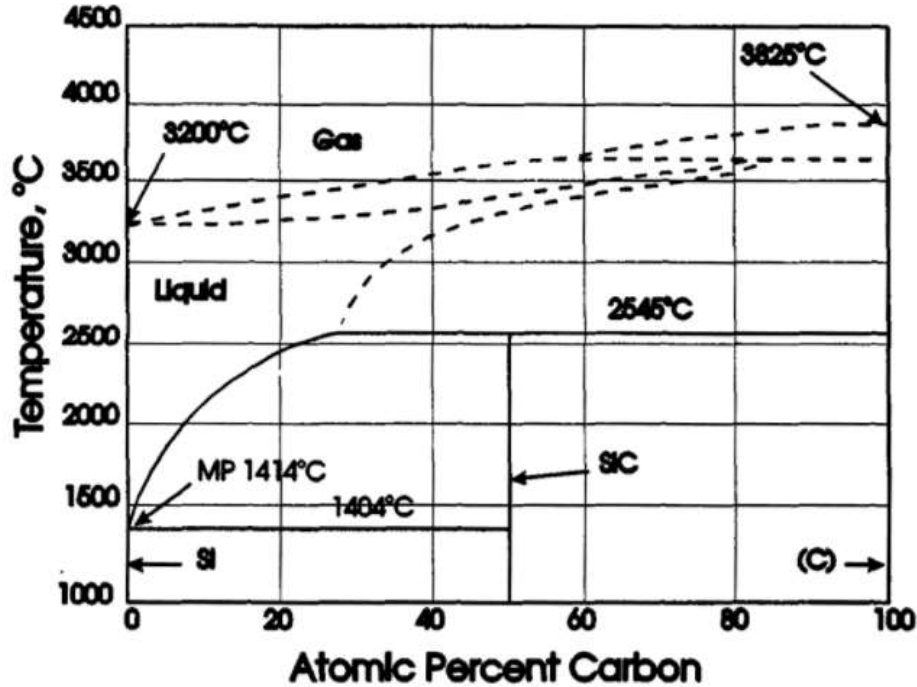
Figure 10: Phase Diagram of the Si-C System [2]

Although not shown on this phase diagram, two SiC species, α-SiC and β-SiC, exist with

different crystal structures. The most common species, β-SiC, possesses a zinc-blende face-

centered cubic crystalline structure and is formed when carburization occurs at temperatures

below 2100°C. The higher-temperature α-SiC has numerous polytypes that mostly exhibit

variations on rhombohedral and hexagonal crystal structures [2].

The carbothermal reduction reaction associated with the Acheson process can be

expressed as:

$$SiO_{2(s)} + 3C_{(s)} \rightarrow SiC_{(s)} + 2CO_{(g)}. \tag{19}$$
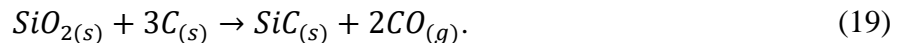
The Gibbs free energy equation for this reaction has been determined to be:

$$\Delta G° = 598.18 - 0.3278T \ (kJ/mol), \tag{20}$$

where the value for the standard Gibbs free energy reaches zero at 1525 °C [54].

The carbothermal reduction reaction to form SiC has been shown to occur at temperatures below 1525 °C, however. A phase stability diagram for the Si-C-O system at 1250 °C is presented in Figure 11. The stability region of each species is presented as a function of CO and O_2 partial pressures.
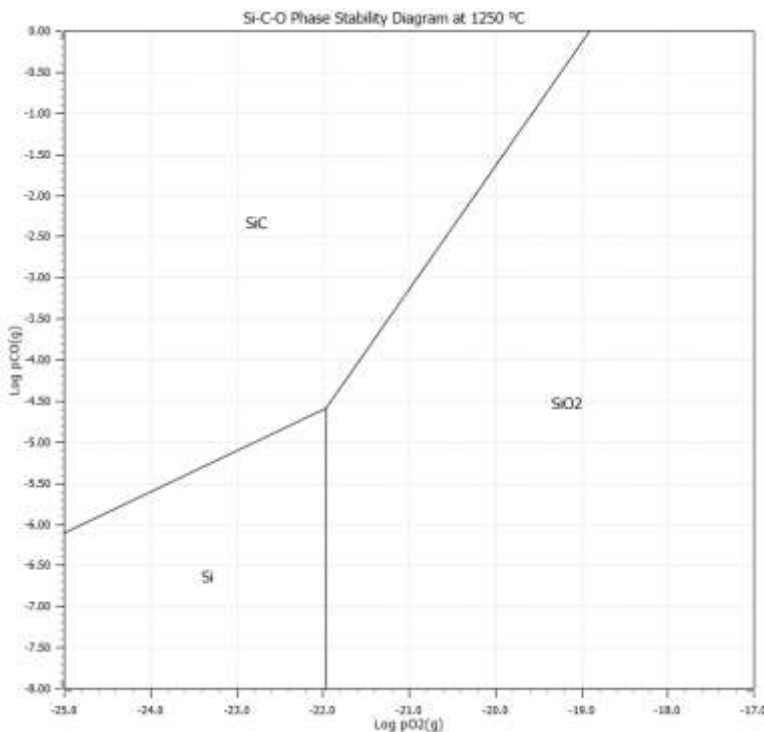
Figure 11: Phase Stability Diagram for the Si-C-O System at 1250 ºC

From the phase stability diagram, it is possible to observe that SiC is stable at 1250 °C provided that the CO and O_2 partial pressures are maintained well below atmospheric pressure. The P_{O2} must be extremely low, less than 10^{-18} atm is required for the synthesis of SiC.

A thermodynamic model of Si-carburization from a silicate-loaded activated carbon precursor is presented in Figure 12. Carburization is modeled based on a system containing the dissolved SiO_4^{4-} anion, an excess of carbon to represent the activated carbon substrate, and a gas mixture consisting of H_2. The diagram presents a number of chemical species, both products and reactants, as their equilibrium concentrations in kmols as a function of temperature in °C.
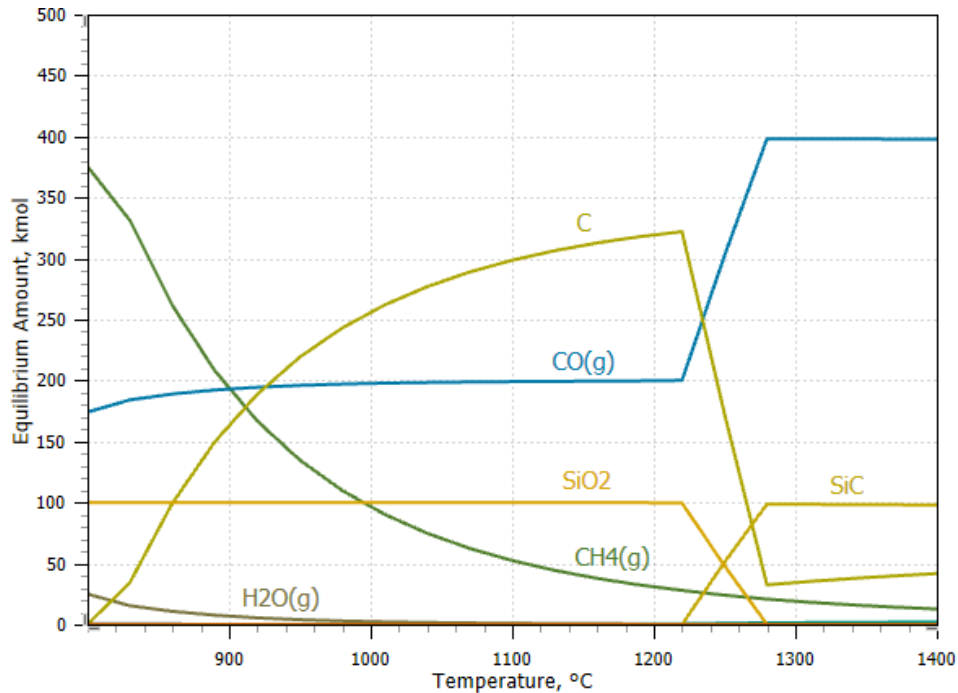
Figure 12: Thermodynamic Model of Si-Carburization (HSC Chemistry)

The thermodynamic model shows that SiO_2 is the dominant stable solid species present at temperatures below 1220 °C. At this temperature, SiC is shown to form and continues to be the dominant species formed at higher temperatures.

Although the materials used in the commercial synthesis of SiC are solids, the actual carburization reaction occurs between the solid carbon source and a Si-containing gaseous intermediate compound, $SiO_{(g)}$ [2]. The reactions involved in the synthesis of SiC from SiO_2 and solid carbon can be expressed as:

$$SiO_{2(s)} + C_{(s)} \rightarrow SiO_{(g)} + CO_{(g)} \tag{21}$$

$$SiO_{2(s)} + CO_{(g)} \rightarrow SiO_{(g)} + CO_{2(g)} \tag{22}$$

$$C_{(s)} + CO_{2(s)} \rightarrow 2CO_{(g)} \tag{23}$$

$$SiO_{(g)} + 2C_{(s)} \rightarrow SiC_{(s)} + CO_{(g)}. \tag{24}$$
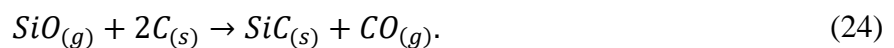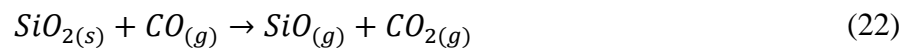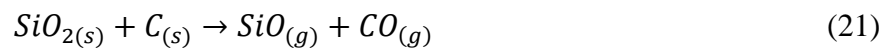
The standard Gibbs free energy for the reaction between solid carbon and the $SiO_{(g)}$ intermediate can be expressed as a function of temperature according to the following equation:

$$\Delta G° = -78.89 + 0.0010T \ (kJ/mol) \ [54]. \tag{25}$$

The existence of the $SiO_{(g)}$ intermediate allows for the production of SiC at temperatures below 1525 °C.

A reducing gas atmosphere, such as H_2, has been shown to alter the carbothermal reduction reaction pathway. Li et al. studied the effects of H_2/Ar gas mixtures on the carbothermal reduction of quartz powder mixed with graphite at temperatures ranging from 1000 °C to 1600 °C. The authors observed that, in the presence of H_2, the solid carbon reacted with H_2 to form CH_4. This CH_4 then reacted with the quartz powder to form $SiO_{(g)}$ according to the reaction:

$$SiO_{2(s)} + CH_{4(g)} \rightarrow SiO_{(g)} + CO_{(g)} + 2H_{2(g)} \ [54]. \tag{26}$$
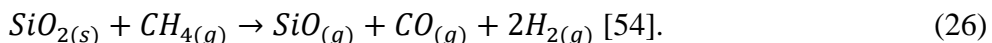
Li, et al. also observed that $SiO_{(g)}$ was also formed by the reduction of SiO_2 with H_2:

$$SiO_{2(s)} + H_{2(g)} \rightarrow SiO_{(g)} + H_2O_{(g)} \ [54]. \tag{27}$$
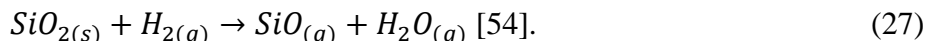
The $H_2O_{(g)}$ formed during this reaction is subsequently converted to H_2 and CO through reactions with the solid carbon. The reaction of $SiO_{(g)}$ with solid carbon to form SiC occurs regardless of the nature by which the $SiO_{(g)}$ intermediate is formed.

The mechanism by which the carburization reaction occurs is still in question. Researchers have proposed a number of explanations for how the reaction takes place and which step is rate controlling [72], [73]. A number of factors can affect the kinetics of the carburization reaction including temperature, carbon particle size, the nature of the Si-containing precursor material, and the removal of product gases such as CO [72]. It is generally agreed that carburization occurs at the surface of the carbon particles due to the migration of the SiO gas

intermediate and that the reaction is diffusion-based in regard to carbon moving through the SiC

product layer. Various researchers have determined activation energies for this reaction step with

values in the range of 100 to 400 kJ/mol [73], [74].

A useful kinetic model for SiC formation has been proposed by Weimer, et al using

experimental data from the rapid carburization of a spray-dried silica powder/carbon black

colloidal mixture. The authors proposed the reaction mechanism that is illustrated in Figure 13.
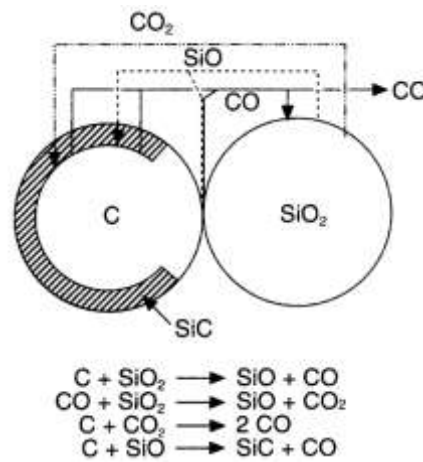
Figure 13: Carburization Mechanism for SiC Synthesis Proposed by Weimer, et al. [72]

The proposed carburization mechanism is based on the close contact between silica and carbon

particles that allowed for the evolution of $SiO_{(g)}$, which migrated to the surface of the carbon

particles, to produce a layer of SiC. Carbon monoxide is generated by the production of $SiO_{(g)}$

and SiC, and also was observed to act as a reactant in the formation of $SiO_{(g)}$ to produce CO_2.

The authors used a contracting volume shrinking core model to describe the rate of

reaction of converting $SiO_{(g)}$ to SiC using the following equation:

$$k = \frac{1-(1-X)^{1/3}}{t} = \frac{k_o}{d}e^{(-E/RT)} \text{ [72]},$$
(28)

where k represents the reaction rate for carburization in s^{-1}, X represents the fraction of SiO_2

converted to SiC, t represents reaction time in seconds, k_o represents an experimentally-

determined rate parameter of 27.35 m/s, d represents the diameter of the carbon particle in m, E

represents the activation energy in kJ/mol (382 kJ/mol), *R* represents the ideal gas constant (8.314 J/mol K), and *T* represents carburization temperature in K.

2.2. Adsorption Kinetics

Adsorption is the process by which a solid, liquid, or gas molecules adhere to the surface of a material. Generally, adsorption occurs by either chemical adsorption (chemisorption), or physical adsorption (physisorption) depending on the nature of the adsorbent and the adsorbate. Physisorption takes place due to van der Waals forces while chemisorption involves the adsorbate forming a chemical bond with the surface of the adsorbent. With chemisorption, the adsorbate often forms a monolayer on the surface of the adsorbent due to the need for binding sites at the surface. While monolayers can also form from physisorption, it is also possible for multilayers of adsorbate to form in a stacking motion as specific binding sites are not a requirement.

Effective adsorbents are generally materials that have a high surface area to mass ratio. One such example is activated carbon. Activated carbon is derived from the pyrolysis of carbonaceous materials in the absence of oxygen followed chemical treatment to alter its surface chemistry. The evaporation of volatile organics from the carbonaceous material and its further treatment with "activating agents" such as steam or strong acids and bases creates a highly porous surface with surface areas ranging from 1000-3000 m^2/g allowing for the creation of numerous adsorption sites [75]. Research has shown that the development of carburization precursors by the adsorption of ions from solutions onto the surface of activated carbon can lower carburization temperatures and facilitate the development of nanocrystalline carbides and other useful carbide morphologies [26], [34], [55], [60], [76].

2.2.1. Langmuir Adsorption Isotherm

The Langmuir adsorption isotherm is commonly used to model monolayer adsorption behavior. While originally developed to model gas-solid adsorption behavior, it has also been used to model other adsorption systems including the removal of ions from solution. A theoretical concept, the Langmuir adsorption model is based on the assumptions that all of the binding sites on the surface of the adsorbent are uniform, and that both adsorbent and adsorbate behave in an ideal manner [77]. The Langmuir adsorption model can be expressed as a linear equation such that:

$$\frac{C_e}{q_e} = \frac{1}{q_0 b} + \frac{C_e}{q_0}, \tag{29}$$

where C_e represents the equilibrium concentration of adsorbate in mg/L, q_e represents the amount of adsorbate adsorbed onto the surface of the adsorbent per unit mass of adsorbent at equilibrium (mg/g), q_0 is the maximum amount of adsorption (mg/g), and b is the Langmuir constant (L/mg) [78]. By plotting experimental adsorption data, a linear regression can be performed to determine the goodness of fit of adsorption data to this theoretical model to gain insight into the mechanism by which adsorption occurs.

2.2.2. Freundlich Adsorption Isotherm

The Freundlich adsorption model is often used to model multi-layer adsorption behavior or adsorption on a heterogeneous surface. The Freundlich adsorption model can be expressed by the following linear equation:

$$\log q_e = \log K_F + \frac{1}{n}\log C_e, \tag{30}$$

where K_F represents adsorption capacity in L/mg and the *1/n* term represents adsorption intensity. Although it is often considered an empirical model, there have been a number of derivations proposed for the Freundlich equation [79]. Experimental adsorption data is often

fitted to the presented linear equation in order to determine the mechanism by which adsorption occurs.

2.2.3. Tungstate and Molybdate Anion Adsorption

Research has shown that it is possible to adsorb significant quantities of tungstate and molybdate from aqueous solutions onto activated carbon. Ohashi, et al. determined that pH had a strong effect on tungstate adsorption and that it increased as the solution pH approached 2.0. While the authors also found that tungstate and molybdate behavior was very similar in regard to the effect of pH, they were unable to determine the mechanism by which adsorption occurred. They suggested that polymerization of the tungstate and molybdate anions was occurring prior to adsorption [44].

The formation of tungstate and molybdate polyanions at low pH values was confirmed by Cruywagen, et al. The authors determined that, under acidic conditions, tungstate anions react with free H^+ ions during adsorption onto activated carbon to form three different tungsten species, $W(OH)_6$, $HW_2O_7^-$, and HWO_4^-. The relative abundance of each species was found to be pH-dependent and at pH values below 3.0, the primary adsorbed species was identified as $HW_2O_{7(ads)}^-$ [45]. Cruywagen, et al. also investigated the adsorption behavior of molybdate anions from solution and found that the adsorption of molybdate, while occurring under similar conditions to tungstate, was more complex. Although multiple molybdate polyanions were identified with the pH range of 1.0-5.0, adsorption was determined to occur primarily through the formation of $[HMo_2O_7]^-$ as well as $[HMoO_4]^-$ and $Mo(OH)_6$ [80]. For both tungstate and molybdate, Cruywagen, et al. determined that the adsorbed species were chemisorbed to the surface of the activated carbon through reactions with oxygen bound to the carbon surface. As tungsten (VI) and molybdenum (VI) are generally octahedrally coordinated, the species observed

to be the primary adsorbates all have vacant binding sites to allow for the completion of the

octahedral orientation [45], [80]. A diagram depicting the adsorbed molybdate species formed on

the activated carbon surface through interactions with oxygen binding sites is presented in Figure

14.
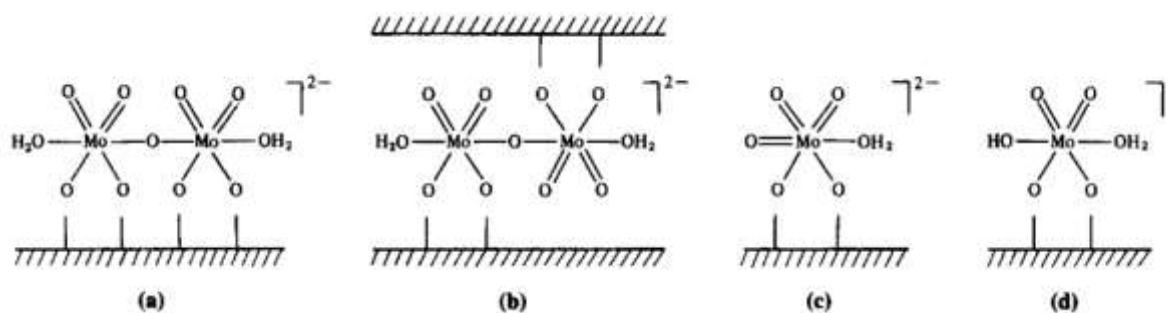
Figure 14: Proposed Structures for Adsorbed Species: (a) dimer, (b) dimer in a micropore, (c) [HMoO₄]⁻, (d)

Mo(OH)₆ [80]

2.2.4. Silicate Anion Adsorption

Little information is available on the adsorption of silicate anions onto activated carbon.

However, activated carbon is frequently impregnated with silicate solution in order to increase its

adsorption capabilities in certain systems [81], [82]. Due to its use as a chemical depressant in

the flotation process, information is available on the adsorption of silicate onto the surfaces of

various minerals [83], [84]. The behavior of sodium silicate in solution and its adsorption onto

synthetic magnetite particles was investigated by Yang, et al. The authors showed that

polymerization of the silicate anions also took place in solution and that the abundance of these

polymerized silicate-based anions increased with increasing silicate concentration.

Polymerization of the silicate anions was also found to increase with decreasing pH. It was

determined that two silicate species, [SiO(OH)3]- and Si(OH)4, were the primary silicate species

involved in adsorption and that chemisorption occurred on the surface of the magnetite particles

through a ligand-exchange mechanism with hydroxyl groups present on the surface of the magnetite. Polymerization following adsorption was also determined to occur allowing for further surface accumulation. Both solution concentration and pH were shown to have a significant effect on the adsorption of silicate species and the type of species present both in solution and at the surface during adsorption [83].

3. Hypothesis and Objectives

The purpose of this research was to experimentally evaluate methods for synthesizing carbide ceramics that reduced carburization energy requirements, produced particles with the submicron to micron size range, and that was versatile enough to synthesize multiple carbides of interest. Tungsten carbide (WC), molybdenum carbide (Mo_2C), and silicon carbide (SiC) were selected for investigation based on the relatively benign nature of their aqueous solutions and the demand for these materials in industry.

This research is predicated on the hypothesis that adsorbing metal ions onto the surface of a source of carbon will produce a precursor material that, upon carburization, will result in the synthesis of fine-grained micron/submicron-scale carbide particles on the activated carbon surface. Carburization temperature will be minimized through the application of optimized reducing gas mixtures of hydrogen (H_2), methane (CH_4), and carbon monoxide (CO). Although numerous studies have been conducted on the use of reducing gases to synthesize carbide ceramics [7], [9], [11], [13], [20], [26], [85], [86], none of the reviewed studies used the approach developed in this study, nor did the reviewed studies incorporate statistical methods of process modelling and parameter optimization. As part of this research, the carbide production process also incorporated the application of statistical analyses of the process variables associated with anion adsorption and precursor carburization using experimental design methods such as 2-factorial and response surface modeling.

4. Experimental

4.1. Apparatus

4.1.1.1. Bulk Adsorption

Bulk adsorption experiments were conducted to produce consistent batches of W-loaded or Mo-loaded precursor. These experiments were carried out using a Fisher Scientific overhead laboratory stirrer mounted onto a ring stand and either a 4 L or a 6 L beaker depending on the amount of solution used. A diagram of the bulk adsorption assembly is presented in Figure 15.
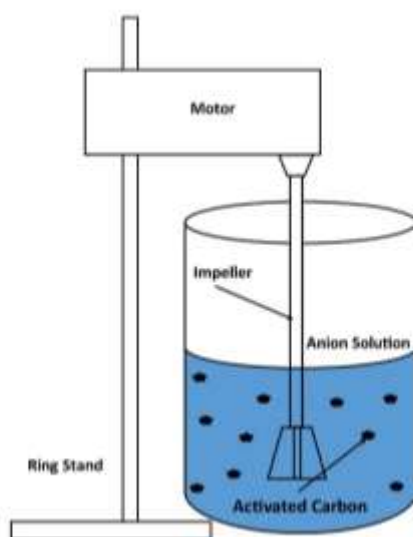
Figure 15: Assembly for Bulk Production of Anion-Loaded Activated Carbon Precursor

4.1.1.2. Carburization Furnaces

Initial carburization experiments involving the W-loaded and Mo-loaded precursors were carried out in an MTI GSL 1100X tube furnace using a 2 in. diameter fused quartz reactor tube. Flange seals were used to enclose the interior of the reactor tube and prevent oxygen from entering the reaction tube during carburization. Initial carburization experiments were carried out using an inert argon (Ar) atmosphere and, in the case of the Mo-loaded precursor, some experiments were carried out using a reducing H_2 atmosphere. For carburization experiments involving the Si-loaded precursor, the same assembly was used except the MTI GSL 1100X

furnace was replaced with an MTI GSL 1500X tube furnace and the fused quartz reactor tube was replaced with a 2 in. diameter alumina (99.8%) reactor tube that was capable of service at temperatures exceeding 1200 °C. The Si-carburization experiments also used either an Ar or a H_2 atmosphere. A schematic of the MTI furnace assembly is presented in Figure 16.
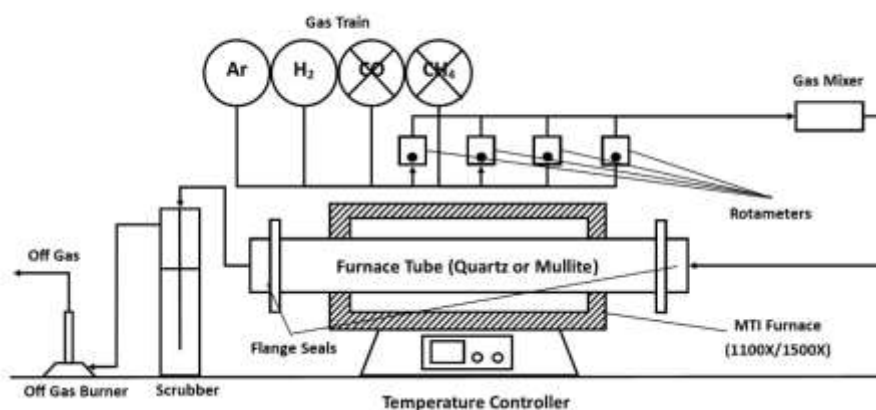
Figure 16: MTI Furnace Assembly for Carburization of Anion Loaded Precursors

The furnace assembly used a gas train containing cylinders of Ar, H_2, CO, and CH_4. The flow rate of each gas was regulated using Omega rotameters calibrated to each gas using a DryCal Defender 530+ primary calibrator. The gas(es) passed through a gas mixer composed of a steel tube filled with alumina cylinders to promote turbulent flow before entering the furnace through a port in the flange seal. As the gas mixture flowed out of the furnace it was passed through a small scrubber filled with deionized water before being flared using a small burner inside a fume hood.

The temperature inside the furnace was regulated using an MTI programmable temperature controller that provided constant temperatures throughout the furnace interior with excellent precision (±1 °C). The MTI GSL 1100X was heated using heating elements composed of Fe-Cr-Al alloy doped with Mo. Temperature was measured using an internal K-type

thermocouple. The MTI GSL 1500X was heated using four 1600 °C-grade SiC rods and temperature was measured using as S-type thermocouple.

W-loaded and Mo-loaded precursor was also carburized using a larger Applied Test Systems (ATS) 3210 split tube furnace heated by Kanthal APM winding. Temperature was controlled using a series of three Eurotherm programmable temperature controllers with an additional Eurotherm temperature controller acting as an "over temp" monitor to ensure overheating of the furnace did not occur. The temperature inside the furnace was measured using K-type thermocouples. Samples were placed inside a fused quartz reactor vessel (Allen Scientific Glass Inc.) with molded baffles to allow for mixing of the sample as it was rotated using a removable variable drive motor assembly with sprocket and drive chain. The ends of the quartz reactor were fitted with quartz ball joint attachments that were sealed using high temperature vacuum grease. The same gas train described in Figure 16 was used with the ATS rotary furnace assembly to introduce a gas mixture of CH_4, H_2, and CO into the quartz reactor vessel. After passing through the reactor vessel, the gas mixture was scrubbed using a small glass scrubber filled with deionized water before being flared off through the same off gas burner used in the MTI furnace assembly. A schematic of the ATS rotary furnace assembly is presented in Figure 17.
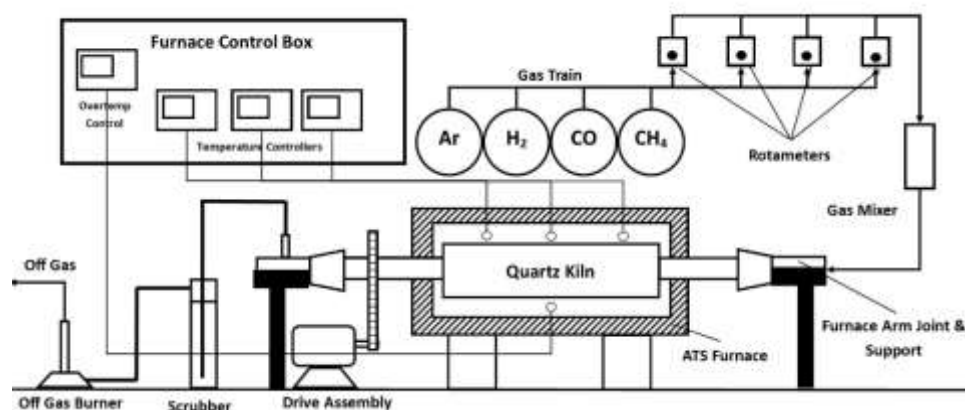
Figure 17: Rotary Furnace Assembly for Bulk Carburization of W-Loaded and Mo-Loaded Precursors

4.2. Precursor Development

4.2.1. W-Loaded Precursor

Tungsten carbide precursor material was produced by the adsorption of tungstate (WO_4^{2-}) ions onto the surface of activated carbon powder (Sigma-Aldrich, -100/+400 Mesh). Sodium tungstate ($Na_2WO_4 \cdot 2H_2O$) solutions were prepared by dissolving sodium tungstate powder in deionized water to produce solutions of varying concentration depending on the experiment. The pH of each solution was adjusted within the range of 2 to 6 using hydrochloric acid (HCl). To promote tungstate adsorption, sodium chloride was added to the solutions so that the NaCl concentration of each solution was approximately 0.2 M.

A series of six scoping experiments was carried out to determine the effect of initial tungstate concentration on tungstate adsorption as well as to establish boundary conditions for the design of experiments used to mathematically model ion adsorption behavior. For each experiment, a sodium tungstate solution was prepared in 100 mL of deionized water with the concentration of sodium tungstate varying between 1000 mg/L and 28,000 mg/L. Following the dissolution of the sodium tungstate, the solution pH was brought to 2.0 by the addition of HCl. After the pH stabilized, a 2.5 g sample of activated carbon was added to the solution and the

mixture was agitated using an orbital shaker set at 480 rpm in order to keep the activated carbon in suspension. After 24 h of agitation, the activated carbon was separated from the tungstate solution by vacuum filtration. The tungstate-loaded carbon was dried overnight at 80 °C in a drying oven while the remaining tungstate solution was analyzed via ICP-OES; the amount of tungstate adsorbed from solution was calculated by measuring the difference in solution concentration following exposure to the activated carbon.

Six additional scoping experiments were carried out to examine the effect of reaction time on the adsorption of tungstate ions from solution. The solution preparation procedure was the same for these six additional experiments with the exception that the tungsten concentration was held constant at 1000 mg/L. The six flasks were agitated on an orbital shaker table at 480 rpm for 4, 6, 8, 12, 24, and 48 h.

Based on the results of the scoping experiments and the tungsten adsorption literature search, a design of experiments matrix was developed using the statistical analysis and experimental design software, DesignExpert 9. The design of experiments, which consisted of 30 individual experiments, was used to evaluate the effects of varying reaction time, temperature, initial tungsten concentration, and pH on the adsorption of tungstate ions onto activated carbon. The upper and lower boundary conditions were established for each variable along with midpoint conditions that improved the prediction capability of the mathematical model. The high, low, and midpoint values for the four variables used to model W-adsorption behavior are presented in Table IV.

Table IV: High, Low, and Midpoint Values for the W-Adsorption Design Matrix

Variable	High	Midpoint	Low
Temperature (°C)	20	40	60
Time (h)	1	12.5	24
W-Conc. (mg/L)	1000	10,500	20,000
pH	2.0	4.0	6.0

The information collected from the design of experiments was used to mathematically model tungstate adsorption behavior and allowed for the statistical optimization of tungstate adsorption onto the activated carbon matrix.

Based on the findings of the design matrix experimentation, the adsorption process was scaled up in order to produce larger quantities of W-loaded precursor for carburization in the ATS rotary furnace. Scaled-up adsorption experiments were carried out using 2 L and 4 L solutions of Na_2WO_4/NaCl and 50 g and 100 g batches of activated carbon, respectively. The solutions were agitated using the impeller setup as shown in Figure 18.

Figure 18: Bulk Adsorption Assembly

Solution concentrations were held at 18,000 ppm W, 0.1 M NaCl, a pH of 2.0, and a total adsorption time of 2 h.

Solution samples from each experiment were analyzed for W concentration in units of mg/L using inductively coupled plasma-optical emission spectroscopy (ICP-OES). The post-

absorption W concentration was compared to the initial solution concentration and the amount of W adsorbed onto activated carbon was measured by difference.

4.2.2. Mo-Loaded Precursor

The development of Mo-loaded precursor followed a procedure similar to that of the W-loaded precursor. A design matrix was developed for Mo adsorption using the same parameters as the design matrix for W adsorption (see Table IV). Sodium molybdate ($Na_2MoO_4 \cdot 2H_2O$) was used as the water-soluble Mo source and a series of 30 experiments were carried out in order to produce the response surface model used to optimize Mo adsorption onto activated carbon.

Based on the results of the design matrix, Mo-adsorption was scaled up to 2 L solutions and 50 g of activated carbon. These scaled-up experiments were carried out using solutions with an initial concentration of 18,000 ppm Mo brought to a pH of 2 using HCl. The adsorption reaction was allowed to continue at 20 °C for 2 h before the solution was removed from the activated carbon using vacuum filtration. Following filtration, the Mo-loaded precursor was dried, and the remaining solution was analyzed for Mo concentration using ICP-OES. The amount of Mo-loading was determined by difference and compared to the values predicted by the response surface model.

4.2.3. Si-Loaded Precursor

A series of 18 scoping experiments was performed to assess the effect of pH on silicate adsorption onto activated carbon. Sodium metasilicate (Na_2SiO_3) was dissolved in 100 mL of deionized water to produce silicate solutions of 0.1, 1, 2, 5, 10, 20, and 50 g/L concentrations. Sodium chloride was added to half of the scoping experiments to determine its effect on silicate adsorption. Solutions were prepared at pH 2.0, 6.0, and the ambient silicate solution pH (11.6-11.9). A 2.5 g sample of activated carbon was added to each solution and the solutions were

agitated at 480 rpm on an orbital shaker table and allowed to mix for a series of reaction times (1, 12, or 24 h). In a manner similar to the tungstate adsorption experiments, the carbon samples were separated from the remaining solution by vacuum filtration. Hydrochloric acid was used to lower the pH of the silicate solutions, but experiments conducted at higher concentrations were inhibited by the formation of silica gel as the HCl additions induced a rapid precipitation of the silicate ions in sample solutions that contained more than 0.1 g/L sodium metasilicate. A series of 12 additional scoping experiments was performed at the ambient pH of the silicate solutions to determine the effect of increasing silicate concentrations on adsorption. Half of these experiments were carried out for an adsorption time of 12 h and the remaining experiments were carried out for 24 h. For all of the silicate adsorption experiments, the solutions were analyzed via ICP-OES.

A statistical design of experiments was used to optimize the adsorption of silicate anions onto the activated carbon matrix. A series of 20 individual experiments was carried out to determine the effects of initial Si concentration (ppm), temperature, and reaction time on adsorption. Initial Si concentrations were set at 10,000 ppm, 30,000 ppm, and 50,000 ppm, temperature was held at 20 °C, 40 °C, and 60 °C, and reaction time was held at 1 h, 12.5 h, and 24 h. In a manner similar to the procedure for tungstate and molybdate adsorption, a 2.50 g sample of activated carbon was added to each solution and the solutions were agitated on a hot plate/stir plate at 480 rpm. In contrast to the tungstate and molybdate solutions, a usable range for pH could not be determined for silicate adsorption due to the formation of a silica gel with the addition of any HCl. Because of this phenomenon, the ambient pH of the silicate solutions was used instead of pH as a variable for the response surface produced by the adsorption data.

To produce optimized silicate-loaded precursor, solutions with a Si concentration of 50,000 ppm were prepared by adding sodium metasilicate to 100 mL of deionized water. The solutions were agitated at 20 °C in the presence of 2.50 g of activated carbon at 480 rpm for 2 h. Following adsorption, the activated carbon was collected via vacuum filtration and dried before being used in carburization experiments.

4.3. Carburization

4.3.1. WC Synthesis

Initial carburization experiments were conducted in the MTI GSL 1100X tube furnace. Samples (1.25 g) of tungsten-loaded activated carbon were placed in ceramic boats and carburized for 20 h at 1000 °C under an inert argon atmosphere (250 mL/min). Further inert atmosphere carburization experiments were carried out at 1400 °C for 20 h using the MTI GSL 1500X tube furnace. Images of the MTI GSL 1100X and 1500X furnaces are presented in Figure 19.

(a)

(b)

Figure 19: Images of the MTI GSL 1100X (a) and MTI GSL 1500X (b) Tube Furnaces

Carburization experiments were also conducted using reducing gas atmospheres

consisting of H_2, CH_4, and CO mixtures. These carburization experiments were conducted using

the ATS rotary furnace with a quartz kiln body, and the gas mixtures were controlled with

Omega flowmeters. Figure 20 shows the rotary furnace apparatus.

Figure 20: ATS Rotary Furnace Setup for Carburization Experiments

Initial reducing gas carburization experiments consisted of four individual experiments

(RGC-1-RGC-4). The composition of the gas mixture used in these experiments was set at 60%

H_2, 25% CO, and 15% CH_4 by volume at a flow rate of 0.5 L/min. Experiments were carried out

with this gas composition at both 850 and 950 °C for 6 and 8 h. The tungstate-loaded activated

carbon charges (approx. 50 g) were heated to the specified temperature under a 0.5 L/min flow of

argon purge gas.

The composition of the reducing gas mixture was altered in an attempt to improve the

conversion of tungstate to tungsten carbide (RGC-9). A sample of precursor material weighing

27.22 g was added to the rotary kiln and heated to 950 °C at a rate of 6 °C /min under argon gas.

Once the temperature inside of the kiln reached the desired target, a reducing gas mixture

consisting of 40% H_2, 35% CO, and 25% CH_4 by volume was introduced to the furnace and the

precursor maintained constant temperature for 8 h. Further experimentation involved altering the

gas composition to a mixture consisting of 80% CH_4, 10% CO, and 10% H_2. In an attempt to

improve carburization of the W-loaded precursor, the precursor material was blended with virgin

activated carbon in a 1:1 mass ratio prior to carburization (RGC-17). Virgin activated carbon was also added to carburized precursor in a 1:1 mass ratio and the material was carburized a second time under the reducing gas mixture for an additional 8 h to further promote carburization (RGC-18).

The data from the scoping experiments were used to establish the boundary conditions for a design of experiments used to model the carburization behavior of the W-loaded precursor. A series of 19 experiments was carried out to measure the effects of temperature, reaction time, reducing gas atmosphere composition, and the amount of added activated carbon on the conversion of the W-loaded precursor to WC. The amount of activated carbon was measured as a weight percent of the total furnace charge, gas atmosphere composition was measured as a ratio of methane to hydrogen (CH_4:H_2), temperature in °C, and reaction time in hours.

W-loaded precursor was blended in a ceramic ball mill with unloaded activated carbon for five minutes to produce 25 g samples that contained 20%, 35%, and 50% unloaded activated carbon by weight. These samples were heated inside the rotary kiln under argon at a rate of 5.3 °C /min until reaching a desired carburization temperature of 850 °C, 900 °C, or 950 °C. Once the kiln interior was at the required carburization temperature, a reducing gas mixture consisting of CH_4, H_2, and CO was introduced. Carbon monoxide was always present as 10% of the total flow (0.5 L/min) by volume while the ratio of methane to hydrogen was altered to 2:1, 5:1, and 8:1. Samples were held at the desired carburization temperature for 6, 7, and 8 h before being cooled to room temperature under argon. The carburized products were then collected and analyzed by X-ray diffraction (XRD) and scanning electron microscopy (SEM). The experimental conditions for each experiment carried out for the 2-factorial design of experiments are presented in Table V.

Table V: Experimental Conditions for the W-Carburization Design of Experiments

Sample Name	Time (h)	Temperature (°C)	Added C Content (% AC)	Gas Composition (CH$_4$:H$_2$)
WCDM1	6	850	20	2
WCDM2	8	850	20	2
WCDM3	6	950	20	2
WCDM4	8	950	20	2
WCDM5	6	850	50	2
WCDM6	8	850	50	2
WCDM7	6	950	50	2
WCDM8	8	950	50	2
WCDM9	6	850	20	8
WCDM10	8	850	20	8
WCDM11	6	950	20	8
WCDM12	8	950	20	8
WCDM13	6	850	50	8
WCDM14	8	850	50	8
WCDM15	6	950	50	8
WCDM16	8	950	50	8
WCDM17	7	900	35	5
WCDM18	7	900	35	5
WCDM19	7	900	35	5

All carburized samples were analyzed via X-ray diffraction using a Rigaku Ultima IV X-ray diffractometer with Cu-Kα radiation at 40 kV and 40 mA. The carburized samples were ground to -325 Mesh using a mortar and pestle and packed onto a powder XRD slide. Qualitative analyses of all samples were done using the Whole Powder Pattern Fitting (WPPF) method. Images of the carburized products were taken using a LEO 1430VP and a Tescan Mira 3 scanning electron microscope. Samples were stub-mounted and carbon-coated prior to analysis.

4.3.2. Mo$_2$C Synthesis

Initial Mo carburization experiments consisted of a series of three carburization experiments on molybdate-loaded precursor under an Ar atmosphere at 1100 °C for reaction times of 4, 8, and 12 h. A series of three carburization scoping experiments was carried out to assess the effect of a reducing gas atmosphere on the carburization of the Mo-loaded precursor. The temperature in each experiment was held constant at 600 °C under a constant flow of H$_2$ (0.5 L/min) while the reaction time was held at 4, 6, and 8 h. The molybdenum carburization experiments were carried out inside an MTI-1500x GSL tube furnace and all carburized samples were analyzed using XRD.

Additional carburization experiments were carried out at varying temperatures below 1100 °C using a reducing gas mixture of CH$_4$, H$_2$, and CO. Carburization of the Mo-loaded precursor was carried out for 8 h at 800 °C (MoRGC-7), 900 °C (MoRGC-8), and 1000 °C (MoRGC-9) under a reducing gas atmosphere consisting of 80% CH$_4$, 10% H$_2$, and 10% CO. Further experimentation was carried out to investigate carburization of the Mo-loaded precursor at 700 °C, 725 °C, 750 °C, and 775 °C under the reducing gas mixture.

A 2-factorial design of experiments was prepared using DesignExpert9 software consisting of 11 carburization experiments to determine the effects of temperature, time, and gas composition on the carburization of the Mo-loaded precursor. These experiments were carried out using the experimental conditions presented in Table VI.

Table VI: Experimental Conditions for the Mo-Carburization Design of Experiments

Sample Name	Time (h)	Temperature (°C)	Gas Composition (CH$_4$:H$_2$)
Mo_DM1	1.0	500.0	2.9
Mo_DM2	8.0	500.0	2.9
Mo_DM3	1.0	850.0	2.9
Mo_DM4	8.0	850.0	2.9
Mo_DM5	1.0	500.0	8.0
Mo_DM6	8.0	500.0	8.0
Mo_DM7	1.0	850.0	8.0
Mo_DM8	8.0	850.0	8.0
Mo_DM9	4.5	675.0	5.0
Mo_DM10	4.5	675.0	5.0
Mo_DM11	4.5	675.0	5.0

Carburization experiments were conducted in the ATS 3210 tube furnace. Samples of Mo-loaded precursor were prepared in 25 g batches and loaded into a fused quartz kiln (Allen Scientific Inc.). An image of the quartz kiln used in the carburization experiments is presented in Figure 21.

Figure 21: Image of Fused Quartz Kiln

The samples of Mo-loaded precursor were heated to a specified carburization temperature (500 °C, 675 °C, or 850 °C) at a rate of 5.3 °C /min under a constant flow of argon gas (0.5 L/min). Once the sample reached the specified carburization temperature, the argon atmosphere was replaced with a mixture of CH_4, H_2, and CO gas. The total flowrate of the gas mixture was held constant at 0.5 L/min. The volumetric ratios of methane and hydrogen were altered for each experiment while the flowrate of carbon monoxide was fixed at 10% of the total volume. Samples were held at temperature for 1, 5, and 8 h after which the reducing gas mixture was replaced with argon gas and the carburized samples were cooled to room temperature. Once the samples reached ambient conditions, the samples were removed from the kiln and analyzed via XRD and SEM.

4.3.3. SiC Synthesis

Si-loaded precursor was carburized in an MTI-1500x GSL tube furnace. To assess the effect of temperature on carburization, samples of Si-loaded precursor were carburized for 1400 °C, 1300 °C, and 1200 °C for 20 h under a continuous Ar purge set at a flow rate of 0.5 L/min. The effect of time on carburization was analyzed by carburizing Si-loaded precursor samples at

1200 °C for 4, 6, and 8 h under an atmosphere of H_2 (0.5 L/min). All samples were initially heated under Ar gas to 200°C at 5 °C /min and held at this temperature for 20 min. Then, samples were heated to 600 °C at a rate of 10 °C /min and held at this temperature for an additional 20 min. At this point, samples were heated to the desired experimental temperature at a rate of 6-8 °C /min. For the experiments conducted under H_2, the reducing gas atmosphere was introduced to the furnace only when the furnace reached the desired experimental temperature. Following the allotted carburization time, any reducing gas atmosphere was removed from the furnace by a purge flow of Ar gas and the samples were cooled to ambient conditions under an inert Ar atmosphere.

Carburized samples were analyzed by XRD and SEM. Carburized Si-loaded precursor samples were ground to -325 Mesh using a micronizer mill. Before being micronized, a small amount of zinc oxide (ZnO), equal to 10 wt% of the carburized sample, was added as a semi-quantitative method of measuring changes in the amount of SiC produced during carburization.

4.4. Modeling and Optimization

Both adsorption and carburization behavior were modeled and optimized using DesignExpert 12 (StatEase Inc.), a statistical analysis software that utilizes response surface methodology to determine the effect of multiple variables on a selected response. Model selection was an iterative process and involved the comparison of multiple mathematical models. In order to model adsorption and carburization behavior, mathematical transformations were performed on the experimental data to normally distribute each data set and allow for trends to be observed. The mathematical transformations, generally power functions, were selected by the application of the Box-Cox plot, a statistical diagnostic that assigns a value, λ, which corresponds to the power function best suited for transforming the data set to fit a normal

distribution [87]. Adsorption behavior was modeled using a central composite response surface design while carburization behavior was modeled using a 2-level factorial design (2FI). Each model was verified using multiple statistical diagnostic methods including Analysis of Variance (ANOVA), Leverage vs. Run, and Cook's Distance plots to assess the overall fit of the selected model to the data set, the influence of individual data points on the overall model, and the possibility of individual data points existing as outliers, respectively.

4.4.1. Precursor Development

Statistical models were prepared for each of the three anion loaded precursors using the ICP-OES results for adsorption. A face-centered distribution was used with these designs of experiments due to precipitation problems observed during previous experimentation at pH levels below 2.0 for tungstate and molybdate solutions.

The tungstate and molybdate adsorption process were modeled using a central composite design of experiments with four independent variables: temperature (°C), reaction time (h), pH, and initial anion concentration (ppm), resulting in a series of 24 experiments with six mid-point experiments to account for curvature. Tungstate adsorption behavior was modeled using an inverse square root transform in conjunction with a modified quadratic model while molybdate adsorption behavior was modeled using a base 10 logarithmic transform in conjunction with a modified quadratic model.

Silicate adsorption was modeled using a three-variable central composite design of experiments. The data was modeled using an inverse square root transform in conjunction with a modified linear model. The addition of any HCl to solutions of concentrated sodium silicate resulted in the rapid precipitation of SiO_2 and the conversion of the solution into a silica gel. Because of the precipitation issues with silicate solutions, it was not possible to consider pH as a

controllable variable in the silicate adsorption process for the purposes of statistical modeling

although pH has been shown to affect adsorption in dilute silicate solutions [83]. The silicate

adsorption behavior design of experiments included 14 individual experiments with an additional

six midpoint experiments to account for curvature. Adsorption behavior was modeled using an

inverse square root transform in conjunction with a modified quadratic model. The experimental

data for each of the adsorption design matrices are available in the appendix.

4.4.2. Carburization Modeling

Carburization of the W-loaded precursor was modeled using a power series transform (λ

$= 2.07$) in conjunction with a modified 2FI model. Mo-carburization data was modeled using a

square root transform and a modified 2FI model. Modeling was carried out using the WPPF

relative weight percentages of Mo_2C or WC from the XRD data from each carburization

experiment. The experimental data for the carburization design matrices are available in the

appendix.

4.5.   Separation

Following carburization, the carbide products, in this case a mixture of WC, W_2C and W,

were liberated from the residual activated carbon matrix by grinding the carburized products in a

Union Process-Szegvari Attritor BATCH-LAB type stirred ball mill and, later, a Sturtevant OM2

micronizer equipped with a tungsten carbide impact chamber. The stirred ball mill ground

samples using steel grinding media to break apart the carburized precursor while the micronizer

used pressurized air to cause a constant stream of particles to collide at high speeds with the

interior walls of the impact chamber as well as the particles themselves. Images of both the

micronizer and stirred ball mill are shown in Figure 22.

(a)   **(b)**

Figure 22: Union Process-Szegvari Attritor Stirred Ball Mill (a) and Sturtevant Micronizer (b)

Samples of carburized material were added to the stirred ball mill and ground for 45 min in the presence of denatured ethanol using a charge of steel balls. Following milling, the carburized material was removed from the mill and the ethanol was removed by evaporation. A heavy density separation was then carried out using lithium metatungstate (LMT) to separate the less dense activated carbon matrix from the denser carburized material. Samples of milled material were placed added to centrifuge tubes containing LMT solution and centrifuged for 60 minutes. Following centrifugation, the high-density material was removed and passed through a syringe filter before being stub-mounted, and gold-coated for SEM analysis.

Carburized material was fed into the micronizer in approximately 50 g batches at a feed pressure of 40 psi and a grind pressure of 78 psi. Following grinding, the high-density material was separated using centrifugation in LMT and the solids were collected via pressure filtration. Following filtration, the material was dried, stub-mounted, and gold-coated in preparation for SEM analysis.

Additional methods of separation were investigated using a surrogate material to represent liberated carbide particles interspersed with the residual carbon matrix. Tungsten carbide particles measuring 1.7 microns in diameter (Kennametal) were blended with the activated carbon used to produce the W-loaded precursor. Ten grams of activated carbon were blended with one to three grams of the purchased WC powder depending on the separation experiment.

Surrogate samples were then passed through a Mac Technologies Warman M16 Hydrocyclosizer to separate the larger carbon particles (>10 microns) from the carbide particles that were collected alongside the smaller carbon particles in the outlet flow of the hydrocyclosizer. The hydrocyclosizer uses a series of vortexes to separate particles by size and density. An image of the hydrocyclosizer is presented in Figure 23.

Figure 23: Image of the Warman M16 Hydrocyclosizer

Excess water was removed by decantation before the remaining slurry was introduced to a 300 mm diameter watch glass rotated at 27 rpm to produce a standing wave through the slurry. After several minutes, higher density particles collected in the center of the watch glass while lower

density particles were allowed to flow over the edge of the watch glass with the water. The

material that remained on the watch glass was then dried and collected for analysis via SEM

using Energy Dispersive X-ray Analysis (EDAX). An illustration of the standing wave

separation apparatus is presented in Figure 24.
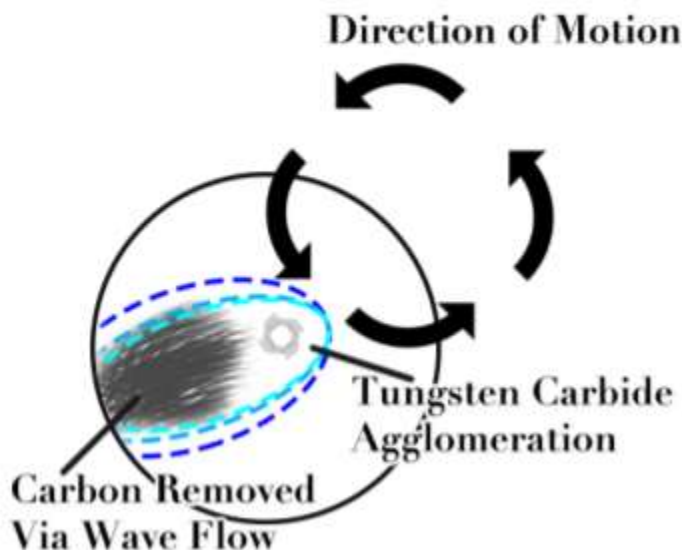
Figure 24: Illustration of the Standing Wave Separation Apparatus [88]

The standing wave separation process was further developed through attempts to improve

carbon-carbide separations by adding surfactants. Initial experiments used 15 µL/L Maxim

Manual Dishwashing Liquid (KS 2202) to promote separation. Later experiments used either

sodium dodecylsulfate (SDS) or sodium dodecylbezenesulfonate (SDDS) obtained from Sigma

Aldrich. Surfactant concentrations were varied between 25 and 400 µL/L. Samples were

analyzed for W concentration using EDAX to determine the effectiveness of the separation.

Following the surrogate sample experiments, the cyclosizer/standing wave separation

process was applied to carburized W-loaded precursor that had been processed via jet mill prior

to separation. Based on the surrogate samples, SDS was used as the surfactant to promote

carbon-carbide separation [88].

5. Results and Discussion

5.1.   Precursor Development and Optimization

5.1.1. W-Loaded Precursor Development and Optimization

The results from the concentration study experiments are presented in Figure 25. The initial concentration of $Na_2WO_4 \cdot 2H_2O$ is presented on the x-axis while tungstate anion adsorption is defined on the y-axis as a percentage based on the amount of tungsten removed from solution determined by difference via ICP-OES.
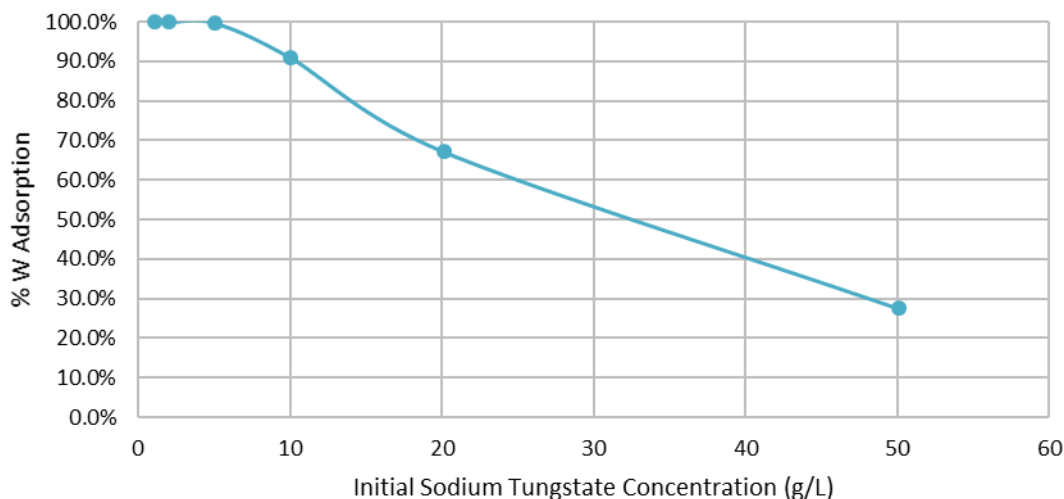
Figure 25: Tungsten Adsorption vs Initial Sodium Tungstate Concentration

The graph shows that nearly all of the tungstate anions were removed from solution at initial concentrations of $Na_2WO_4 \cdot 2H_2O$ less than 5 g/L. Tungstate adsorption sharply decreased once solution concentrations exceeded 10 g/L and adsorption dropped below 70% at a solution concentration of 20 g/L.

Tungstate loading was also expressed as an adsorption isotherm in order to determine a range of concentrations suitable for carburization precursor production. The tungstate adsorption isotherm is presented in Figure 26. Tungstate adsorption is defined on the y-axis as milligrams of

tungsten per gram of activated carbon (mg/g), while initial tungstate concentration is defined on

the x-axis as milligrams of $Na_2WO_4 \cdot 2H_2O$ per liter of solution.
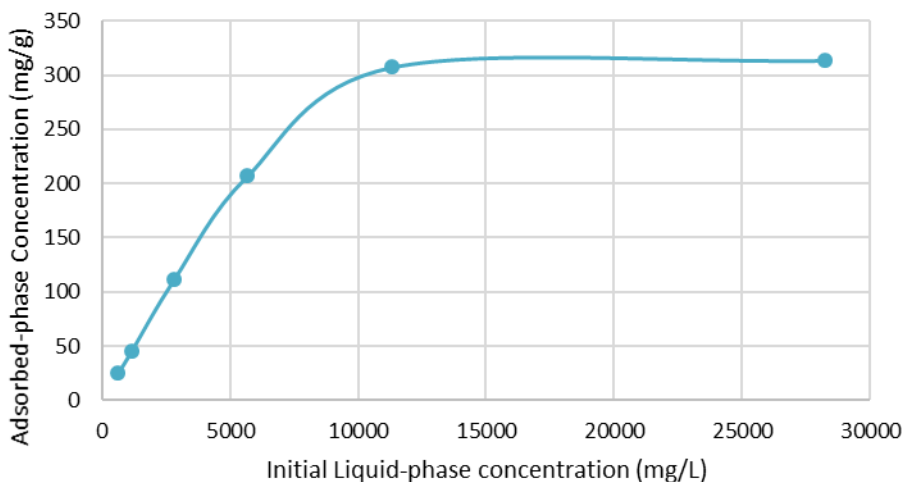
Figure 26: Tungstate Adsorption Isotherm

Tungstate loading increased with increasing initial concentration until a loading "plateau" of

approximately 300 mg/g was achieved at approximately 15,000 mg/L. From the data presented

in Figure 25 and Figure 26, it was determined the upper bound for initial concentration in the W-

adsorption design of experiments would be 20,000 mg/L $Na_2WO_4 \cdot 2H_2O$ and the lower bound

was fixed at 1000 mg/L $Na_2WO_4 \cdot 2H_2O$. Based on the six scoping experiments, an initial

concentration of 20,000 mg/L $Na_2WO_4 \cdot 2H_2O$ should be more than sufficient to enable maximum

loading of the activated carbon while still removing a relatively high percentage of the tungstate

ions (~70%) from solution. Both the amount, and the percentage, of tungstate removed from

solution are important factors to consider when developing this process because, while it is

important to produce the greatest mass of carbide product possible, it is also critical that reagents

are not wasted in the production of the carburization precursor. As part of this process, anion

solutions could be recycled, and the concentration of anions restored to initial amounts for use in

subsequent adsorption runs.

The data from the scoping experiments were also fitted to both the Freundlich and Langmuir adsorption models in order gain a better understanding of the nature of the tungstate adsorption process. The Freundlich model of tungstate adsorption is presented in Figure 27. Initial $Na_2WO_4 \cdot 2H_2O$ concentration (Ce) is defined as a logarithmic function on the x-axis in mg/L while the amount of tungstate adsorbed onto activated carbon (qe) is also defined as a logarithmic function on the y-axis in mg (W) per gram of activated carbon (mg/g).
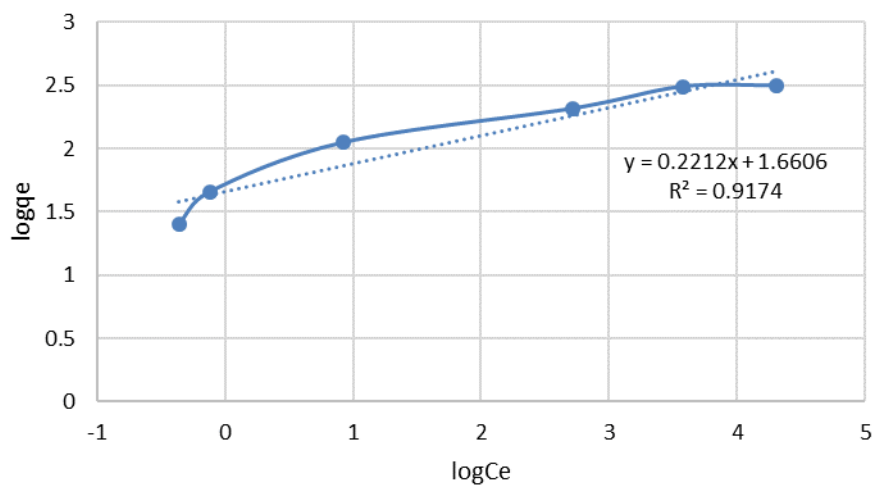
Figure 27: Freundlich Model of Tungstate Adsorption

The Langmuir model of tungstate adsorption is presented in Figure 28. Initial $Na_2WO_4 \cdot 2H_2O$ concentration is presented on the x-axis in units of mg/L and tungstate adsorption is represented on the y-axis as initial $Na_2WO_4 \cdot 2H_2O$ concentration divided by the mass of adsorbed tungsten per gram of activated carbon. This ratio is therefore defined in units of liters of solution per gram of activated carbon (L/g).
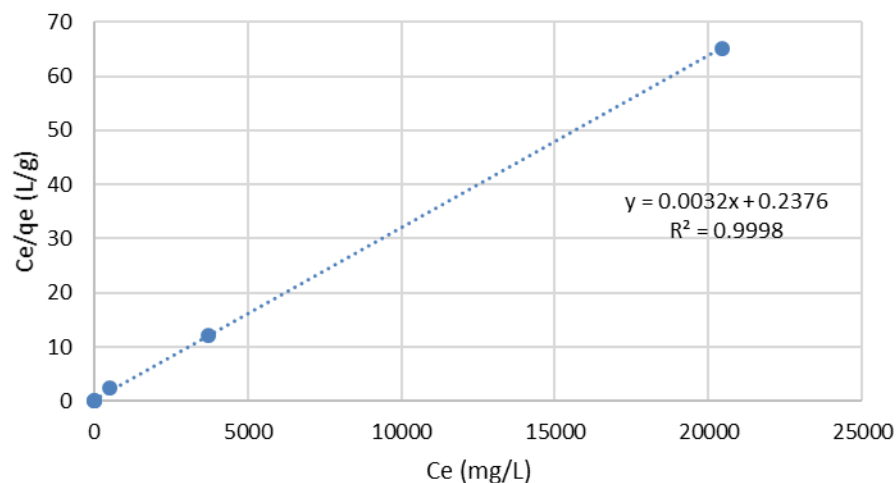
Figure 28: Langmuir Model of Tungsten Adsorption

Comparison of the R-squared values for both models revealed that the data better fit the Langmuir model of adsorption. Langmuir adsorption behavior is an indication that monolayer adsorption is occurring between the activated carbon and tungstate anions rather than a stacking mechanism of multiple anions on top of one another.

Tungstate adsorption behavior was modeled using an inverse square root transform and a modified quadratic model. The ANOVA results and fit statistics for the selected adsorption model are presented in Table VII.

Table VII: ANOVA for W-Adsorption Model

Source	p-value
Model (Mod. Quadratic/Inverse Sqrt Transform)	< 0.0001
Initial W Concentration (mg/L)	< 0.0001
pH	< 0.0001
Concentration-pH Interaction	< 0.0001
Concentration^2	< 0.0001
Fit Statistics	
R-squared	0.9931
Adjusted R-squared	0.9920
Predicted R-squared	0.9907
Adequate Precision	70.8653

The ANOVA data show that the chosen model is statistically significant, and that adsorption behavior is governed by two major factors: Initial W concentration and pH. Reaction time and temperature were not statistically significant factors within the observed design space. The insignificance of reaction time should not be interpreted as an indication that reaction kinetics are not affecting adsorption, but rather that, within the time parameters established for the process design space (1-24 h), there was no statistically significant effect on adsorption by varying reaction times. Tungstate adsorption onto the activated carbon occurs rapidly (less than 1 h) and this behavior allows for short adsorption times to be used when producing W-loaded precursor.

The fit statistics also support the use of the selected model. Not only is the R-squared value for the model close to 1.0, it is also in good agreement with both the adjusted and predicted

R-squared values. The adequate precision value is also relatively large (>8), which, along with other diagnostic tests, indicates that the selected model should have strong predictive power.

Figure 29 and Figure 30 contain diagnostic plots used to validate the selected adsorption model. Figure 29 contains a Normal Distribution plot of the data residuals as well as a Predicted vs. Actual Plot. Figure 30 is a graph of the leverage values associated with each experiment as well as a plot of the Cook's Distance values for each data point.
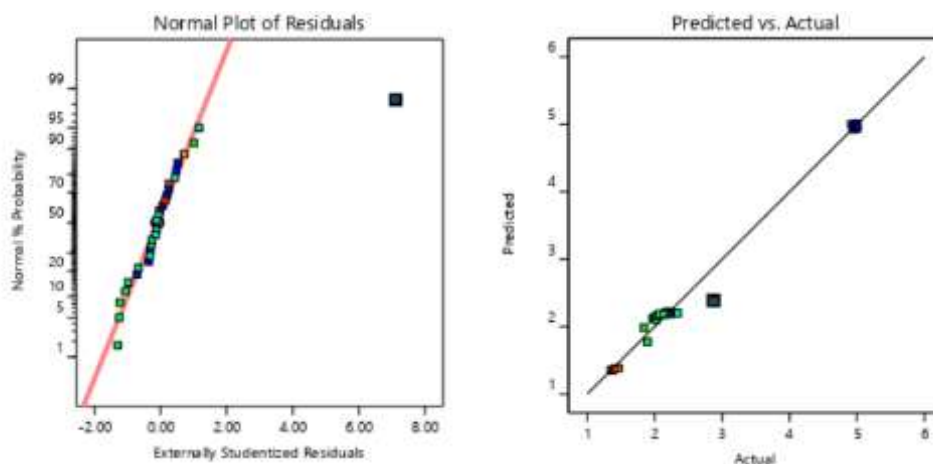
Figure 29: Normal Distribution and Predicted vs Actual Plots for the Tungstate Adsorption Model

The adsorption data fit well to the normal distribution line with the exception of a single point. Although this result could be an indication of an outlier point, the same point is shown to fit well to the trend line produced by the Predicted vs. Actual plot.
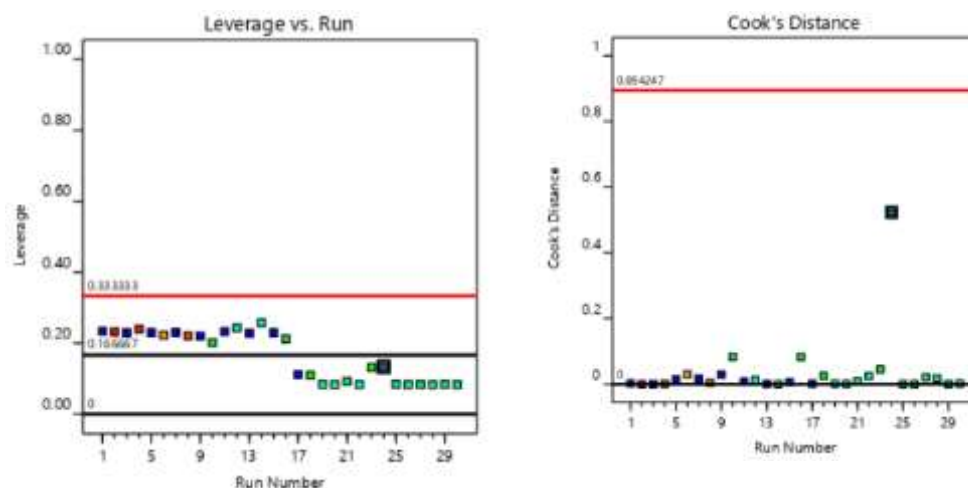
Figure 30: Leverage and Cook's Distance Diagnostic Plots for the Tungstate Adsorption Model

The same point that did not align well with the normal distribution plot does not possess a leverage value or a Cook's Distance value that would support it being removed from the data set as an outlier. None of the leverage or Cook's Distance values for the other data points lie outside of the control (red line), indicating that none of the points induced an excessive amount of influence onto the adsorption model.

A three-dimensional plot of the response surface adsorption model is presented in Figure 31. The model was produced from the following program-generated expression:

$$\frac{1}{\sqrt{gW/gC}} = 0.034320 - 3.09986 \times 10^{-6}C_W + 9.72219 \times 10^{-6}pH + 6.50037 \times 10^{-8}C_W pH + 8.4568 \times \quad (31)$$

$$10^{-11}C_W{}^2 ,$$

Where tungsten adsorption, gW/gC, is expressed as a function of initial tungsten concentration (C_W) and pH. Solution pH and initial tungstate concentration are defined on the x and y axes with initial tungstate concentration presented in units of mg of tungsten per liter of solution (mg/L). Tungstate loading is presented on the z-axis in units of grams of tungsten per g of activated carbon (g W/g C). Temperature and reaction time are held constant at 20 °C and 1 h respectively.
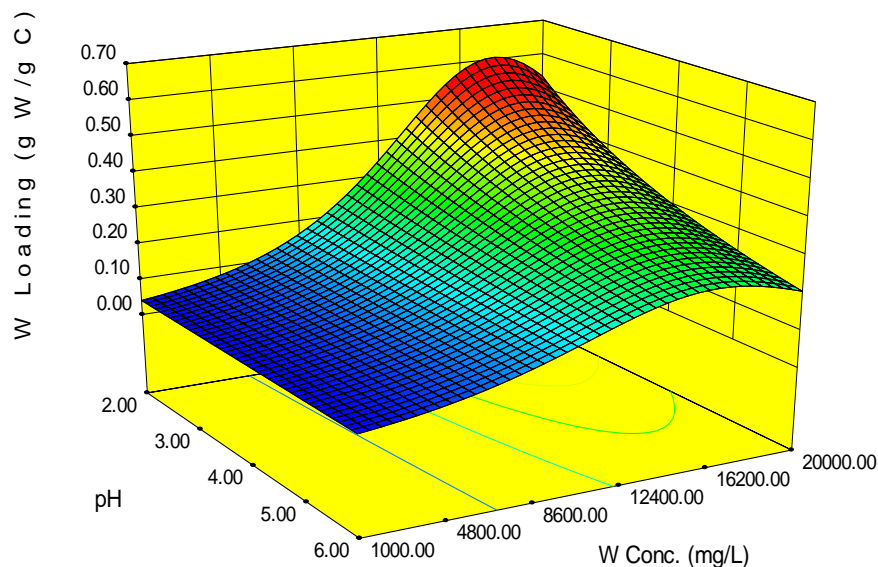
Figure 31: Response Surface Model of Tungstate Adsorption Behavior (1 h Reaction Time) [89]

The adsorption model shows tungstate anion adsorption improves as pH decreases when the initial tungsten solution concentration remains between 17,000 mg/L and 19,000 mg/L. In order to maximize tungstate adsorption, optimal parameters were determined to be a solution pH of 2, an initial tungsten concentration of 18,000 mg/L, an adsorption time of 2 h, and a solution temperature of 20 °C. These conditions were used for the scaled-up adsorption experiments to produce 50 g and 100 g batches of precursor material for the carburization experiments. ICP-OES results from these scaled-up adsorption experiments determined that 0.35 g W/g C was achievable under these conditions.

5.1.2. Mo-Loaded Precursor Development and Optimization

Because of the chemical similarities between tungsten and molybdenum, it was determined that the parameters for W-adsorption would be used to optimize the production of the Mo-loaded precursor. The ANOVA data for the selected Mo-adsorption model is presented in Table VIII.

Table VIII: ANOVA for Mo-Adsorption Model

Source	p-value
Model (Mod. Quadratic/Log Transform)	< 0.0001
Initial W Concentration (mg/L)	< 0.0001
pH	< 0.0001
Concentration-pH Interaction	< 0.0001
Concentration^2	< 0.0422
Fit Statistics	
R-squared	0.9814
Adjusted R-squared	0.9785
Predicted R-squared	0.9682
Adequate Precision	55.3932
Lack of Fit	0.0302

The ANOVA data shows that the modified quadratic model is statistically significant and that the only statistically significant factors affecting Mo-adsorption are pH, initial Mo concentration, and the squares of these factors. Further support for the validity of this model comes from the high R-squared value and how well that R-squared value agrees with both the Adjusted and Predicted R-squared values. This model also has a high Adequate Precision value (55.3932) that indicates that the presented model should be able to predict adsorption values within the design space. A point of concern with this model was observed in the Lack of Fit value being statistically significant. However, due to the quality of the other ANOVA values, it

was decided to continue with the use of this model and rely upon other diagnostic methods

(Predicted vs. Actual, Normal Distribution plots, etc.) to determine the model's validity.

Diagnostic plots for the Mo-adsorption model are presented in Figure 32 and Figure 33.

Figure 32 contains a Normal Distribution plot of the data residuals as well as a Predicted vs.

Actual Plot. Figure 33 contains a graph of the leverage values associated with each experiment as

well as a plot of the Cook's Distance values.
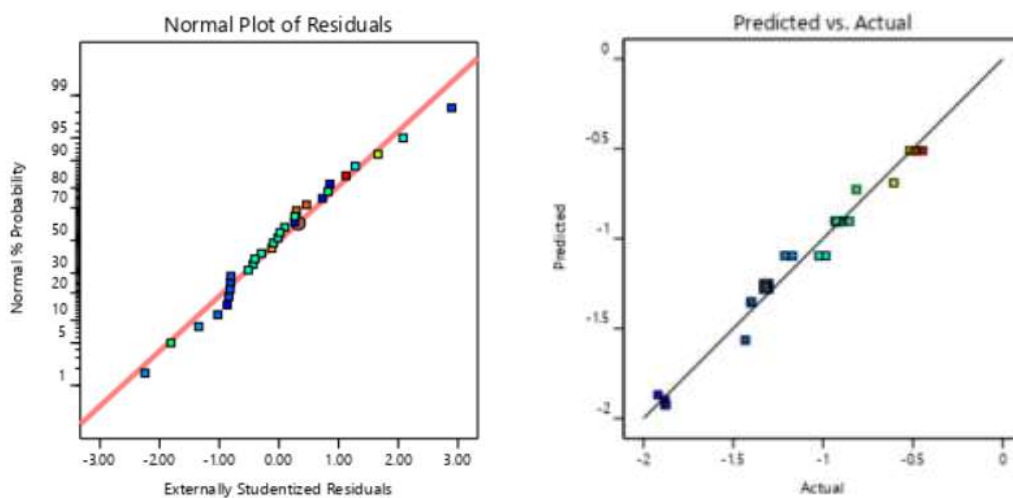
Figure 32: Normal Distribution and Predicted vs Actual Plots for the Molybdate Adsorption Model

Both diagnostic plots in Figure 32 show that the model data agrees with expected trends

with little deviation from ideal values. These two plots support the use of the presented model

despite the significant Lack of Fit value.
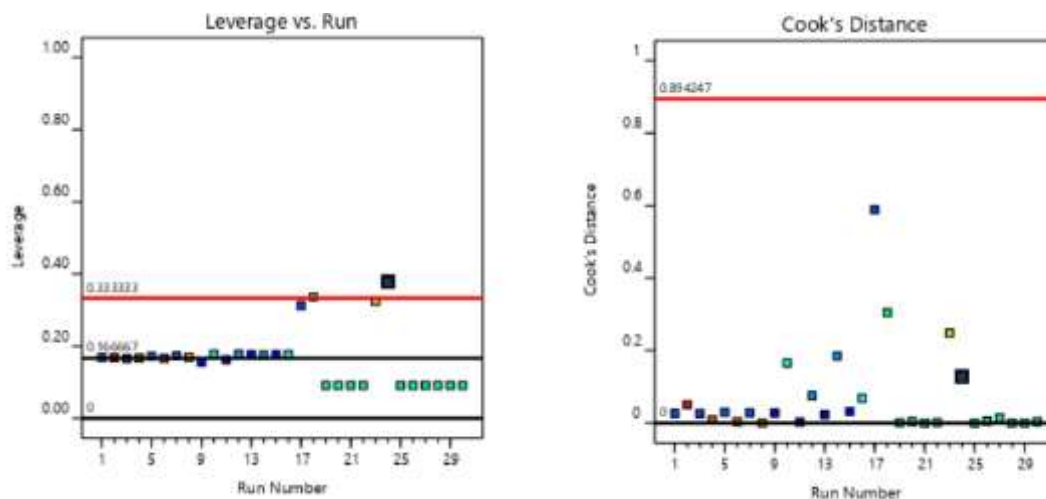
Figure 33: Leverage and Cook's Distance Diagnostic Plots for the Molybdate Adsorption Model

The leverage plot shows that one of the data points (experiment 24) had a greater degree of influence over the model than most of the other data points. However, this same data point does not have a Cook's Distance value high enough to be considered an outlier. It was proposed that the influence of experiment 24 was causing orthogonality problems within the model and an attempt to improve the model by removing this data point was attempted. However, the exclusion of experiment 24 resulted in an overall decrease in the quality of the model diagnostics while also not inducing an insignificant Lack of Fit value.

Despite the significant Lack of Fit value determined by ANOVA, it was decided, based on the quality of all other model diagnostics, that the presented model best represented the Mo-adsorption data. This model was used to predict optimal adsorption process parameters with the goal of maximizing Mo-adsorption.

A three-dimensional representation of the response surface model for Mo-adsorption is shown in Figure 34. The model was produced from the following program-generated expression:

$$\log_{10} gMo/gC = -1.381 + 1.028 \times 10^{-4}C_{Mo} + 1.404^{-3}pH - 2.794 \times 10^{-9}C_{Mo}^2 - 0.018pH^2, \tag{32}$$

Where molybdenum adsorption, *gMo/gC*, is expressed as a function of initial molybdenum concentration (*CMo*) and pH. Solution pH and initial molybdate concentration are defined on the x and y axes with initial molybdate concentration presented in units of mg of molybdenum per liter of solution (mg/L). Molybdate loading is presented on the z-axis in units of grams of molybdenum per g of activated carbon (g Mo/g C). Temperature and reaction time are held constant at 20 °C and 1 h respectively.
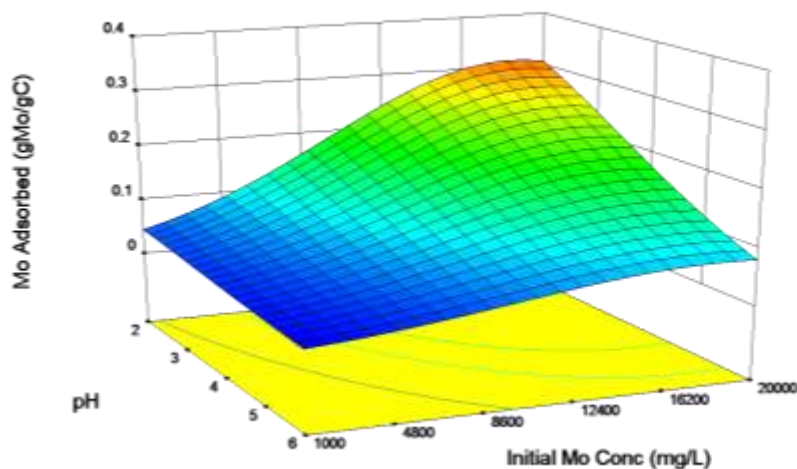
Figure 34: Response Surface Model of Molybdate Adsorption Behavior [90]

The response surface plot shows a region where a maximum adsorption value of approximately 0.3 g Mo/ g C is possible. Using the Point Prediction component of the DesignExpert 12 software, a set of optimal adsorption conditions was established. These conditions are presented in Table IX.

Table IX: Mo-Adsorption Model Verification Parameters and Confidence Interval for Predicted Values

Initial Mo Concentration (mg/L)	18,000
Reaction Time (h)	2
pH	2.0
Temperature (ºC)	20
Predicted Mean (g Mo/g C)	0.314
Predicted Median (g Mo/g C)	0.311
95% C. I. Low (Mean)	0.279
95% C. I. High (Mean)	0.353

The optimal adsorption conditions were predicted to produce a mean adsorption value of 0.314 g Mo/g C with a 95% confidence interval ranging from 0.279 to 0.353 g Mo/g C. To determine the ability of the model to predict new data points within the design space, a series of four confirmation experiments were carried out using the optimal adsorption parameters. The results from these confirmation experiments are presented in Table X.

Table X: Results from Mo-Adsorption Confirmatory Experiments

Confirmatory Experiment	Mo Adsorption (g Mo/g C)
Mo-1	0.33
Mo-2	0.32
Mo-3	0.32
Mo-4	0.31

Each of the adsorption values produced by the confirmatory experiments fell within the 95% confidence interval for the optimal adsorption parameters. The confirmatory experiment

results show the power of the model to predict new points within the design space despite the

significant Lack of Fit value produced by ANOVA. It was decided, based on the quality of all

other model diagnostics, and the predictive power of the model demonstrated by the

confirmatory experiments, that the presented model best represented the Mo-adsorption data.

This model was used to predict optimal adsorption process parameters with the goal of

maximizing Mo-adsorption. The experimental parameters in Table IX were used in scale-up

batches to produce Mo-loaded precursor for use in reducing gas carburization experiments.

5.1.3. Si-Loaded Precursor Development and Optimization

The results of the silicate adsorption scoping experiments carried out at 0.1 g/L Na_2SiO_3

are presented in Figure 35. Each line represents a different pH and NaCl content. Time is defined

in hours (h) on the x-axis while silicate adsorption is presented on the y-axis in units of mg Si/g

C.
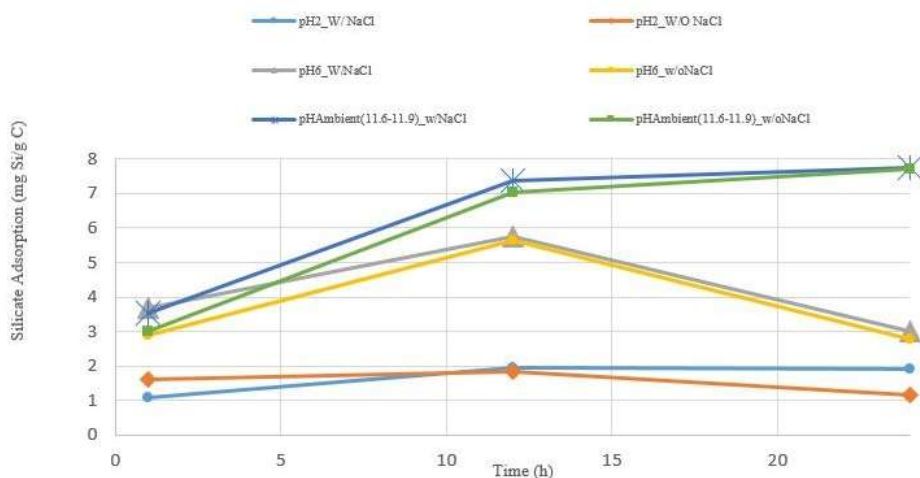
Figure 35: Silicate Adsorption Scoping Experiments (Time and pH)

The results show that NaCl addition had little effect on silicate adsorption while pH was

found to significantly effect silicate loading with the highest amounts of loading occurring within

the ambient solution pH range (11.6-11.9). Attempts to investigate pH effects at higher initial

concentration were unsuccessful due to the precipitation of a silica gel in the presence of HCl at

concentrations higher than 0.1 g/L Na_2SiO_3.

The results from additional scoping experiments investigating the effect of initial silicate

concentration on adsorption are presented in Figure 36. Initial silicate anion concentration is

defined on the x-axes in mg of Si per liter of solution (mg/L) while adsorption is defined on the

y-axis in mg of Si per gram of carbon (mg Si/g C).
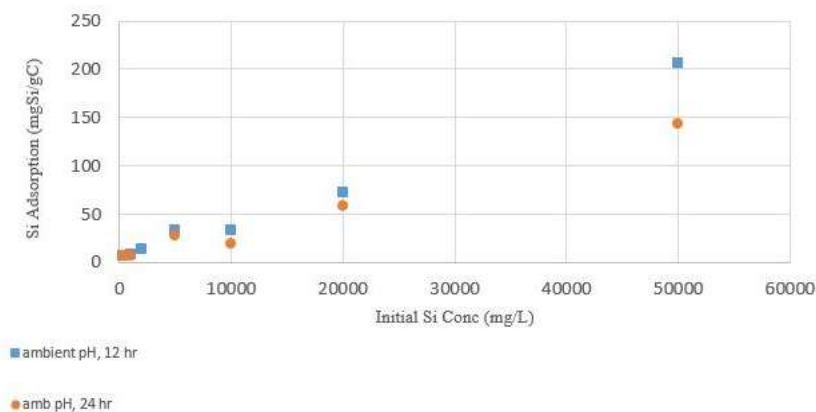
Figure 36: Silicate Adsorption Scoping Experiments (Initial Si Concentration)

In a manner similar to the tungstate adsorption scoping experiments, Si-loading was

found to increase with increasing concentration. To conserve reagents, initial concentration was

limited to 50,000 mg/L Si which produced the highest observed loadings at approximately 200

mg Si/g C. Experiments conducted at a 12 h reaction time were also found to produce higher

loading values than the 24 h adsorption experiments. This behavior indicated that the silicate

anions may desorb from the carbon matrix if allowed to remain suspended in solution for too

long. From these scoping experiments, the boundary conditions for the Si-adsorption design

matrix were determined.

The ANOVA results from the statistical model for Si-adsorption behavior are presented

in Table XI.

Table XI: ANOVA for Si-Adsorption Model

Source	p-value
Model (Mod. Linear/Inverse Sqrt. Transform)	< 0.0001
Initial Si Concentration (mg/L)	< 0.0001
Fit Statistics	
R-squared	0.8170
Adjusted R-squared	0.8068
Predicted R-squared	0.7691
Adequate Precision	17.9317
Lack of Fit	0.5319

The adsorption results show that the only statistically significant variable tested in the design matrix was the initial concentration of silicate anions in solution. The selected model for Si-adsorption behavior was found to be significant and the p-value for the Lack of Fit was greater than 0.05 indicating an insignificant Lack of Fit that further supports the selected model. The selected model does have a lower R-squared value associated with it compared to the other adsorption models. However, it is in good agreement with the Adjusted and Predicted R-squared values and is still large enough to consider the selected model for predicting adsorption behavior. The satisfactory predictive power of the model is shown by the Adequate Precision value of 17.9317.

Diagnostic plots for the selected Si-adsorption model are presented in Figure 37 and Figure 38. A Predicted vs Actual plot and Normal Distribution plot are presented in Figure 37 and Leverage Plot and a Cook's Distance plot are presented in Figure 38.
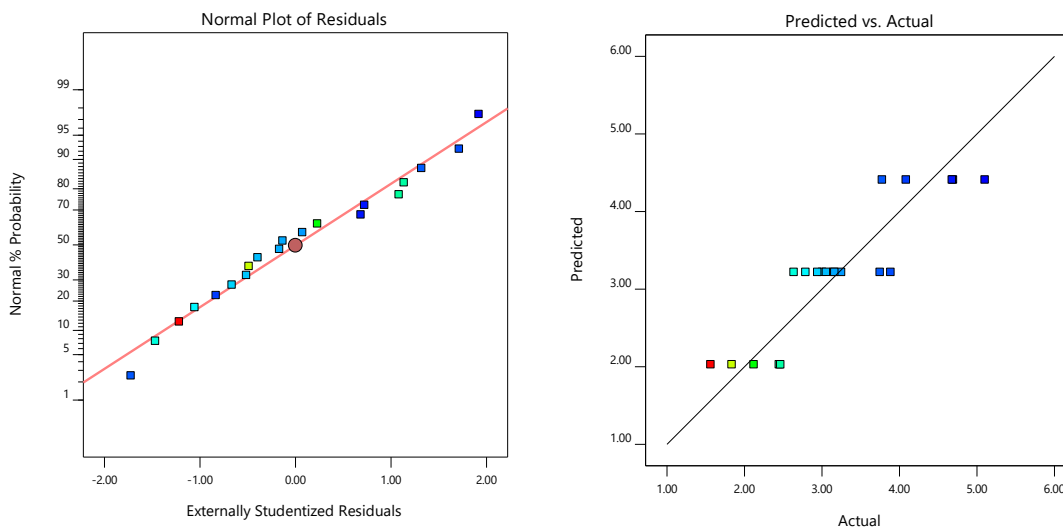
Figure 37: Normal Distribution and Predicted vs Actual Plots for the Silicate Adsorption Model

While there is a greater degree of deviation from ideality in the model's Predicted vs

Actual results than what was observed in the other adsorption models, the residuals of the

individual data points fit the normal distribution line well.
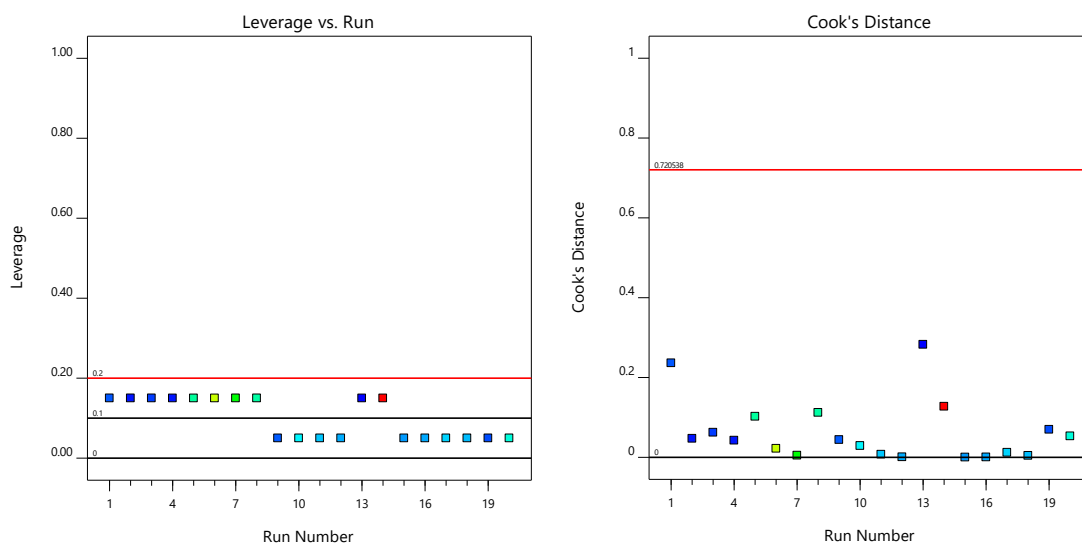
Figure 38: Leverage and Cook's Distance Diagnostic Plots for the Silicate Adsorption Model

Although there was a higher degree of variability between samples, the Leverage and

Cook's Distance plots show that none of the data points induced an excessive amount of

influence on the model nor were any of the points considered to be statistical outliers. Overall,

the data were found to possess a relatively good fit to the selected model and complied well with the various model diagnostics.

A three-dimensional representation of the response surface model for Si-adsorption is presented in Figure 39. The model was produced from the following program-generated expression:

$$\frac{1}{\sqrt{g\,Si/gC}} = 5.006 - 5.953 \times 10^{-5} C_{Si} \tag{33}$$

Where silicon adsorption, gSi/gC, is expressed as a function of silicon concentration (C_{Si}). Temperature in degrees Celsius and Initial Si concentration in mg/L are presented on the x- and y-axes, and Si adsorption is defined in g Si/g C on the z-axis. Reaction time is held constant at 1 h.
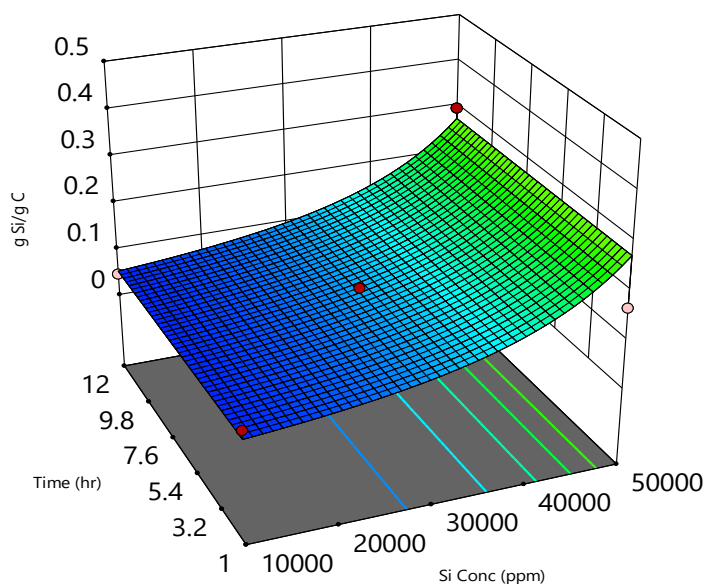
Figure 39: Response Surface Model of Silicate Adsorption Behavior [90]

The model shows the lack of effect of temperature on Si adsorption. Loading levels of 0.27 g Si/g C were achieved at the highest initial solution concentration of 50,000 mg/L Si. Overall, adsorption of the silicate anion was lower than loading levels observed for tungstate and

molybdate adsorption. This behavior is likely due to differences in solution environment due to the silicate adsorption requiring basic conditions in order to keep the silicate in solution.

Optimal conditions for silicate adsorption were determined to be an operating temperature of 20 °C, an initial solution concentration of 50,000 mg/L Si, and a reaction time of 1 h. Multiple batches of Si-loaded precursor were made using these process conditions and produced Si loadings between 0.24 and 0.27 g Si/g C for use in lab-scale carburization experiments. These loading values were determined to be within the lower and upper bound of a 95% confidence interval produced by the presented model as well as being in good agreement with the predicted mean adsorption value.

5.2. Carburization

5.2.1. WC Synthesis and Modeling

The X-ray diffraction pattern for experiment WC10_1 is presented in Figure 40. This diffraction pattern is a representation of the experiments carried out under similar conditions.
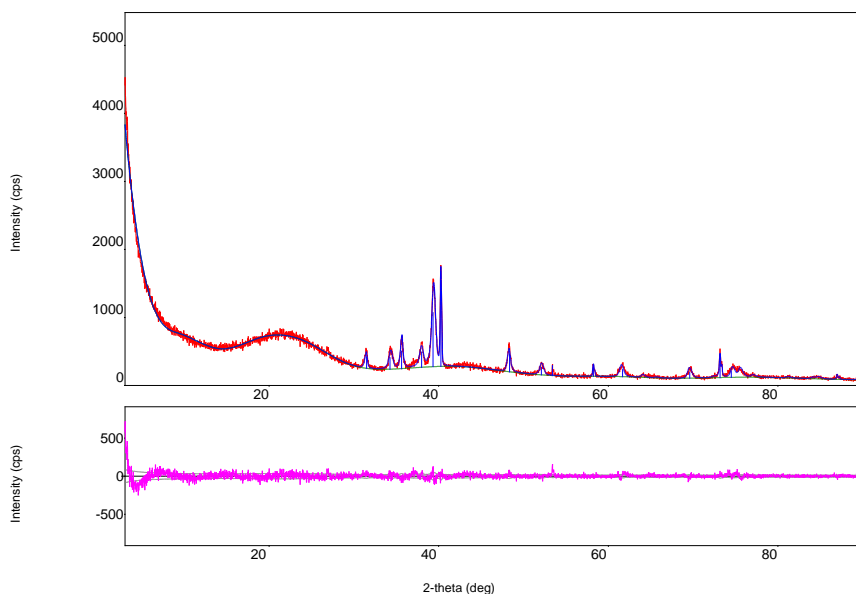
Figure 40: Diffraction Pattern for WC10_1 (1000ºC, Ar, 20h)

The diffraction pattern shows the presence of three crystalline tungsten species: WC, W_2C, and W. In these initial inert atmosphere experiments, the degree of conversion to WC was relatively low with WC making up 14.9% of the composition of the detected crystalline species by WPPF analysis. The bulk of the crystalline species were W_2C (75.7%) with 9.3% remaining as elemental tungsten.

To improve WC yield, inert carburization experiments were also conducted at 1400 °C. A representative X-ray diffraction pattern for these experiments is presented in Figure 41.
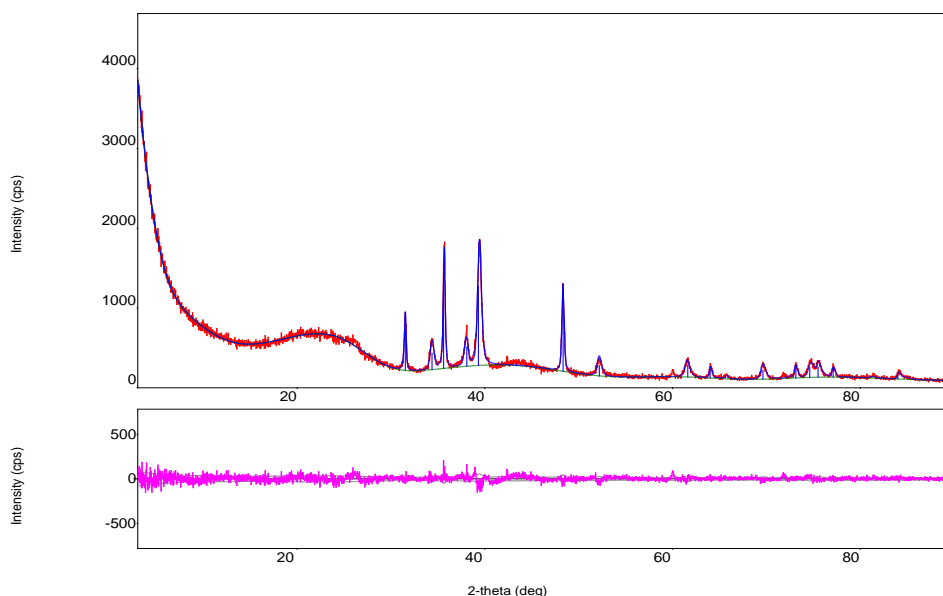
Figure 41: Diffraction Pattern for WC-12DM3 (1400ºC, Ar, 20 hr.)

The XRD analysis detected the presence of two tungsten-based crystalline species: WC and W_2C, and the amounts of each species present differed from the carburization experiments carried out at 1000 °C. The 400-degree increase in temperature significantly increased the amount of WC produced. The WPPF analysis of the sample showed that 44.4% of the crystalline species detected by XRD was WC with the remaining 55.6% being W_2C.

Initial reducing gas experiments were carried out at 865 °C and a gas atmosphere consisting of 15% CH_4, 25% CO, and 60% H_2 by volume. The X-ray diffraction pattern for the 8 h carburization experiment, RGC2, is presented in Figure 42.
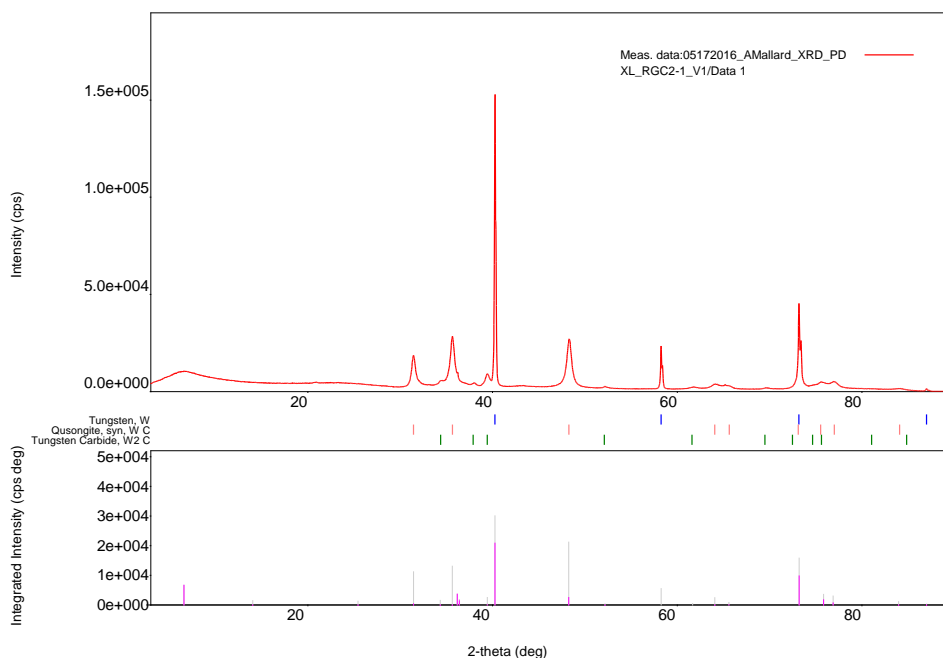
Figure 42: Diffraction Pattern for RGC2 (865 ºC, 15% CH₄, 25% CO, 60% H₂, 8 h)

The diffraction pattern and WPPF analysis show that the composition of the crystalline species present after carburization is composed of 55.0% WC, 4.9% W_2C, and 40.1% W. These early carburization experiments indicated that the reducing gas atmosphere improved conversion to WC when compared to the inert gas carburization experiments as higher degrees of WC conversion were achieved at lower operating temperatures and shorter carburization times. Although there was an increase in the amount of elemental tungsten present in the sample, the amount of W_2C was reduced. The addition of carbonaceous gases likely provided an additional carbon source and allowed for a more rapid rate of carbon diffusion into the metal tungsten lattice. This behavior limited the formation of the metastable W_2C carbide phase.

Because WC conversion rates were still relatively low, carburization experiments were also carried out at temperatures higher than 865 °C. The diffraction pattern presented in Figure 43 corresponds to the product of experiment RGC3 carried out at 950 °C with the same gas atmosphere and total carburization time as RGC2.
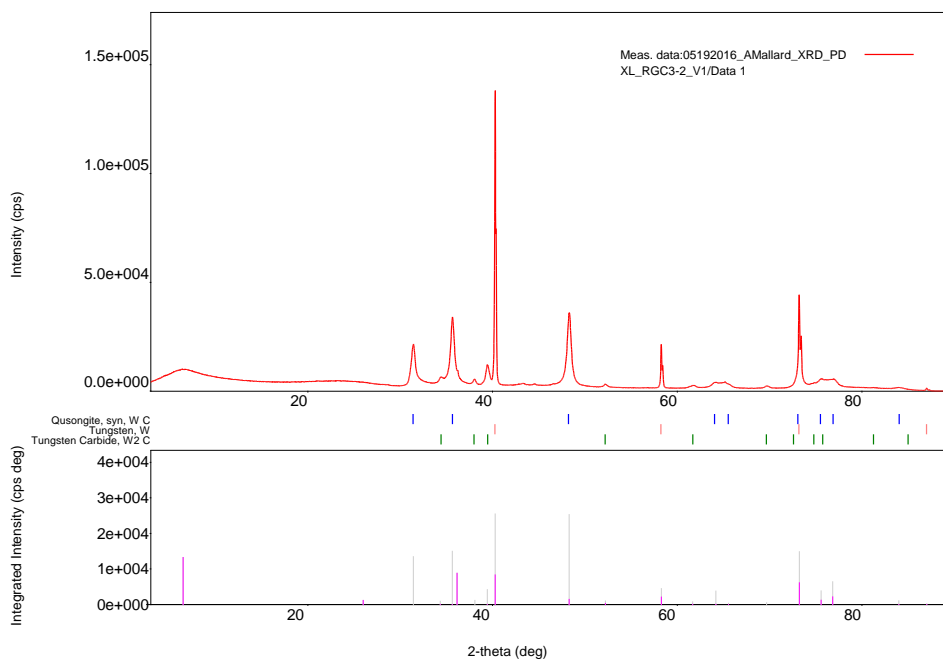
Figure 43: Diffraction Pattern for RGC3 (950 °C, 15%CH4, 25%CO, 60%H2, 6 h)

As expected, the increased carburization temperature improved conversion to WC. The WPPF analysis of the sample showed that the crystalline species were composed of 62.3% WC, 6.2% W_2C, and 31.3% W.

As it was evident that the carburizing gases were improving WC yield, the ratios of the three gases were altered in order to promote conversion to WC. Multiple variations of the three-gas mixture were used, including experiments without the addition of carbon monoxide, but none of the experiments produced a WC yield greater than that observed in RGC3. The diffraction pattern for experiment RGC9, presented in Figure 44, shows an improvement on WC conversion involving a gas atmosphere of 25% CH_4, 35% CO, and 40% H_2.
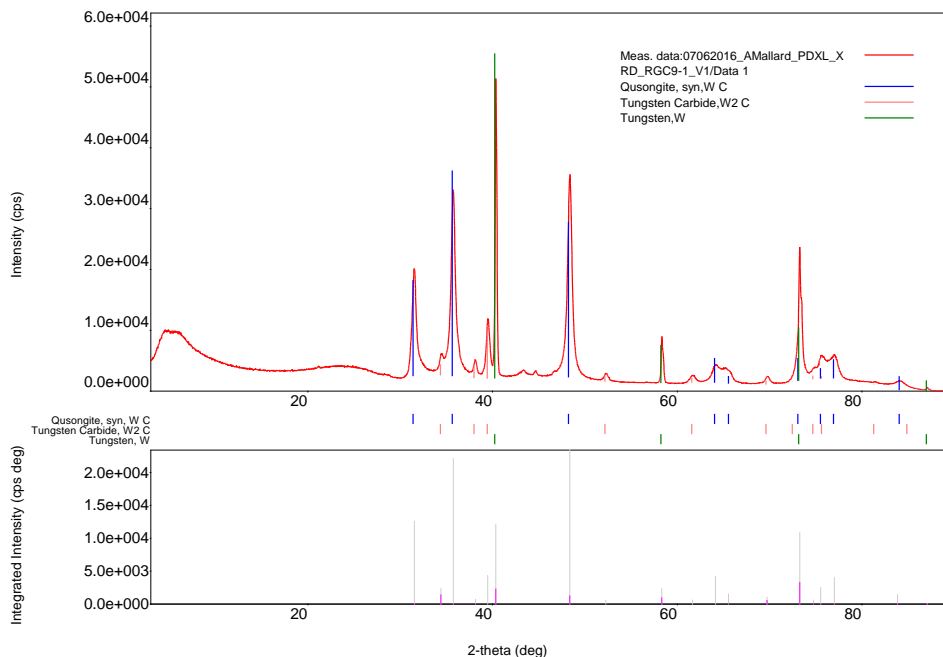
Figure 44: Diffraction Pattern for RGC9 (950 °C, 25% CH_4, 35% CO, 40% H_2, 8 h)

The WPPF analysis of the carburized sample determined the composition of the crystalline species to be 73.6% WC, 8.3% W_2C, and 18.1% W. The results from this experiment indicated that increasing the amount of CH_4 in the gas mixture improves WC conversion. However, subsequent carburization experiments showed the presence of the other gases was still required. Carburization experiments carried out without H_2, for example, resulted in nearly complete mass loss of the carburization product with any remaining solid material coating the inside of the kiln walls in such a way that it could not be recovered from the kiln along with the production of undesirable organic byproducts such as naphthalene.

Further carburization scoping experiments were carried out to improve WC conversion values and mitigate the production of unwanted organic byproducts. A gas mixture consisting of 80% CH_4, 10% CO, and 10% H_2 was selected for use in the carburization experiment, RGC16. The diffraction pattern for the product of this experiment is presented in Figure 45.
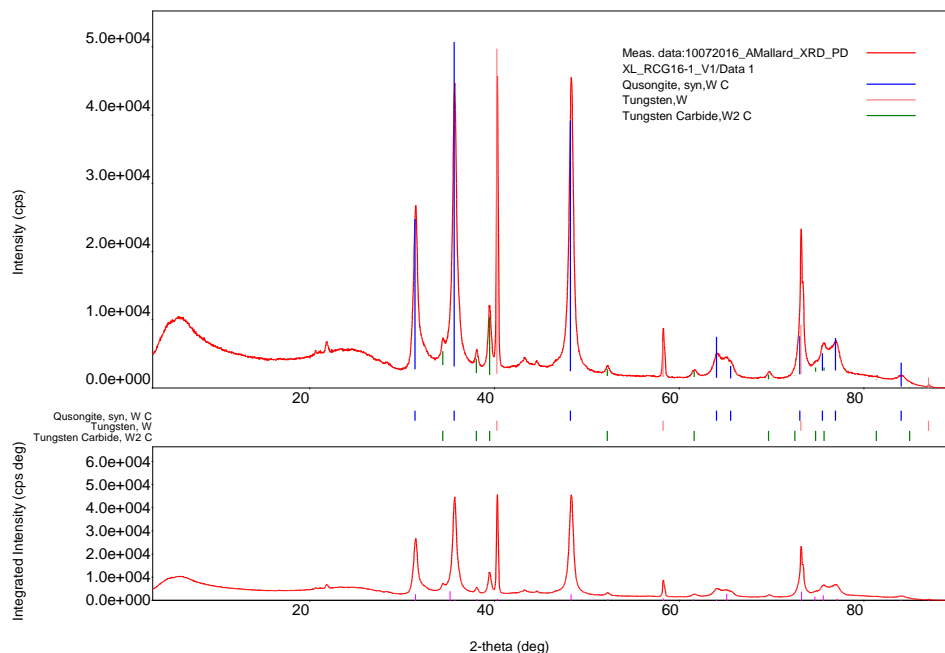
Figure 45: Diffraction Pattern for RGC16 (950 °C, 80% CH$_4$, 10% CO, 10% H$_2$, 8h)

The gas mixture containing 80% CH$_4$ produced an increase in WC conversion. The WPPF analysis determined that WC was 77.2% of the crystalline material identified by XRD with 7.1% being W$_2$C and 15.7% being W. No naphthalene was formed during initial carburization experiments using this gas mixture.

The same gas mixture was used in carburization experiments where additional activated carbon was blended with the W-loaded precursor (1:1 mixture) before being added to the rotary kiln. The diffraction pattern for the first of these experiments, RGC17, is presented in Figure 46.
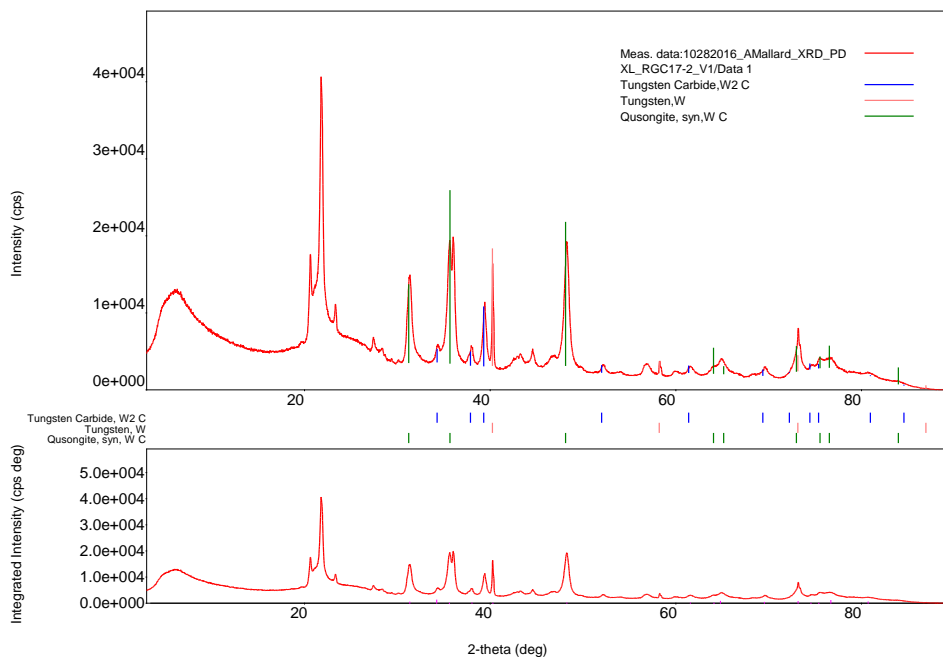
Figure 46: Diffraction Pattern for RGC17 (950 °C, 80% CH4, 10% CO, 10% H2, 8h, Blended Charge)

Blending unloaded activated carbon with the W-loaded precursor significantly improved the conversion of the precursor material to WC. The WPPF analysis of the carburized product detected the same $WC/W_2C/W$ species with the composition being 83.8% WC, 10.0% W_2C, and 6.8% W. Additional peaks present in this diffraction pattern were identified as SiO_2 that originated from the kiln wall.

After the addition of unloaded activated carbon was shown to improve WC conversion, additional scoping experiments were carried out in order to drive WC conversion to completion. Experiment RGC18 was carried out using a furnace charge that was a 1:1 blend of unloaded activated carbon and the carburized product of RGC17. The diffraction pattern of the product of RGC18 is presented in Figure 47.
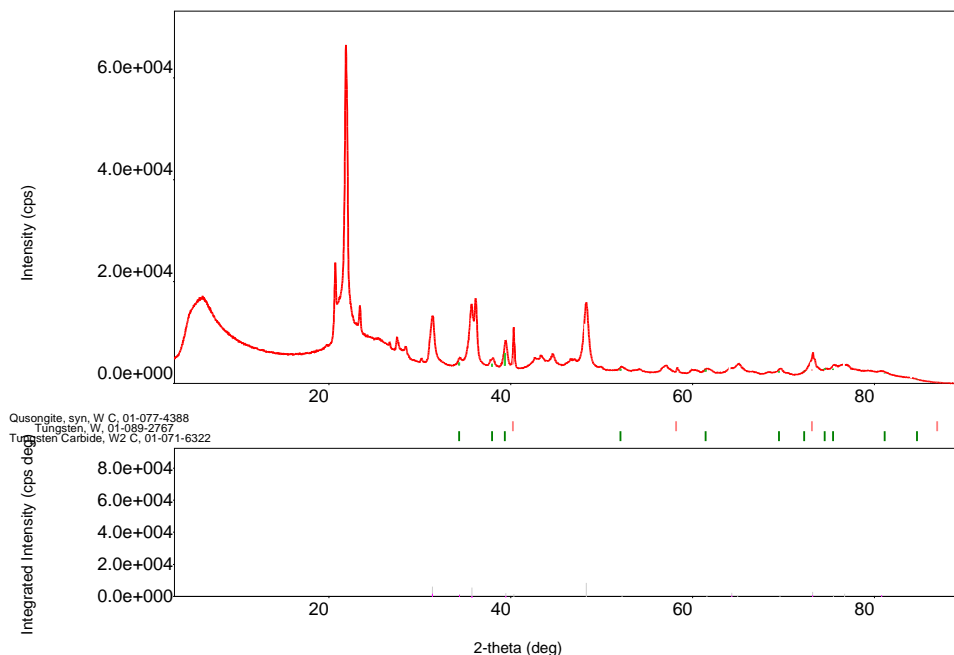
Figure 47: Diffraction Pattern for RGC18 (950 °C, 80% CH₄, 10% CO, 10% H₂, 8h, Blended Charge)

The WPPF analysis of RGC18 determined that the average crystalline phase composition consisted of 88.3% WC, 9.7% W_2C, and 2.8% W. Adding even more unloaded carbon to the furnace charge did improve WC conversion, however, this method of improving WC conversion was determined to be undesirable due to the large additions of added carbon and the small increase in WC conversion they produced. The dilution of the W-loaded precursor with this amount of added carbon made for a low total mass of recoverable tungsten species.

A summary of the evolution of the WC synthesis process through the scoping experiments is provided in Figure 48.
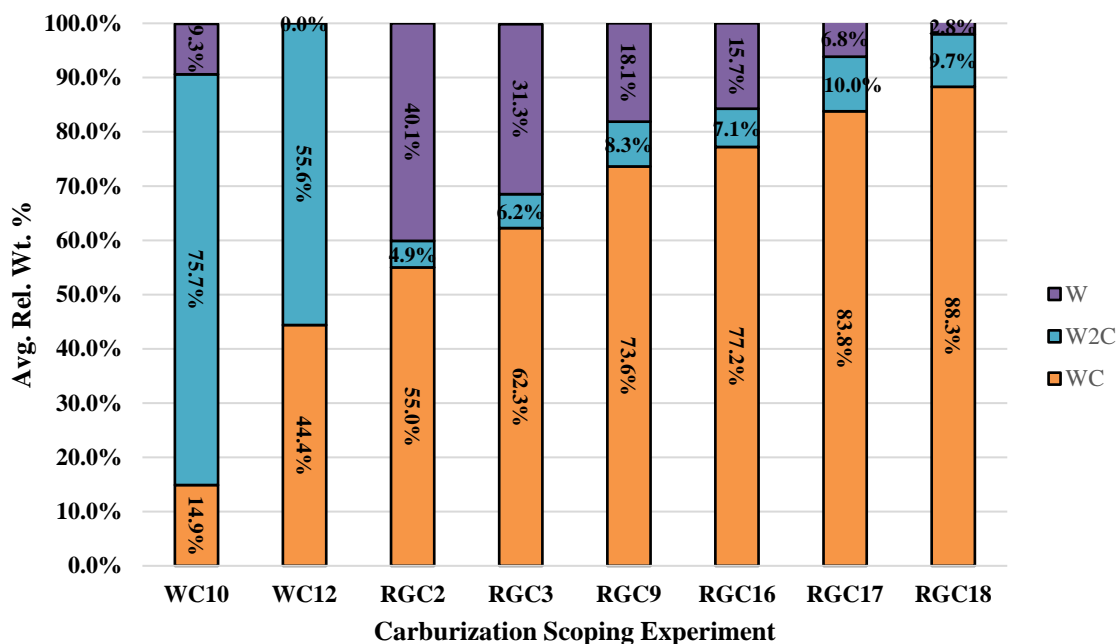
Figure 48: Evolution of WC Conversion Efficiency

The scoping experiments provided a number of insights into the W-loaded precursor carburization process. These experiments showed that gas atmosphere composition was an important factor to consider in this system, as was the blending of unloaded carbon with the W-loaded precursor. As expected, carburization time and temperature also seemed to affect WC conversion. The scoping experiments allowed for the determination of upper and lower boundary conditions for the design of experiments used to mathematically model and statistically optimize the W-carburization process.

A four-variable, two-factorial design of experiments was prepared to model the carburization behavior of the W-loaded precursor. Carburization behavior was modeled using four independent variables: carburization time (h), temperature (°C), added activated carbon (AC) content (% AC), and reducing gas composition as a ratio of methane to hydrogen gas (CH_4:H_2). The observed response was the relative weight percent of WC detected in carburized samples by X-ray diffraction (%WC). A face-centered distribution was also used with the

carburization design of experiments due to experimental complications that occurred during

scoping experiments at temperatures exceeding 950 °C. Three center-point experiments were

added to the design space to account for curvature and to provide lack of fit data. ANOVA data

for the carburization model are presented in Table XII.

Table XII: ANOVA for W-Carburization Model

Source	p-value
Model	0.0004
Time (h)	0.0716
Temp (°C)	0.0115
Added Activated Carbon (% C)	0.0016
Gas Composition (CH_4:H_2)	0.0129
Fit Statistics	
R-squared	0.7923
Adjusted R-squared	0.7125
Predicted R-squared	0.5019
Adequate Precision	11.0538
Lack of Fit	0.0011

All four measured variables were significant to the model as well as an interaction term

between temperature and activated carbon content. Again, there was an issue during the iterative

analysis process with producing an insignificant Lack of Fit value for any of the investigated

models. The presented power series model (Box-Cox recommended) had the largest values for

R-squared, Adjusted R-squared, and Predicted R-squared. The difference between the Adjusted

and Predicted R-squared values is slightly outside of the desired range (0.2196 vs. the desired

0.2), however, the Adequate Precision value is still large enough that the model should be able to

predict values within the design space. It was decided to move forward with this model due to

the quality of the Adequate Precision value and the following diagnostic plots shown in Figure

49 and Figure 50.
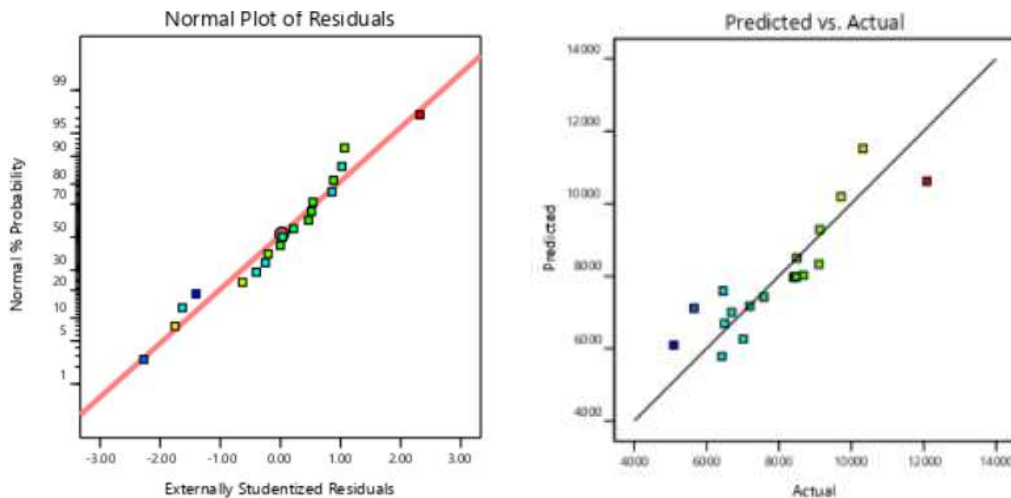
Figure 49: Normal Distribution and Predicted vs Actual Plots for the W-Carburization Model

The normal plot of residuals shows that the data residuals fit the expected normalized

trend well. The Predicted vs. Actual plot is does show some deviation from ideality, it is not

excessive and indicates that the model should be able to predict optimal parameters for

carburization.
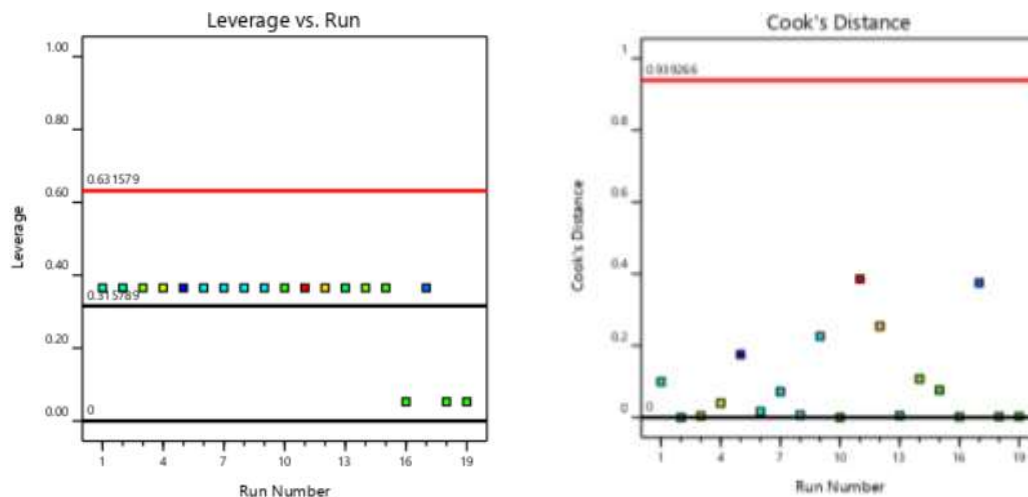
Figure 50: Leverage and Cook's Distance Diagnostic Plots for the W-Carburization Model

The Leverage and Cook's Distance plots also support the use of this model as there appear to be no issues with orthogonality and none of the data points appear to have an excessive effect on the model.

Three variations of the W-carburization model response surface are presented in Figure 51. The model was developed using the following program-generated expression:

$$(Rel\,Wt.\%\,WC)^{2.07} = \text{-}41362.26 + 452.79t + 52.45T + 938.29AC + 221.44C_{gas} - 1.11TAC \quad (34)$$

where t represents carburization time in h, T represents temperature in °C, AC represents the added activated carbon as a weight percent, and C_{gas} represents the gas composition as a ratio of CH_4 to H_2. For all three response surfaces, gas composition is held constant at a CH_4:H_2 ratio of 8:1 while time is held constant at 6 h for Figure 51 (a), 7 h for Figure 51 (b), and 8 h for Figure 51 (c). The amount of WC produced is presented on the z-axis as an average relative weight percentage.
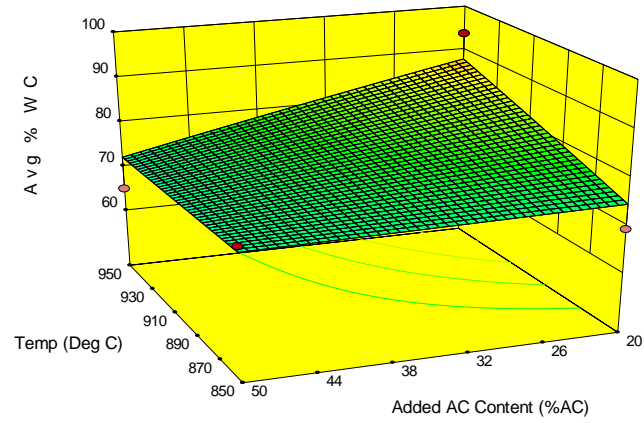
(a)
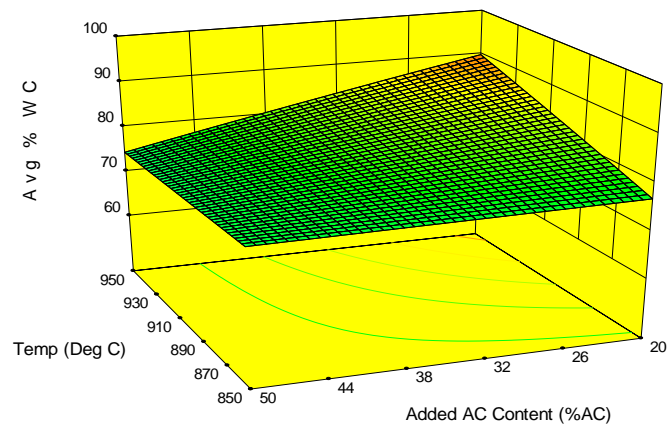
(b)
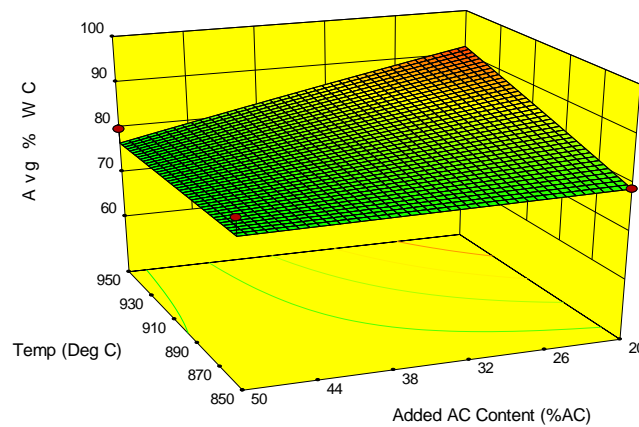
(c)

Figure 51: W-Carburization Response Surfaces at 6 h (a), 7 h (b), and 8 h (c) [91]

As expected, WC production increased with increasing time and temperature. Increased CH_4 content was also found to produce the highest amounts of WC. However, it was observed that, although mixing unloaded carbon with the W-loaded precursor improved WC conversion, the highest amounts of WC were produced in samples that contained the lowest amounts of added carbon even at higher temperatures.

The effect of added carbon on WC conversion can be observed in greater detail in the Interaction Plot of added carbon content and temperature produced by the model that is presented in Figure 52. Temperature is defined on the x-axis in degrees Celsius, while WC conversion is expressed on the y-axis as an average relative weight percent. In this Interaction Plot, carburization time is held constant at 8 h and gas composition is set at a ratio of 8:1 ($CH_4:H_2$).
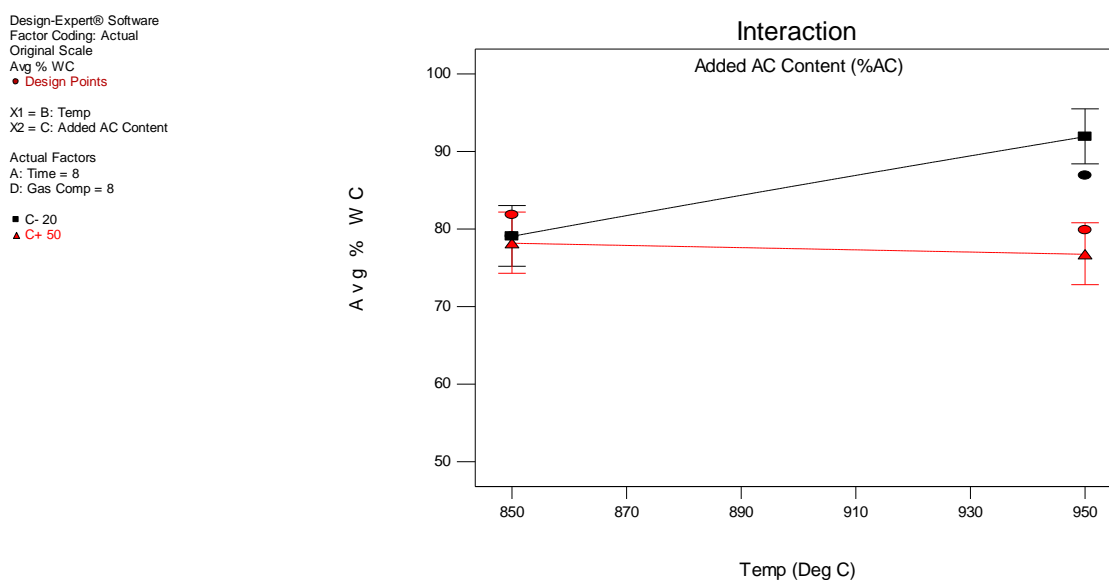
Figure 52: Temperature-Added Carbon Variable Interaction Plot

The Interaction Plot shows that increasing the added carbon content changes the statistical effect of temperature on WC production with WC production essentially remaining constant across the temperature design space when added carbon levels reach 50% of the sample by mass. This behavior may indicate that added carbon levels greater than 20% inhibit

conversion to WC by shielding the adsorbed tungsten from the gaseous carbon sources. This shielding effect would limit the gas-solid reactions that would be able to take place by reducing the interface between the solid tungsten and the carbon-containing methane. The production of WC would then primarily depend on solid W- solid C reactions that would occur much more slowly than the gas-solid reactions.

Further evidence for the existence of this shielding effect can be observed in the One Factor plots presented in Figure 53. Carburization time is defined on the x-axes of both plots in hours while temperature is set at 950 °C and the gas composition is held constant at a ratio of 8:1 (CH_4: H_2). Figure 53 (a) shows the behavior of a 20% addition of carbon while Figure 53 (b) shows the behavior of a 50% addition of carbon.

(a) **(b)**
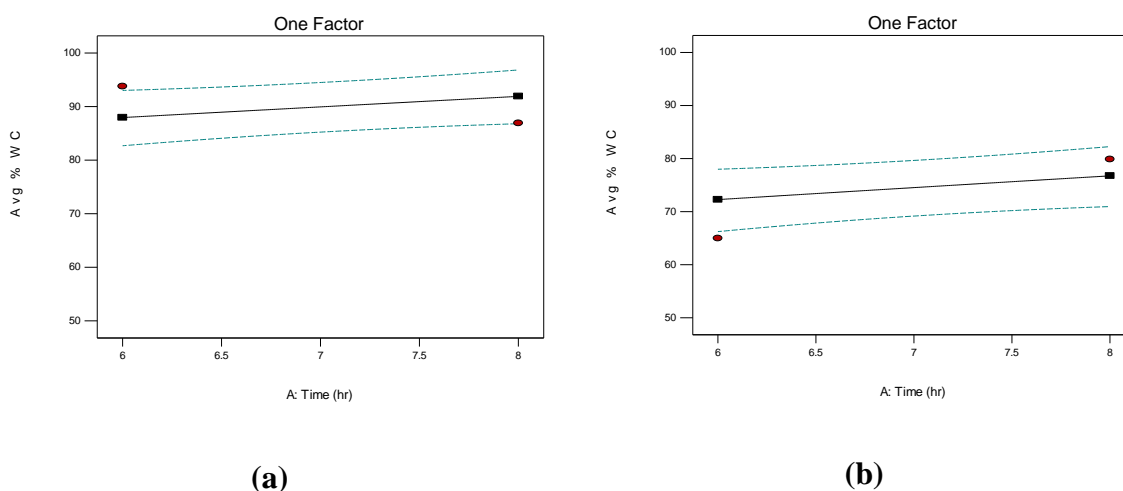
Figure 53: Effect of Carbon Content on Carburization at 950 °C with Respect to Carburization Time at 20% AC (a) and 50% AC (b)

Increasing the added carbon content of the furnace charge results in a 15-20% decrease in overall WC conversion at all carburization time intervals. This behavior could be explained as the inhibition of the gas-solid reactions that would normally promote WC conversion to the more desirable levels on conversion observed at lower amounts of added carbon.

A series of four confirmatory experiments was carried out to validate the predictive capabilities of the W-carburization model. The experimental parameters for these confirmation experiments are presented in Table XIII.

Table XIII: Experimental Parameters for the W-Carburization Model Confirmatory Experiments

Experiment	Time (h)	Temp (^{o}C)	Added Carbon (%)	Gas Comp. ($CH_4:H_2$)
WC-Conf-1	8	950	20	8
WC-Conf-2	8	900	20	8
WC-Conf-3	8	925	20	8
WC-Conf-3REP	8	925	20	8

Although the model has indicated that optimal carburization conditions include operating at 950°C, due to issues with producing naphthalene at that temperature, a number of the confirmation experiments were carried out at temperatures below 950°C in order to avoid naphthalene production and produce results that would be able to validate the predictive capabilities of the model.

Three samples of each carburization product were analyzed via XRD to determine composition and the compositions of each replicate were determined by WPPF analysis. These data are presented in Table XIV as an average relative weight percent of the three replicate samples for each carburization product.

Table XIV: Confirmatory Experiment Results for the W-Carburization Model

WC-Conf-1 (950°C)		
Sample Composition	**Avg. Rel. Wt. %**	**Notes**
WC	69.3	Large amount of naphthalene produced during run
W	20.2	
W_2C	10.5	
WC-Conf-2 (900°C)		
WC	74.2	No naphthalene detected
W	18.2	
W_2C	7.6	
WC-Conf-3 (925°C)		
WC	79.2	Small amount of naphthalene produced
W	16.9	
W_2C	4.0	
WC-Conf-3REP (925°C)		
WC	80.2	Small amount of naphthalene produced
W	13.7	
W_2C	6.1	

The amount of WC detected in WC-Conf-1 is significantly lower than expected due to the amount of naphthalene produced during the experiment. However, the lower amount of naphthalene produced at lower temperature runs allowed for their use in validating the carburization model. The two experiments carried out at 925°C (WC-Conf-3 and WC-Conf-3REP) produced WC in amounts that fell within a 95% confidence interval produced by the carburization model. Although the detected mean value is lower than the predicted mean (88.6%WC), the difference is likely due to the naphthalene reactions limiting the amount of available carbon for the carburization reaction. This phenomenon was accounted for, however, within the carburization model and the model is capable of predicting carburization behavior within the design space. The average WC content of WC-Conf-2 was slightly outside of the 95% confidence interval for those experimental conditions.

In addition to the statistical modeling, the carburized products were also analyzed using SEM. Representative images of the precursor samples carburized under the reducing gas mixture are presented Figure 54. Both images are a combination of both secondary electron, and backscattered electron imaging allowing for both topographical and compositional analysis.
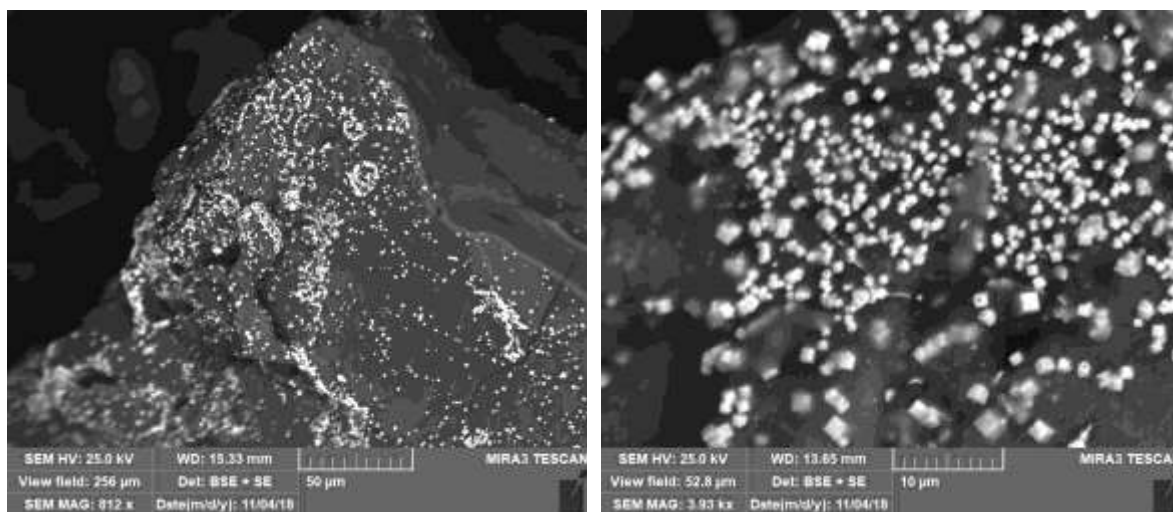
(a)   (b)

Figure 54: Micrographs of Carburized W-Loaded Precursor at Lower (a) and Higher (b) Magnifications

The micrographs of the carburized precursor show that the process is capable of converting the adsorbed anions into solid particles on the surface of the activated carbon matrix. EDAX analysis confirmed that the smaller white crystals are tungsten compounds attached to the surface of the larger activated carbon particles which supports the analyses of the carburized products by XRD. Mixed $WC/W_2C/W$ Crystals produced during the carburization process were of a relatively uniform particle size of approximately 2 microns.

5.2.2. Mo$_2$C Synthesis and Modeling

A representative diffraction pattern for the products of Mo-carburization experiments carried out under argon at 1100 °C is presented in Figure 55.
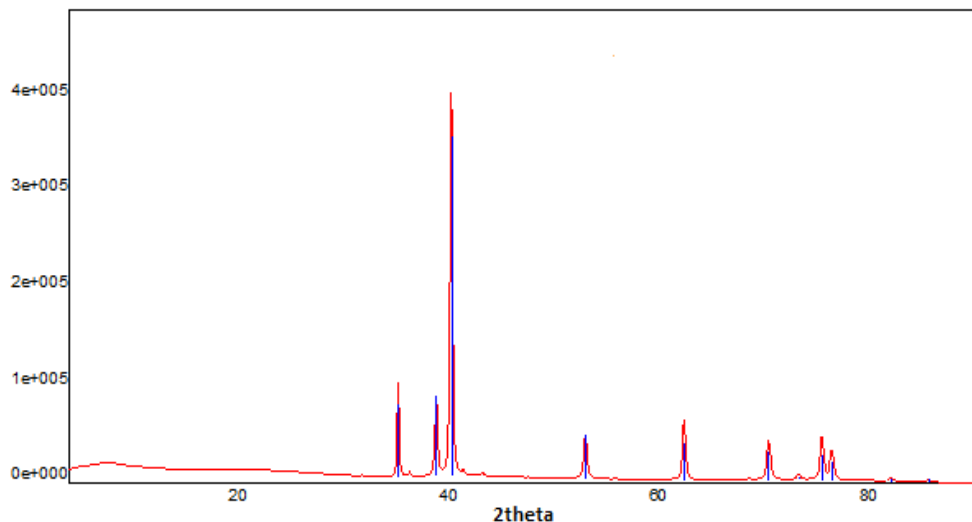
Figure 55: Diffraction Pattern of Mo-Loaded Precursor Carburized at 1100 °C under Ar Atmosphere

During carburization in argon at 1100 °C, the only species detected by XRD was molybdenum carbide (Mo_2C). The success of these early inert gas carburization experiments suggested that Mo_2C could be synthesized at lower temperatures and with less complicated reducing gas atmospheres than those required for synthesizing WC.

A representative diffraction pattern for the Mo-loaded precursor carburized at 600 °C under an H_2 atmosphere is presented in Figure 56.
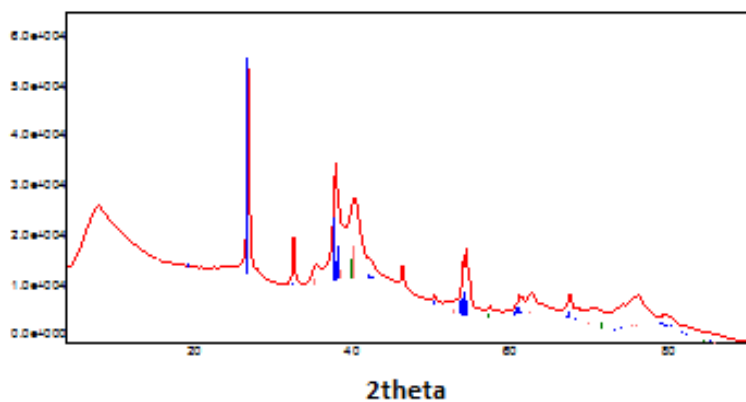
Figure 56: Diffraction Pattern of Mo-Loaded Precursor Carburized at 600 °C under H_2 Atmosphere

The compositions of the carburization products from the experiments carried out under H_2 were found to have a crystalline species composition of 40% Mo_2C, 35.9% MoO_2, and 24%

Mo by WPPF analysis. The presence of MoO_2 in the carburized sample is likely due to MoC oxidizing in air after the carburized furnace charge was removed from the kiln. The results from the H_2 carburization experiments indicated the following: 600 °C is not a high enough temperature for Mo_2C synthesis, that carbon-containing gases need to be included in the gas mixture, or that both higher temperatures and carbon-containing gases are required to completely convert the available Mo to Mo_2C.

Further carburization experiments were carried out using the same reducing gas mixture that was found to work best for producing WC in an effort to develop a flexible process that could effectively synthesize both WC and Mo_2C. The diffraction patterns presented in Figure 57 are from the products of three carburization experiments carried out using a reducing gas mixture consisting of 80% CH_4, 10% CO, and 10% H_2.
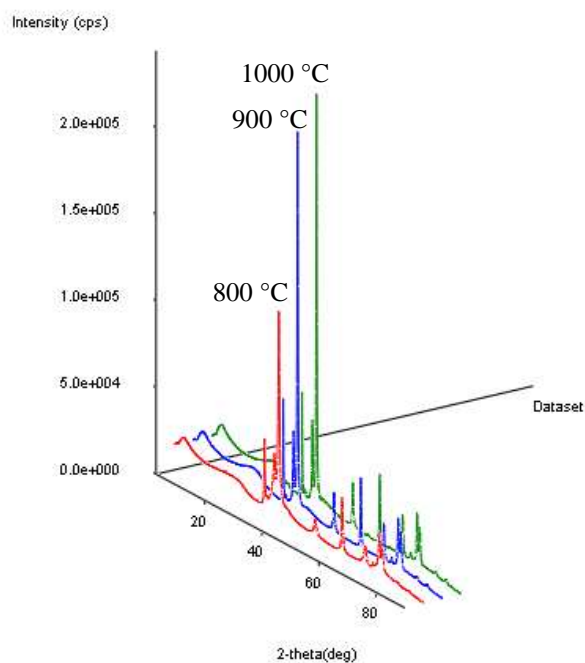
Figure 57: Effect of Temperature on Mo₂C Conversion under a Reducing Gas Mixture at 800, 900, and 1000 °C

The XRD results show that Mo$_2$C is the only crystalline phase present in the carburized samples at all three temperatures. Replicate experiments of MoRGC-7 (800 °C) were carried out in order to determine if the results were reproducible. The diffraction patterns presented in Figure 58 demonstrate that carburization of the Mo-loaded precursor at 800°C is a reproducible phenomenon.
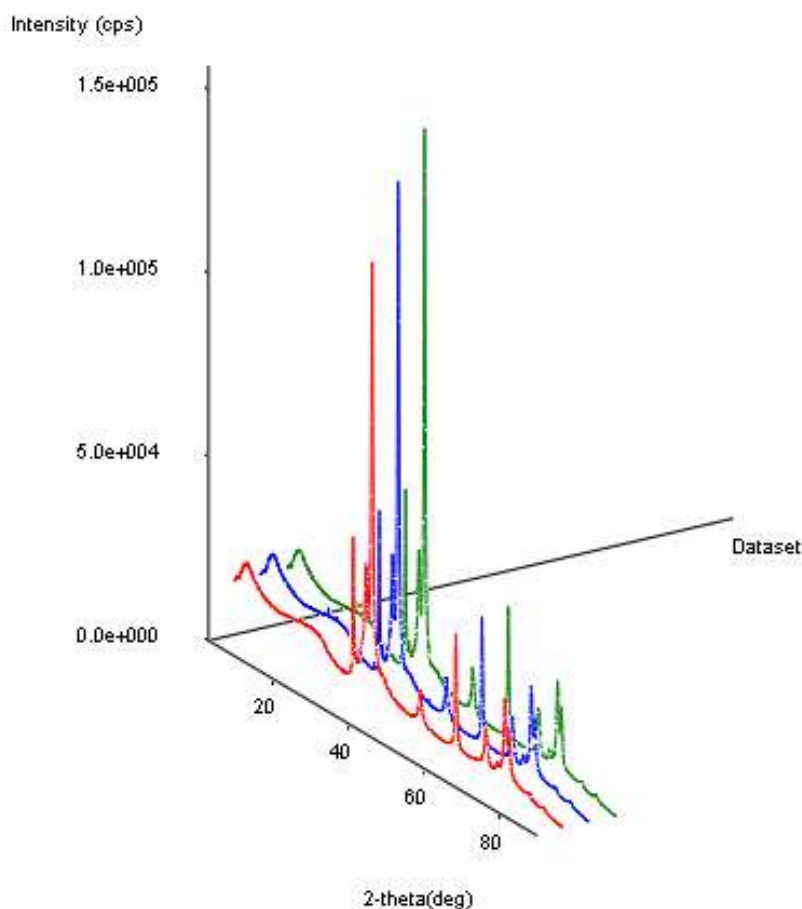
Figure 58: Replicate Experiments of MoRGC-7 (800 °C)

The carburization temperature range between 700 and 800 °C was investigated in greater detail in order to determine the "breakaway" temperature at which Mo$_2$C appeared as the sole crystalline phase. Additional experiments were carried out at 700 °C, 725°C, 750°C, and 775°C

under the specified reducing gas composition. The XRD patterns for samples carburized within the 700-800ºC temperature range are presented in Figure 59.
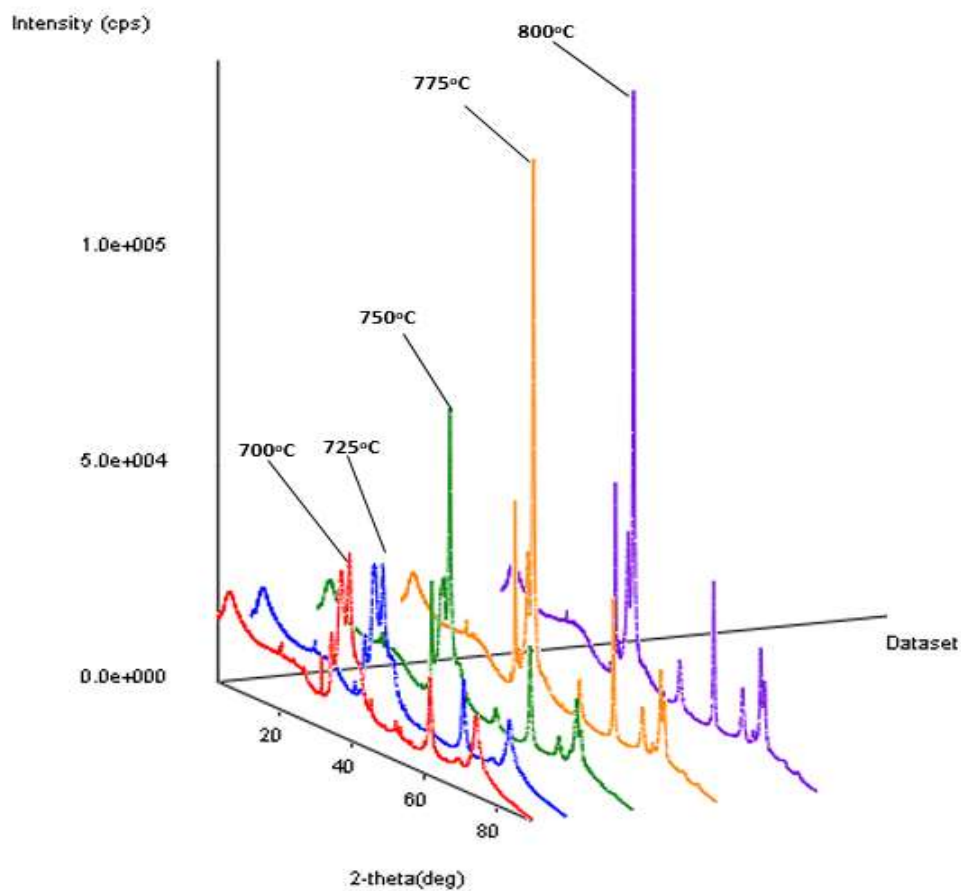
Figure 59: Mo-Carburization Profile (700-800 °C)

During carburization under argon at 1100 °C, the only species detected was Mo_2C. Likewise, the XRD patterns for samples carburized under reducing conditions at 800 °C and 775 °C are nearly identical to the inert gas sample carburized at 1100 °C with Mo_2C being the only phase present within the samples. The presence of Mo_2C was detected at 750 °C, alongside other molybdenum species including MoC, and elemental molybdenum. The amount of Mo_2C present in samples carburized at temperatures below 750 °C continued to decrease in relative concentration as the temperature decreased.

The carburization scoping experiments were used to develop upper and lower boundary conditions for the design of experiments that would involve scaled-up carburization experiments similar to those used for the W-carburization behavior model. The ANOVA data for the Mo-carburization model is presented in Table XV.

Table XV: ANOVA Data for Mo-Carburization Model

Source	p-value
Model	< 0.0001
Temp (°C)	< 0.0001
Fit Statistics	
R-squared	0.9737
Adjusted R-squared	0.9708
Predicted R-squared	0.9665
Adequate Precision	30.2791

The selected model for Mo-carburization was determined by ANOVA to be statistically significant. The high R-squared value is also in good agreement with the Adjusted and Predicted R-squared values indicating that the model fits the data well. The Adequate Precision value produced by the model indicates that the selected model has sufficient predictive power to predict carburization behavior within the design space.

Diagnostic plots for the Mo-carburization model are presented in Figure 60 and Figure 61. A Normal Distribution plot and a Predicted vs Actual plot are presented in Figure 60.
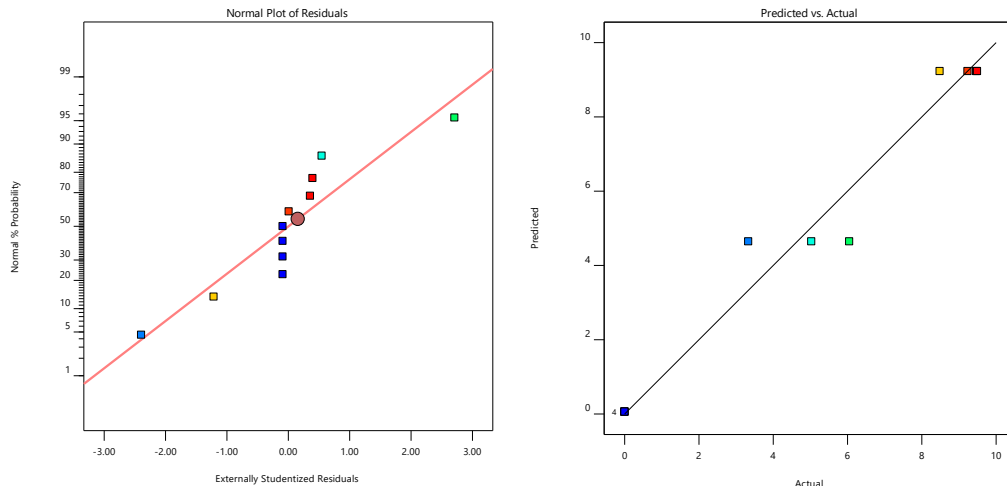
Figure 60: Normal Distribution and Prediction vs Actual Plots for the Mo-Carburization Model

Although some deviation from ideal trends is present in both plots, the data residuals are relatively normally distributed, and the data points follow the predicted trend well with some increased variation in the mid-range samples.

Plots of the Leverage and Cook's Distance values associated with each data point are presented in Figure 61.
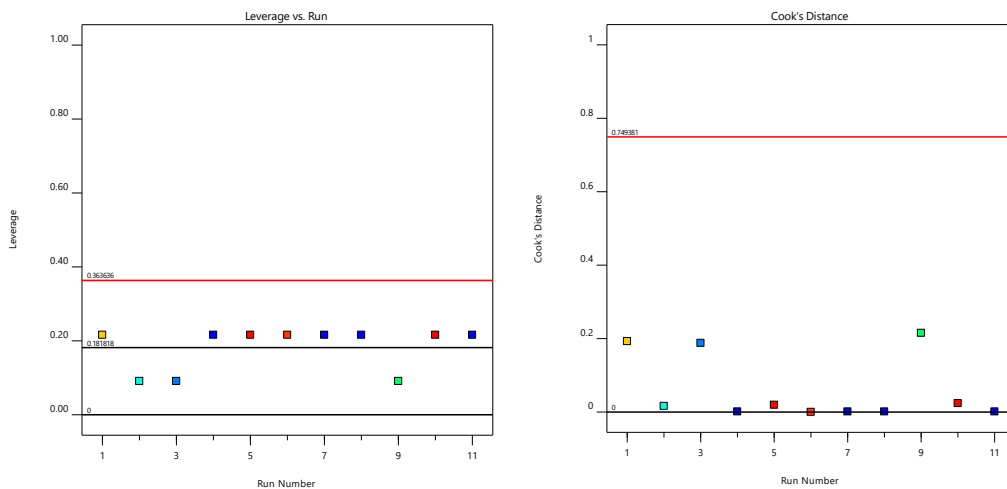
Figure 61: Leverage and Cook's Distance Diagnostic Plots for the Mo-Carburization Model

The Leverage plot shows that none of the data points used to build the statistical model have a significantly greater degree of influence over the model than any other data point indicating a lack of orthogonality issues within the model. The Cook's Distance plot also shows

that none of the data points used to build the carburization model should be considered as outliers and validates using the data to build a predictive model.

A three-dimensional representation of the Mo-carburization model is presented in Figure 62. The model was developed using the following program-generated expression:

$$\sqrt{\text{Rel. Wt. \% Mo}_2\text{C}} = -12.92 + 0.03\text{T}. \tag{35}$$

Temperature is defined in degrees Celsius on the x-axis and gas composition is defined on the y-axis as the molar ratio of CH_4 to H_2 ($CH_4:H_2$). The degree of conversion to Mo_2C is defined on the z-axis as average relative weight percent determined by XRD (WPPF). Carburization time is held constant at 1 h.
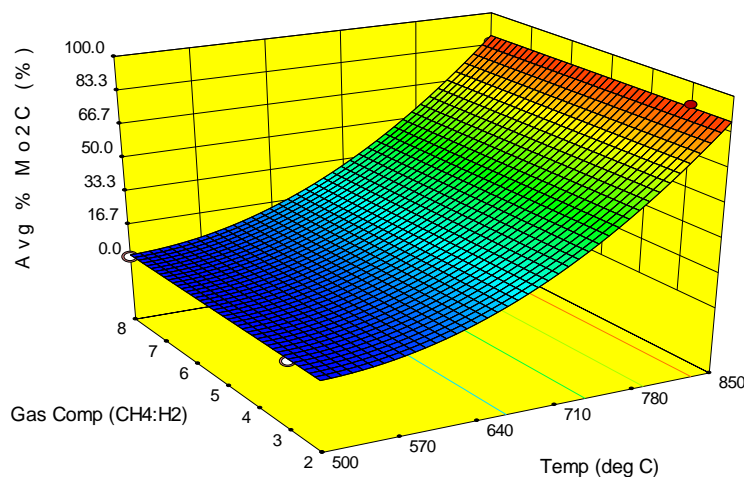
Figure 62: Mo-Carburization Response Surface Model [93]

The selected model shows some significant differences between Mo-carburization and W-carburization behavior. While conversion to WC was dependent on a number of variables including temperature, gas composition, and carburization time, conversion to Mo_2C is primarily a thermally driven process with temperature being the only statistically significant variable within the design space. Conversion to Mo_2C of approximately 90% was achieved at 850 °C

regardless of carburization time or gas composition. High degrees of conversion to Mo_2C occur at temperatures significantly lower than what is required for synthesizing WC. This behavior is likely due to the formation of Mo_2C having a lower activation energy than WC [62], [94].

Three confirmatory experiments were carried out to determine the predictive capabilities of the Mo-carburization model. All three of the confirmatory experiments used a carburization temperature of 850 °C, a reaction time of 2 h, and a gas atmosphere consisting of a CH_4: H_2 ratio of 2.9. The compositions of the three carburization products are presented in Table XVI.

Table XVI: Confirmatory Experiment Results for the Mo-Carburization Model

Experiment	Mo_2C (Avg. Rel. Wt. %)	MoC (Avg. Rel. Wt. %)
Mo_Conf1	94.2	5.8
Mo_Conf2	96.2	4.0
Mo_Conf3	95.4	4.5

The optimal conditions for carburization predicted by the Mo-carburization model produced high conversions to Mo_2C on the Mo-loaded precursor. The compositions of the carburization products from the three confirmatory experiments indicate that the process is reproducible and the amounts of Mo_2C observed in the carburization products fall within the bounds of a 95% confidence interval predicted by the model.

The products of the Mo-carburization model experiments were also analyzed using SEM to investigate the morphologies of the synthesized carbide species. A representative micrograph of samples carburized at 850 °C is presented, along with the corresponding X-ray diffraction pattern, in Figure 63.
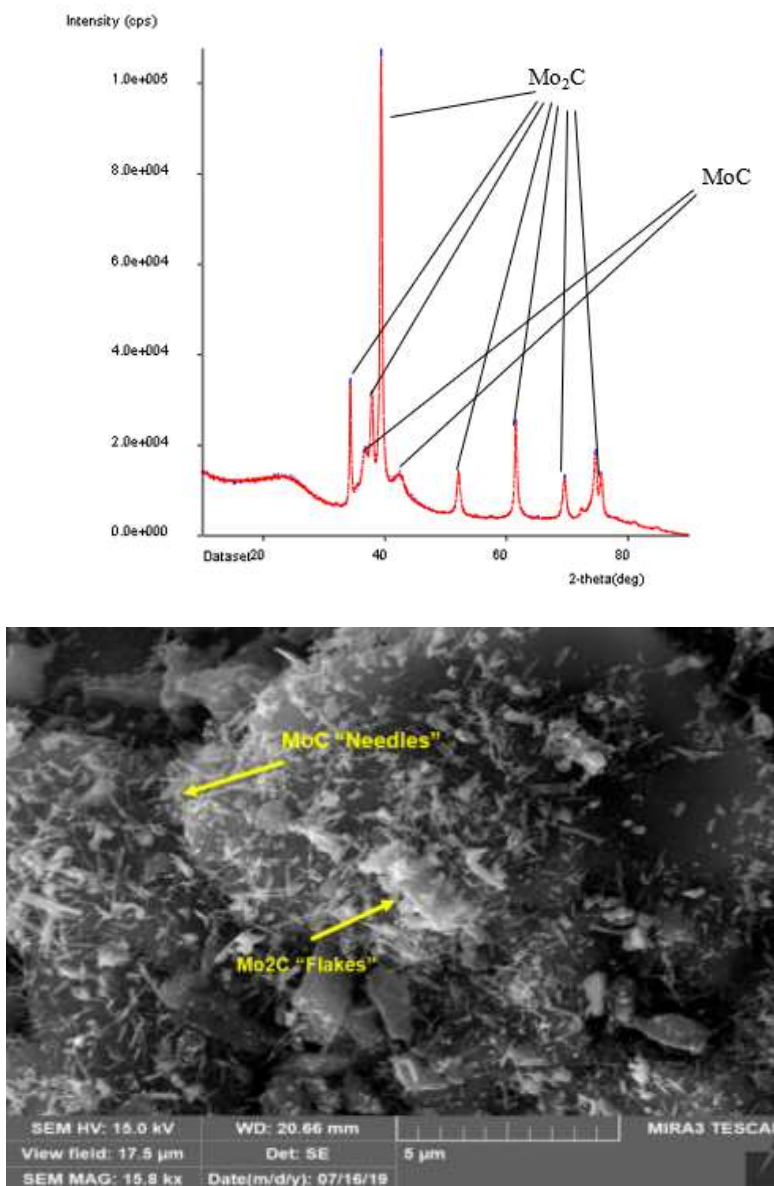
Figure 63: Diffraction Pattern and Surface Micrograph of the Mo-Loaded Precursor Carburized at 850 °C

The X-ray diffraction pattern indicated the presence of two distinct crystalline phases: Mo_2C and MoC with Mo_2C being the dominant phase present with approximately 90% the crystalline species existing as Mo_2C. Micrographs of the samples carburized at 850 °C show two different morphologies ("needles" and "flakes") present in the crystals found on the surface of the activated carbon matrix. The lighter colored crystals on the surface of the darker carbon matrix were analyzed via EDAX and were found to contain Mo. The mixed Mo_2C/MoC crystals

are approximately 2-3 microns or smaller with "needle" structures approaching submicron dimensions in thickness.

Samples carburized at 500 °C were also analyzed via SEM. A representative micrograph of samples carburized at 500 °C is presented, along with the corresponding X-ray diffraction pattern, in Figure 64.
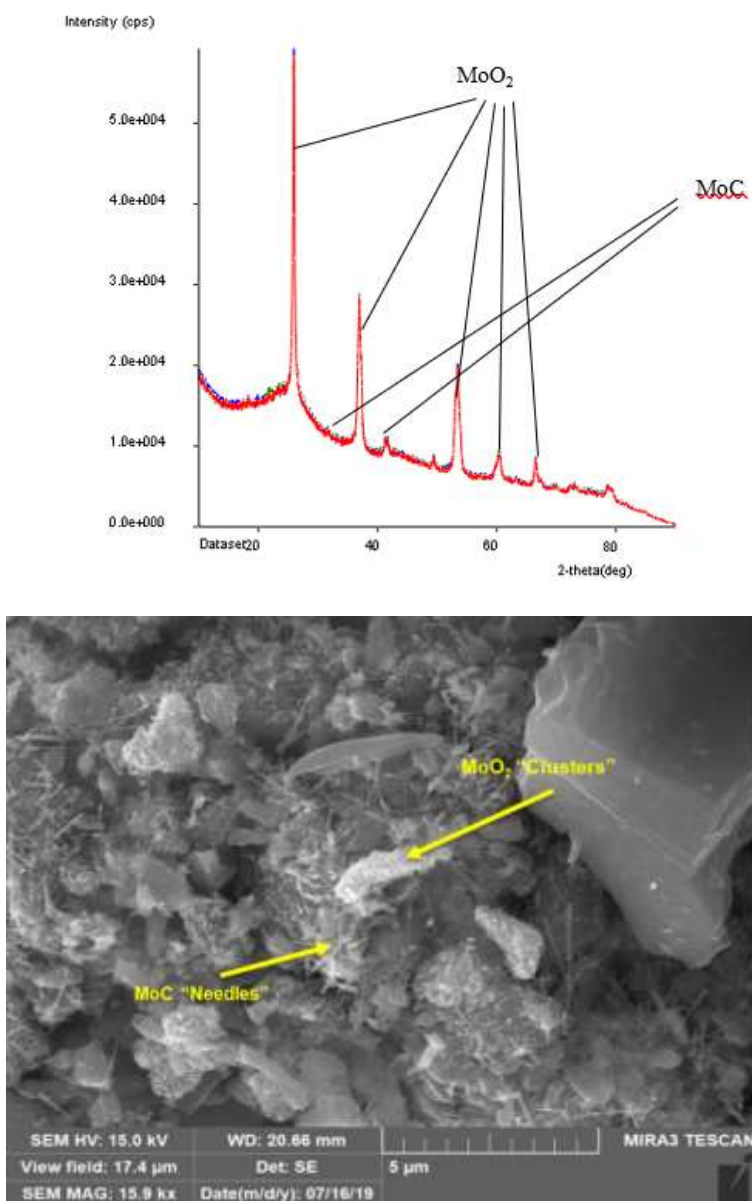
Figure 64: Diffraction Pattern and Surface Micrograph of the Mo-Loaded Precursor Carburized at 500ºC

X-ray diffraction patterns for samples carburized at 500 °C show the presence of two distinct crystalline phases: MoO_2 and MoC. The SEM images also show two different crystalline structures formed on the surface of the carbon matrix. Again, small "needles" are present in the carburized sample along with a new "cluster" morphology that was not observed in samples carburized at 850 °C. The crystalline materials were identified as being Mo species via EDAX, adding further support to the XRD data. The crystalline species were found to be approximately 2-3 microns in size or smaller with the needle-like structures being submicron in thickness as observed in the samples carburized at 850 °C. Smaller particle sizes were likely produced due to the lower operating temperatures and shorter reaction times required to carburize the Mo-loaded precursor.

Based on the presence of the needle structures in samples carburized at 500 °C and 850 °C, and a literature investigation, these structures were identified as MoC. With the "needles" identified as MoC, the "flakes" observed in the 850 °C samples were identified as Mo_2C and the "clusters" were determined to be the MoO_2 detected in the samples at 500 °C by XRD. Existing literature supported this determination as Mo_2C has been shown to form "flakes" in other synthesis methods [31]. MoO_2 has also been shown to form "clusters" of crystals as it undergoes oxidation [33]. It is likely that the MoO_2 clusters formed pre-carburization as the adsorbed molybdate species were reduced at elevated temperatures. As these oxide clusters only appear at low temperatures, they are likely a result of incomplete carburization of the Mo-loaded precursor.

5.2.3. SiC Synthesis

Initial Si-loaded precursor carburization experiments were carried out at 1400 °C under

an argon atmosphere. A representative diffraction pattern for these initial Si-carburization

experiments is presented in Figure 65.
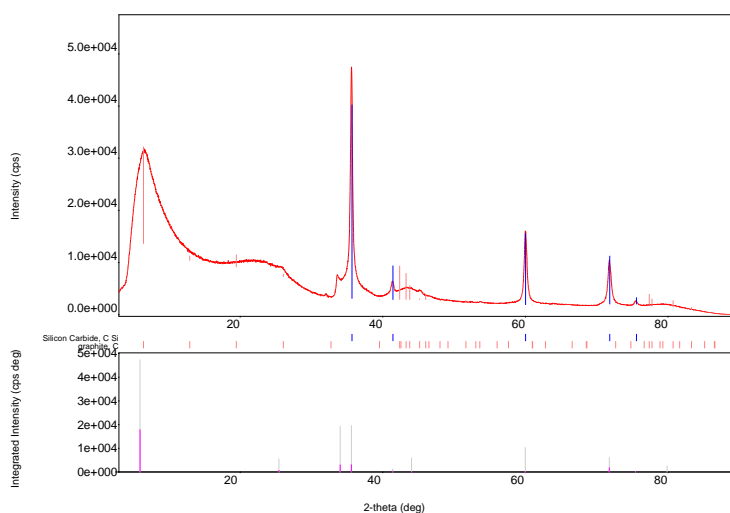
Figure 65: XRD Pattern for Si-Carburization at 1400 °C under Argon Atmosphere

β-SiC was detected as the sole crystalline species in samples carburized at 1400 °C under

an Ar atmosphere. This carburization behavior is predicted by the Si-C binary phase diagram.

The carburized Si-loaded precursor was also characterized using SEM. A micrograph of

the material carburized at 1400 °C under Ar is presented in Figure 66.
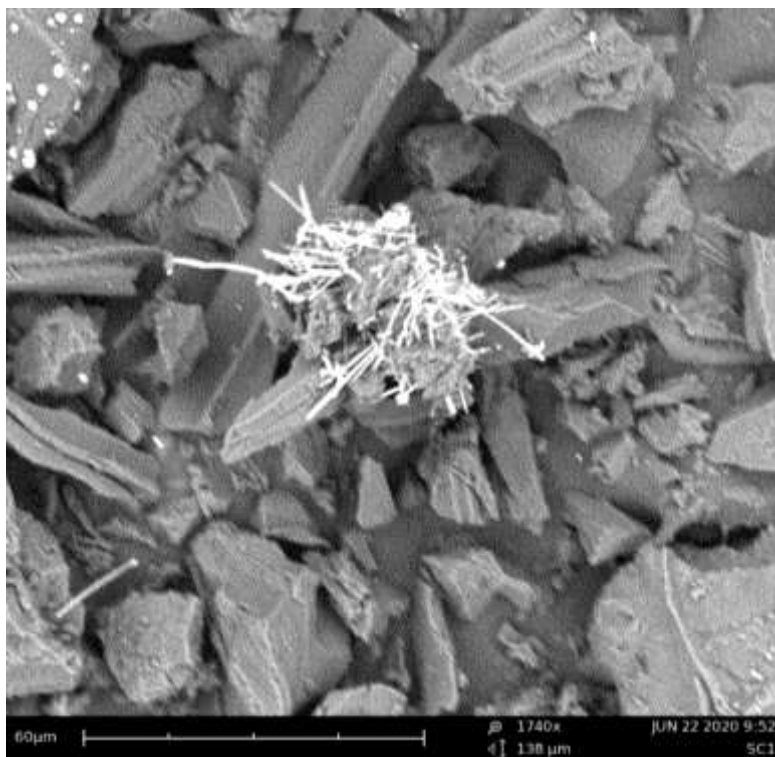
Figure 66: SEM Image of Carburized Si-Loaded Precursor (1400 °C, Ar, 20 h)

The micrograph of the carburized Si-loaded precursor shows that the silicate anions were reduced to form "whiskers" of SiC on the surface of the activated carbon matrix. While some of the SiC appears to have formed as "nodules" (top left of image), the majority of the SiC is present as long, thin crystals approaching submicron sizes in thickness. The morphology of the SiC produced on the surface of the Si-loaded precursor may have formed because of the mechanism by which SiC is believed to be formed, i.e. through an intermediate gas phase. Due to the constant flow of Ar through the alumina tube, the $SiO_{(g)}$ would have allowed for the adsorbed Si to be transported and deposited in a manner that would form the long SiC "whiskers".

Carburization experiments conducted in an H_2 atmosphere also successfully carburized the Si-loaded precursor at temperatures as low as 1200 °C. An example of the X-ray diffraction pattern for the carburized precursor at 1200 °C under H_2 is presented in Figure 67.
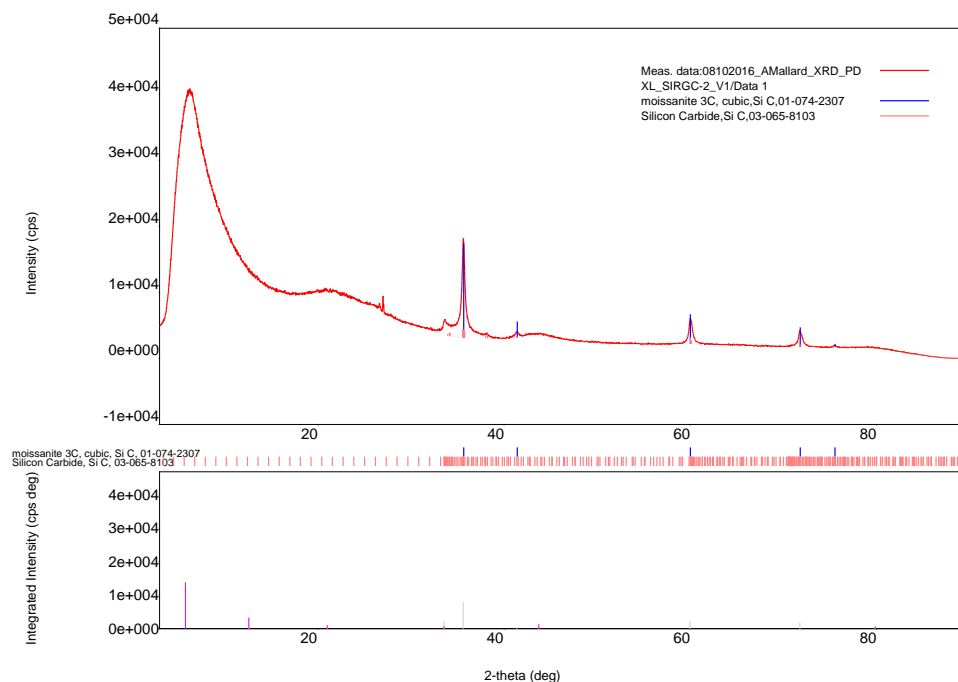
Figure 67: XRD Pattern for Si-Carburization at 1200 °C under H₂ Atmosphere

Although peak heights differ, the XRD patterns obtained from samples carburized at 1400 °C under Ar, and at 1200 °C under H_2, are identical and indicate that β-SiC is the only phase present. The decrease in peak height may indicate that less of the silicate anions were carburized at 1200 °C. However, it is difficult to make this determination using X-ray diffraction when only one crystalline phase is present.

Images of the H_2-carburized Si-loaded precursor samples were generated by SEM. An example of these images is presented in Figure 68.
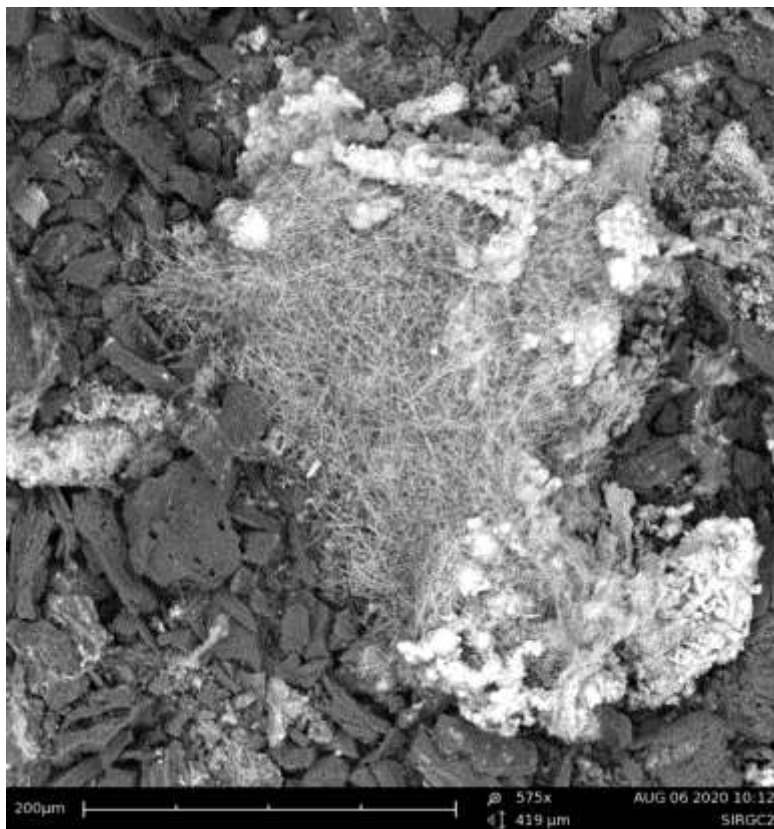
Figure 68: SEM Image of Carburized Si-Loaded (1200 °C, H_2, 6 h)

The image shows the presence of SiC formed on the surface of the activated carbon

matrix. In a manner similar to what was observed in the samples carburized under Ar, the SiC is

present as "nodules" and the whisker-like morphology. The SiC "whiskers" can be several

microns in length and often approach submicron thicknesses. The number of nodules present in

the H_2 samples appears to be greater than what was observed in the Ar samples. This behavior

may be due to the reducing nature of the H_2 atmosphere improving the carburization reaction

kinetics and causing SiC nucleation to occur at a rate that prevented the formation of the

"whisker" structure.

In order to compare SiC concentrations between different carburization experiments, a 10

wt. % addition of zinc oxide was added to each sample prior to analysis. The results presented in

Table XVII and Table XVIII are the WPPF qualitative analysis results for the series of carburization experiments using Si-loaded precursor.

Table XVII: Effect of Temperature on Si-Loaded Precursor Carburization (Ar, 20 h)

Experiment	Temperature (°C)	ZnO (Rel. Wt. %)	SiC (Rel Wt. %)
SiC-IS-1	1400	60.1	39.9
SiC-IS-2	1300	63.4	37.3
SiC-IS-3	1200	81.4	18.6

Table XVIII: Effect of Time on Si-Loaded Precursor Carburization (H_2, 1200 °C)

Experiment	Time (h)	ZnO (Rel. Wt. %)	SiC (Rel Wt. %)
SiC-IS-6	4	79.8	20.4
SiC-IS-4	6	70.6	29.5
SiC-IS-5	8	70.2	24.5

The zinc oxide additions to the carburized samples enabled a comparison to be made between the relative amounts of silicon carbide produced under different experimental conditions. The formation of SiC is shown to decrease in the inert atmosphere experiments as the temperature is decreased from 1400 °C to 1200 °C. The results presented in Table XVIII Table XVIII: Effect of Time on Si-Loaded Precursor Carburization (H_2, 1200 °C)however, do not appear to demonstrate any discernable trend. This behavior suggests that, at 1200 °C, the carburization of the precursor is not time dependent. The relative wt. % values for silicon carbide produced at 1200 °C under H_2 are greater than what was produced under Ar. The results indicate that hydrogen gas atmospheres improved carburization at lower operating temperatures.

5.2.4. Carburization Mechanisms

The morphology of the carbide particles produced through the WC synthesis process indicates that some coalescence of the adsorbed tungsten species occurred during carburization. A mechanism for the particle growth on the surface of the activated carbon can be proposed from the observed carburization products and the available literature on the subject. It is likely that the adsorbed tungstate species, which generally exist as complexed anions, were first reduced to W metal and subsequently carburized given the presence of residual W metal still present in small amounts in the carburization products. During the carburization process, it is possible that the reduced tungsten particles experienced simultaneous carburization, primarily via diffusion of CH_4, and particle agglomeration through a combined process of particle migration and coalescence (PMC), where surface particles agglomerate through Brownian motion across the substrate surface, as well as Ostwald ripening to minimize the surface energy of the carbon-mounted particles.

Literature accounts support the application of PMC and Ostwald ripening to the growth of metal particles supported on substrates. Hansen et al. proposed a mechanism for the sintering of metal-supported particles observed in certain catalysts. The authors determined that Ostwald ripening was the dominant mechanism for particle growth and agglomeration at temperatures below 750 °C, but that PMC was found to also occur as part of the agglomeration process at higher temperatures, but only with particles in close proximity to one another [92].

From observing the thermodynamic model of the system, combined with the results from the carburization experiments, it can be proposed that carburization occurred by the conversion of the adsorbed molybdate species to MoO_2 rather than a metallic Mo species. MoO_2 is thermodynamically stable at the temperatures used in the Mo-carburization design of experiments unlike metallic Mo which is thermodynamically stable at higher temperatures (>900

°C). Particle growth is likely due to a mechanism similar to what was proposed for W-carburization where the combined effects of Ostwald ripening and localized PMC allowed for the growth of Mo-containing particles on the activated carbon surface.

It is evident that carburization of the Si-loaded precursor occurred through the conventional mechanism of the production of the $SiO_{(g)}$ intermediate species. However, the formation of whisker-like SiC morphologies was not initially expected. Further literature research revealed that while whisker formation usually requires the use of a catalyst, it is possible for impurities within carbon sources to act as nucleation sites for whisker growth. Certain surface formations, such as edges, were also shown to act as nucleation sites for whisker formation as these surface formations are sites for higher surface energies when considering silica-coated carbon [56]. The carbon used in these experiments is not of a uniform shape and a number of sharp points and edges can be seen that may have provided the surface energies necessary for SiC whisker formation.

5.3. Separation Study

Micrographs of the jet-milled, carburized W-loaded precursor are presented in Figure 69. Figure 69(a) is an image of the jet-milled material before undergoing the LMT heavy liquid separation process, while Figure 69(b) is an image of the jet-milled material after undergoing the LMT heavy liquid separation process.

| (a) | (b) |
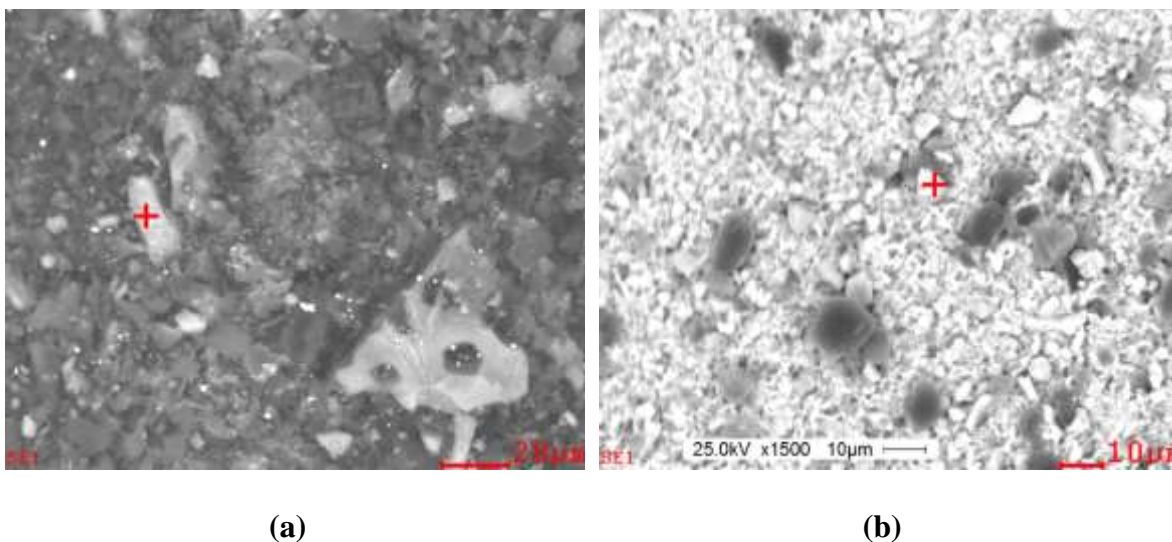
Figure 69: Micrographs of Jet-Milled Carburized Material Before (a) and After (b) LMT Separation

The SEM images show that the LMT separation significantly alters the jet-milled material. An EDAX analysis of the "bright" particles show they represent the W-containing materials while the "dark" particles present in the sample correspond to particles of the activated carbon matrix. The SEM images of the high-density material collected after LMT separation show a higher concentration of W-containing particles than what is present in the carburized material that has not undergone LMT separation. Because of this phenomenon, it is highly possible that the heavy liquid separation method is capable of removing a large portion of the activated carbon matrix.

An SEM image of the high-density material collected after centrifugation in LMT solution, and being passed through a 0.45 μm syringe filter, is presented in Figure 70.
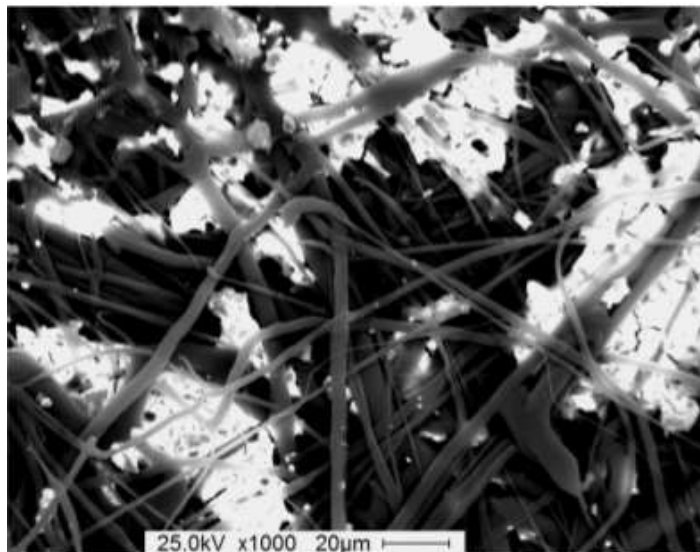
Figure 70: Micrograph of Separated Tungsten-Containing Particles Entrained within Filter Media [89]

The SEM image shows the high-density, mixed crystals of WC/W$_2$C/W formed during

carburization, were entrained within the filter media with little residual activated carbon present

amongst the high-density material. The lack of residual carbon particles indicates that density

separations have the potential to separate the carburized product from the residual activated

carbon following short jet milling operations. Although the LMT separation process was capable

of removing much of the excess carbon, the heavy liquid separation method is difficult and

costly to scale up and there exists a potential for sample contamination from the tungstate

solution used to separate the carbon from the WC/W$_2$C/W crystals. Alternative methods of

separation needed to be investigated to establish proof-of-concept for the carbide separation

process.

A representative micrograph of the surrogate WC-C material following separation by the

standing wave process is presented in Figure 71. The image is of the higher density material

collected from the center of the watch glass.
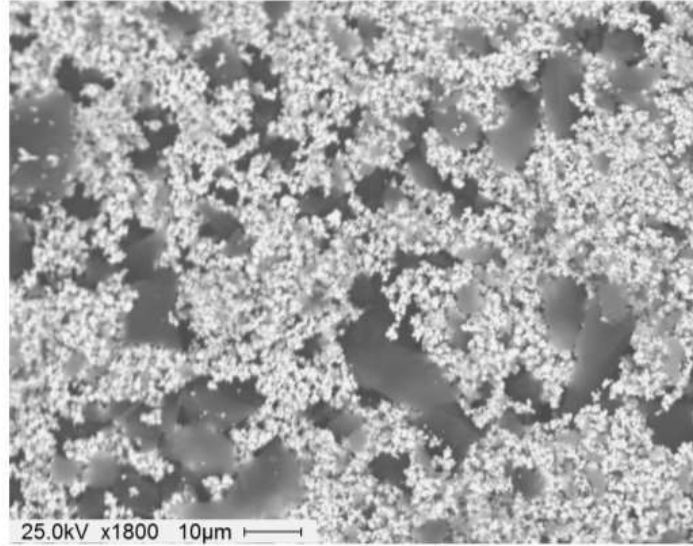
Figure 71: Surrogate WC-C Material Following Standing Wave Separation [88]

A qualitative analysis of the images taken of the collected surrogate material showed that the standing wave separation process was able to concentrate the WC particles. From the observations made from the surrogate WC-C samples, fully liberated WC particles should separate from the much less dense carbon matrix. Some residual carbon does remain in this concentrate likely due to larger carbon particles, or an agglomeration of smaller carbon particles, behaving in a similar manner to the denser WC particles. Carbon is, by nature, hydrophobic and fine carbon particles will agglomerate when suspended in water.

It was predicted that the addition of surfactants could improve the separation of the WC particles from the carbon matrix. The results of the surfactant experiments done using the surrogate WC-C material are presented in Table XIX.

Table XIX: Effect of Surfactant Type and Concentration on Standing Wave Separation Mass Recovery [88]

Surfactant Type	Surfactant Additions (µL)	Recovered WC Mass (%)
None	0	13.2
SDDS	25	42.8
SDDS	100	35.5
SDDS	400	30.8
SDS	25	36.5
SDS	100	61.1
SDS	400	43.0

Standing wave separations made without the addition of surfactant were found by EDAX calculations to only collect 13.2% of the initial WC added to the surrogate WC-C samples. The addition of surfactant, particularly SDS significantly increased the amount of collected WC with a 100 µL addition of SDS causing 61.1% of the WC to be collected from the center of the rotated watch glass.

Standing wave separations with surfactant were also carried out using actual milled carburized W-loaded precursor. Samples of the collected higher density material were analyzed via SEM. A representative micrograph of the separated carburized material is presented in Figure 72.
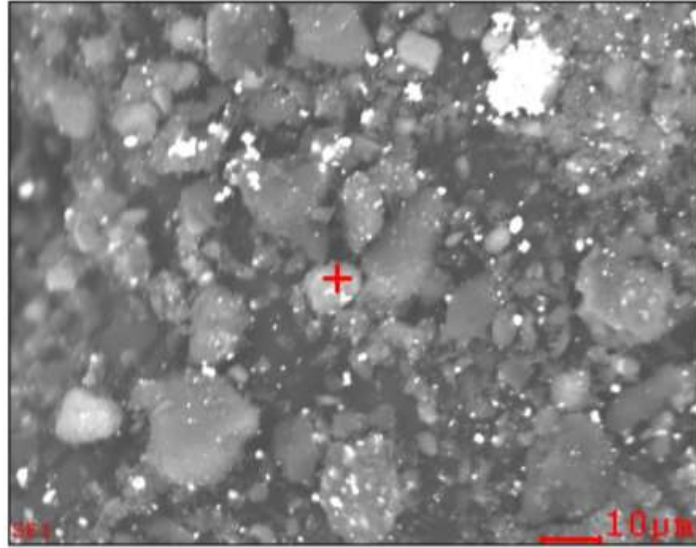
Figure 72: Carburized W-Loaded Precursor After Undergoing Standing Wave Separation [88]

The SEM analysis of the collected material from the standing wave separation experiments involving milled W-loaded precursor showed that the concentrated higher density material contained more carbon than what was found in the experiments using surrogate WC-C material. This is likely due to insufficiently liberated carbide particles that were still bound to the activated carbon matrix. Large (>10micron) carbon particles can be observed in the micrograph showing that the milling operations carried out on the carburized W-loaded precursor did not sufficiently break apart the carbon matrix and a number of carbon particles can be observed with bright W-containing crystals still attached to their surface.

6. Conclusions

This research was predicated on the hypothesis that adsorbing metal ions onto the surface of a source of carbon will produce a precursor material that, upon reduction and carburization, will result in the synthesis of fine-grained micron/submicron-scale carbide particles on the activated carbon surface. The research conducted in this investigation supports this hypothesis. Carbide particles were synthesized on the surface of the anion-loaded precursors and the size and morphology of these particles were affected by the adsorption of these anions onto the surface of activated carbon. Conversions greater than 90% were achieved with all three carbides investigated in this research.

The presented work shows that a statistically sound and experimentally confirmed process was developed for synthesizing micron/submicron sized carbide particles from anion-loaded precursors at operating temperatures significantly lower than those used in conventional carbide synthesis processes. This process is capable of being altered to synthesize multiple carbides of interest including WC, Mo_2C, and SiC. It should be noted that no other work was found that implemented the same process of adsorption, reduction, carburization, and separation that is the subject of this research. The use of response surface modelling to optimize tungstate, molybdate, and silicate loading onto activated carbon, as well as the carburization behavior of these anion-loaded precursors were not observed in any literature sources.

A flow diagram of the process developed through this work, including adsorption, carburization, and separation steps, is presented in Figure 73.
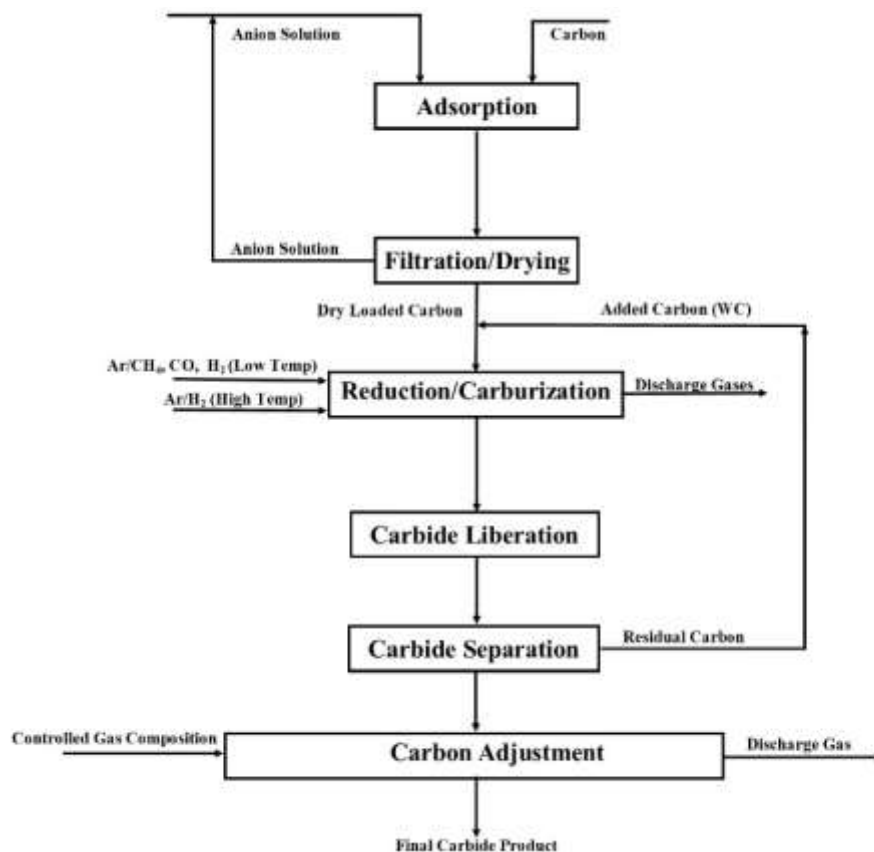
Figure 73: Flow Diagram of Carburization Process

The process flow diagram begins with the production of anion precursor through the adsorption of anions onto activated carbon. Anion solution can be collected following filtration and regenerated for continued use. Reduction and carburization could take place in a rotary furnace setup; however, the use of fluid bed technology may be required for the production of WC. The implementation of a fluidized bed to improve carbide conversion is currently being investigated. A static bed furnace is likely required for SiC whisker growth, but further study and scale-up of SiC carburization is required. Following the reduction and carburization of the anion-loaded precursor, liberation of the carbide particles can be carried out through grinding of the carburized precursor. Ball milling and jet milling have been used to liberate the carbide particles, but this step could include other types of grinding methods depending on future study. The liberation and separation of the carbide particles is currently under investigation to develop a

quantitative evaluation of various methods of particle liberation and separation techniques. The separation process would also allow for excess carbon to be recycled for use in the production of WC as that process requires the addition of carbon to promote WC conversion. Proof-of-concept has been established for all of the steps in the process related to adsorption, carburization, and separation. The final carbon adjustment step was included as a potential final carbon-removal step where a controlled CO/CO_2 ratio could be maintained to selectively oxidize any residual carbon following the tested separation methods.

Statistical modeling was used to predict adsorption behavior to maximize anion loading onto the activated carbon matrix. Tungstate and molybdate adsorption were maximized using the same optimal adsorption conditions: 25 °C, 2 h, an initial W/Mo concentration of 18,000 mg/L, and a solution pH of 2.0. These adsorption conditions produced multiple batches of precursor with loadings of 0.35 g W/g C and 0.32 g Mo/g C. Silicate adsorption behavior was also modeled to determine statistically valid optimal adsorption conditions. Silicate loadings of 0.27 g Si/g C were achieved using the following adsorption conditions: 25 °C, 2 h, and an initial Si concentration of 50,000 mg Si/L.

Statistical modeling was also able to predict and optimize the carburization behavior of the W-loaded and Mo-loaded precursors. Relative WC concentrations of 94.3% were achieved at 950 °C, a carburization time of 8 h, a reducing gas atmosphere consisting of 80% CH_4, 10% CO, and 10% H_2, and a blended furnace charge containing 20% added activated carbon. Carbide products synthesized through this process were found to be relatively small in size (approx. 2 microns) and could be suitable for potential structural and catalytic applications. Although high degrees of conversion to WC were possible through this process, complete conversion may require an alternative furnace setup, such as a fluidized bed reactor, that would allow for

improved exposure of the furnace charge to the reducing/carburizing gas atmosphere and overcome the kinetic inhibitions observed in this process. The temperatures required to achieve these high levels of WC also induce process issues due to the formation of naphthalene at these temperatures as the CH_4 begins to react with itself at temperatures exceeding 900 °C. The use of a fluidized bed reactor could reduce the required operating temperatures needed for complete carburization and eliminate the naphthalene production issues observed in this work. Liberation and separation of the W-containing particles from the residual carbon matrix was shown to be feasible through the use of milling and the exploitation of the differences in density and hydrophobicity of carbon and the W-containing particles.

The carburization of the Mo-loaded precursor also produced Mo_2C conversions exceeding 90% at 850 °C, a carburization time of at least 1 h, and a CH_4:H_2 ratio of 2.9. The synthesis of Mo_2C was found to be a more thermally driven process than the WC synthesis process and less susceptible to changes due to gas composition. The products of the carburization process were found to be relatively small in size, with some carbide particles being submicron in size. Although complete conversion to Mo_2C was observed in the smaller scale tube furnace experiments, this behavior was not observed in scale-up experiments and is most likely due to the furnace charge experiencing insufficient exposure to the reducing/carburizing gas atmosphere inside the rotary kiln.

The adsorption/carburization process was shown to be capable of synthesizing SiC at temperatures lower than commercial carburization methods. Silicon carbide "whiskers" were formed at temperatures as low as 1200 °C under H_2. The SiC structures formed during carburization are several microns long with thicknesses also approaching submicron sizes.

Methods for separating the extremely fine carbide particles from the carbon matrix included both heavy liquid separations, and surfactant-aided standing wave separations. The separation experiments demonstrated that separation of the fine carbide particles is possible and would allow for this process to be used to produce carbides for use in the development of sintered carbide products.

7. Recommendations

The use of a fluidized bed reactor should also be considered to induce complete carburization of the molybdate anions to Mo_2C. Separation experiments should also be carried out on the carburized Mo-loaded precursor to determine the feasibility of separating the carburization products from the residual carbon matrix. The catalytic applications of the synthesized Mo_2C should also be investigated as the small particle sizes produced by this process may allow for the carburization products to be used in this manner.

Fluidized bed reactor experiments should also be conducted using the W-loaded precursor to fully convert the precursor to WC as well as potentially lowering the required carburization temperature to eliminate the naphthalene-production issues which occurred frequently during the high-temperature W-carburization experiments. Other potential options for improving carburization could also include replacing CH_4 with another carbon-containing gas to determine its effect on carburization.

The separation methods described in this work also should be investigated further to provide optimal parameters for maximum carbide product recovery. The improvements made to the process using surfactants may allow for the low-density carbon to be separated via flotation or other separation methods in addition to those used in this work.

Additional experimentation should also be conducted on improving the SiC synthesis process. The intermediate gas phase that occurs in the SiC mechanism may not allow for the use of a fluidized bed reactor. Scale-up experiments, and a statistical model to optimize carburization parameters, should be produced to predict Si-carburization behavior.

The adsorption/carburization process developed in this work should also be applied to synthesizing other carbides of interest such as vanadium carbide, or other metal carbides with a

water-soluble salt available. New carbides of interest would also require optimization of their

adsorption parameters to produce precursor for the carburization experiments.

8. References

[1] "Metal Carbides," *Total Materia*, 2006. [Online]. Available:

https://www.totalmateria.com/page.aspx?ID=CheckArticle&site=ktn&NM=158.

[Accessed: 16-Apr-2016].

[2] Hugh Pierson, "Chromium, Molybdenum, and Tungsten Carbides," in *Handbook of Refractory Carbides and Nitrides: Properties, Characteristics, Processing, and Applications*, Westwood, NJ: Noyes Publications, 1996, pp. 114–116.

[3] H. Moissan, "Preparation au four électrique de quelques mètaux réfractaires: tungstène, molybdène, vanadium.," *C R*, vol. 116, pp. 1225–1227, 1893.

[4] (AZoM), "Tungsten Carbide - An Overview," *AZo Materials*, 2002. [Online]. Available: https://www.azom.com/article.aspx?ArticleID=1203.

[5] (BIS Research), "Global Tungsten Carbide Market: Focus on Application (Cutting Tools, Mining & Drilling Tools, Wear Parts, Mill Products, and Others) and End-Use Industry-Analysis and Forecast: 2018-2028," New York, 2019.

[6] Joyce Chepkemoi, "List of Countries by Tungsten Production," *WorldAtlas*, 2017. [Online]. Available: https://www.worldatlas.com/articles/list-of-countries-by-tungsten-production.html.

[7] Zaoxue Yan, Mei Cai, and Pei Kang Shen, "Nanosized tungsten carbide synthesized by a novel route at low temperature for high performance electrocatalysis," *Sci. Rep.*, vol. 3, pp. 1–7, 2013, doi: 10.1038/srep01646.

[8] J. B. O. Santos, G. P. Valença, and J. A. J. Rodrigues, "Catalytic Decomposition of Hydrazine on Tungsten Carbide: The Influence of Adsorbed Oxygen," *J. Catal.*, vol. 210, no. 1, pp. 1–6, Aug. 2002, doi: 10.1006/JCAT.2002.3634.

[9]   Yoshinori Hara, Noriko Minami, and Hiroaki Itagaki, "Synthesis and characterization of high-surface area tungsten carbides and application to electrocatalytic hydrogen oxidation," *Appl. Catal. A Gen.*, vol. 323, pp. 86–93, 2007, doi: 10.1016/j.apcata.2007.02.011.

[10]   Yoshinori Hara, Noriko Minami, Hajime Matsumoto, and Hiroaki Itagaki, "New synthesis of tungsten carbide particles and the synergistic effect with Pt metal as a hydrogen oxidation catalyst for fuel cell applications," *Appl. Catal. A Gen.*, vol. 332, no. 2, pp. 289–296, 2007, doi: 10.1016/j.apcata.2007.08.030.

[11]   M. F. Zawrah, "Synthesis and characterization of WC-Co nanocomposites by novel chemical method," *Ceram. Int.*, vol. 33, no. 2, pp. 155–161, 2007, doi: 10.1016/j.ceramint.2005.09.010.

[12]   Leo J. Prakash, "Application of fine grained tungsten carbide based cemented carbides," *Int. J. Refract. Met. Hard Mater.*, vol. 13, no. 5, pp. 257–264, Jan. 1995, doi: 10.1016/0263-4368(95)92672-7.

[13]   Z. Zak Fang, Xu Wang, Taegong Ryu, Kyu Sup Hwang, and H. Y. Sohn, "Synthesis, sintering, and mechanical properties of nanocrystalline cemented tungsten carbide - A review," *Int. J. Refract. Met. Hard Mater.*, 2009, doi: 10.1016/j.ijrmhm.2008.07.011.

[14]   Charles F. Davidson, Guy B. Alexander, and Milton E. Wadsworth, "Initial Kinetics of Tungsten Carburization by Methane," *Metall. Trans. B*, vol. 9B, pp. 553–557, 1978.

[15]   Rasit Koc and Suneel K. Kodambaka, "Tungsten Carbide Synthesis from Novel Precursors.pdf," *J. Eur. Ceram. Soc.*, vol. 20, pp. 1859–1869, 2000.

[16]   Joel O. Hougen, Robert R. Reeves, and Gene G. Mannella, "Reduction of Tungsten Oxides with Hydrogen," *Ind. Eng. Chem.*, vol. 48, no. 2, pp. 318–320, 1956, doi:

10.1021/ie50554a042.

[17]   G. A. Swift and R. Koc, "Formation of WC powders using carbon coated precursors," *Journal of Materials Science*, vol. 35, no. 9. pp. 2109–2113, 2000, doi: 10.1023/A:1004760719005.

[18]   F. F. .. Medeiros, S. .. De Oliveira, C. .. De Souza, A. G. .. Da Silva, U. .. Gomes, and J. .. De Souza, "Synthesis of tungsten carbide through gas–solid reaction at low temperatures," *Mater. Sci. Eng. A*, vol. 315, no. 1–2, pp. 58–62, Sep. 2001, doi: 10.1016/S0921-5093(01)01214-X.

[19]   M. Nakazawa and H. Okamoto, "XPS study of WC formation process," *Applied Surface Science*, vol. 27, no. 1. pp. 85–92, 1986, doi: 10.1016/0169-4332(86)90097-8.

[20]   Guohua Li, Chun'an Ma, Junyan Tang, and Yifan Zheng, "Preparation of tungsten carbide porous sphere core wrapped by porous multiwall," *Mater. Lett.*, vol. 61, no. 4–5, pp. 991–993, 2007, doi: 10.1016/j.matlet.2006.06.037.

[21]   Zhen Xiong, Gangqin Shao, Xiaoliang Shi, Xinglong Duan, and Li Yan, "Ultrafine hardmetals prepared by WC-10 wt.%Co composite powder," *Int. J. Refract. Met. Hard Mater.*, vol. 26, no. 3, pp. 242–250, 2008, doi: 10.1016/j.ijrmhm.2007.04.004.

[22]   P. Seegopaul, L. E. McCandlish, and F. M. Shinneman, "Production capability and powder processing methods for nanostructured WC-Co powder," *Int. J. Refract. Met. Hard Mater.*, vol. 15, no. 1–3, pp. 133–138, Jan. 1997, doi: 10.1016/S0263-4368(96)00044-3.

[23]   Jianhua Ma and Yihong Du, "Synthesis of nanocrystalline hexagonal tungsten carbide via co-reduction of tungsten hexachloride and sodium carbonate with metallic magnesium," *J. Alloys Compd.*, vol. 448, no. 1–2, pp. 215–218, 2008, doi: 10.1016/j.jallcom.2006.10.060.

[24] Cristina Giordano, Christian Erpen, Weitang Yao, and Markus Antonietti, "Synthesis of Mo and W carbide and nitride nanoparticles via a simple 'urea glass' route," *Nano Lett.*, vol. 8, no. 12, pp. 4659–4663, 2008, doi: 10.1021/nl8018593.

[25] J. C. Kim and B. K. Kim, "Synthesis of nanosized tungsten carbide powder by the chemical vapor condensation process," *Scr. Mater.*, vol. 50, no. 7, pp. 969–972, 2004, doi: 10.1016/j.scriptamat.2004.01.015.

[26] T. Danny Xiao, Xinglong Tan, Maozhong Yi, Shigao Peng, Fangcai Peng, Jiangao Yang, and Yu Dai, "Synthesis of Commercial-Scale Tungsten Carbide-Cobalt (WC/Co) Nanocomposite Using Aqueous Solutions of Tungsten (W), Cobalt (Co), and Carbon (C) Precursors," *J. Mater. Sci. Chem. Eng.*, vol. 02, no. 07, pp. 1–15, 2014, doi: 10.4236/msce.2014.27001.

[27] Zaoxue Yan, Guoqiang He, Mei Cai, Hui Meng, and Pei Kang Shen, "Formation of tungsten carbide nanoparticles on graphitized carbon to facilitate the oxygen reduction reaction," *J. Power Sources*, vol. 242, pp. 817–823, 2013, doi: 10.1016/j.jpowsour.2013.05.161.

[28] N. Hugot, A. Desforges, S. Fontana, J. F. Marêché, C. Hérold, A. Albiniak, and G. Furdin, "Solid-state chemistry route for supported tungsten and tungsten carbide nanoparticles," *J. Solid State Chem.*, vol. 194, pp. 23–31, 2012, doi: 10.1016/j.jssc.2012.07.027.

[29] (MatWeb), "Molybdenum Carbide, Mo2C," 1996. [Online]. Available: http://www.matweb.com/search/datasheet_print.aspx?matguid=3cbb589aeb7e4d5aadb67e1f0f9e996e.

[30] Yabo Wang, Wenguang Tu, Jindui Hong, Wei Zhang, and Rong Xu, "Molybdenum carbide microcrystals: Efficient and stable catalyst for photocatalytic H2 evolution from

water in the presence of dye sensitizer," *J. Mater.*, 2016, doi: 10.1016/j.jmat.2016.09.003.

[31] Lei Liao, Xiaojun Bian, and Yi Tang, "A Nanoporous Molybdenum Carbide Nanowire as an Electrocatalyst for Hydrogen Evolution Reaction," *Energy Environ. Sci.*, vol. 7, no. January, pp. 387–392, 2014, doi: 10.1039/C3EE42441C.Energy.

[32] Joshua A. Schaidle, Neil M. Schweitzer, Olabode T. Ajenifujah, and Levi T. Thompson, "On the preparation of molybdenum carbide-supported metal catalysts," *J. Catal.*, vol. 289, pp. 210–217, May 2012, doi: 10.1016/J.JCAT.2012.02.012.

[33] Ahmad Hanif, Tiancun Xiao, Andrew P. E. York, Jeremy Sloan, and Malcolm L. H. Green, "Study on the structure and formation mechanism of molybdenum carbides," *Chem. Mater.*, vol. 14, no. 3, pp. 1009–1015, 2002, doi: 10.1021/cm011096e.

[34] Gerardo Vitale, Héctor Guzmán, Maria L. Frauwallner, Carlos E. Scott, and Pedro Pereira-Almao, "Synthesis of nanocrystalline molybdenum carbide materials and their characterization," *Catal. Today*, vol. 250, pp. 123–133, Jul. 2015, doi: 10.1016/J.CATTOD.2014.05.011.

[35] Hua Min Wang, Xiao Hui Wang, Ming Hui Zhang, Xiao Yong Du, Wei Li, and Ke Yi Tao, "Synthesis of bulk and supported molybdenum carbide by a single-step thermal carburization method," *Chem. Mater.*, vol. 19, no. 7, pp. 1801–1807, 2007, doi: 10.1021/cm0615471.

[36] Xiao-Hui Wang, Hong-Ling Hao, Ming-Hui Zhang, Wei Li, and Ke-Yi Tao, "Synthesis and characterization of molybdenum carbides using propane as carbon source," *J. Solid State Chem.*, vol. 179, no. 2, pp. 538–543, Feb. 2006, doi: 10.1016/J.JSSC.2005.11.009.

[37] A. Szymańska-Kolasa, M. Lewandowski, C. Sayag, and G. Djéga-Mariadassou, "Comparison of molybdenum carbide and tungsten carbide for the hydrodesulfurization of

dibenzothiophene," *Catal. Today*, vol. 119, no. 1–4, pp. 7–12, Jan. 2007, doi: 10.1016/J.CATTOD.2006.08.021.

[38]   J. S. Lee, S. T. Oyama, and M. Boudart, "Molybdenum carbide catalysts. I. Synthesis of unsupported powders," *J. Catal.*, 1987, doi: 10.1016/0021-9517(87)90218-1.

[39]   N. Arul Dhas and A. Gedanken, "Sonochemical Synthesis of Molybdenum Oxide- and Molybdenum Carbide-Silica Nanocomposites," *Chem. Mater.*, vol. 9, no. 12, pp. 3144–3154, 1997, doi: 10.1021/cm9704488.

[40]   Fei Wang, Junming Xu, Jianchun Jiang, Peng Liu, Fanglin Li, Jun Ye, and Minghao Zhou, "Hydrotreatment of vegetable oil for green diesel over activated carbon supported molybdenum carbide catalyst," *Fuel*, vol. 216, pp. 738–746, Mar. 2018, doi: 10.1016/J.FUEL.2017.12.059.

[41]   Leroy Covington, Kamalesh Munirathinam, Akand Islam, and Kenneth Roberts, "Synthesis and characterization of nanostructured molybdenum & tungsten carbide materials, and study of diffusion model," *Polish J. Chem. Technol.*, vol. 14, no. 1, pp. 28–34, 2012, doi: 10.2478/v10026-012-0055-8.

[42]   C. P. B. Araujo, C. P. De Souza, L. M. D. Maia, M. V. M. Souto, and C. M. Barbosa, "On the synthesis of molybdenum carbide with cobalt addition via gas-solid reactions in a CH4/H2 atmosphere," *Brazilian J. Chem. Eng.*, vol. 33, no. 3, pp. 577–588, 2016, doi: 10.1590/0104-6632.20160333s20150107.

[43]   Quanli Zhu, Qifeng Chen, Xiaobin Yang, and Dongxian Ke, "A new method for the synthesis of molybdenum carbide," *Mater. Lett.*, vol. 61, no. 29, pp. 5173–5174, Dec. 2007, doi: 10.1016/J.MATLET.2007.04.056.

[44]   Kousaburo Ohashi, Kiyoko Murakami, and Katsumi Yamamoto, "Adsorption Behavior of

Tungsten(VI) Onto Activated Carbon," *Bunseki Kagaku*, vol. 32, no. 10, pp. E313–E319, 1983, doi: 10.2116/bunsekikagaku.32.10_E313.

[45]   J. J. Cruywagen and A. T. Pienaar, "The adsorption of tungsten(VI) on activated carbon from 1.0 M Na(H)Cl solution," *Polyhedron*, vol. 8, no. 1, pp. 71–76, 1989, doi: 10.1016/S0277-5387(00)86380-9.

[46]   Pirouz Derakhshi, Hossein Ghafourian, Morteza Khosravi, and Mohammad Rabani, "Optimization of Molybdenum Adsorption from Aqueous Solution Using Granular Activated Carbon," *World Appl. Sci. J.*, vol. 7, no. 2, pp. 230–238, 2009.

[47]   Gernot Gruber, "Performance and Reliability Limiting Point Defects in SiC Power Devices," Graz University of Technology, 2016.

[48]   Philip J. Guichelaar, "Acheson Process," in *Carbide, Nitride and Boride Materials Synthesis and Processing*, Dordrecht: Springer Netherlands, 1997, pp. 115–129.

[49]   (Accuratus), "Silicon Carbide, SiC Ceramic Properties," 2013. [Online]. Available: https://accuratus.com/silicar.html.

[50]   (AZoM), "Silicon Carbide (SiC) Properties and Applications," *AZo Materials*, 2001. [Online]. Available: https://www.azom.com/properties.aspx?ArticleID=42.

[51]   Burak Ozpineci and Leon Tolbert, "Silicon Carbide: Smaller, Faster, Tougher," *IEEE Spectrum*, 2011. [Online]. Available: https://spectrum.ieee.org/semiconductors/materials/silicon-carbide-smaller-faster-tougher. [Accessed: 16-Apr-2016].

[52]   J. W. Palmour, J. A. Edmond, H. S. Kong, and C. H. Carter, "6H-silicon carbide devices and applications," *Phys. B Condens. Matter*, vol. 185, no. 1–4, pp. 461–465, Apr. 1993, doi: 10.1016/0921-4526(93)90278-E.

[53]   E. G. Acheson, "Production of Artificial Crystalline Carbonaceous Materials, Carborundum," 17911, 1892.

[54]   Xiang Li, Guangqing Zhang, Kai Tang, Oleg Ostrovski, and Ragnar Tronstad, "Synthesis of silicon carbide by carbothermal reductions of quartz in H2-Ar gas mixtures," in *The Fourteenth International Ferroalloys Congress Energy efficiency and environmental friendliness are the future of the global Ferroalloy industry*, 2015, pp. 548–554.

[55]   Hans Peter Martin, Ramona Ecke, and Eberhard Müller, "Synthesis of nanocrystalline silicon carbide powder by carbothermal reduction," *J. Eur. Ceram. Soc.*, 1998, doi: 10.1016/s0955-2219(98)00094-6.

[56]   K. L. Vyshnyakova, L. N. Pereselentseva, Z. G. Cambaz, G. N. Yushin, and Y. Gogotsi, "Whiskerisation of polycrystalline SiC fibres during synthesis," *Br. Ceram. Trans.*, vol. 103, no. 5, pp. 193–196, 2004, doi: 10.1179/096797804X4556.

[57]   G. Roewer, U. Herzog, K. Trommer, E. Müller, and S. Frühauf, "Silicon Carbide — A Survey of Synthetic Approaches, Properties and Applications," *High Perform. Non-Oxide Ceram. I*, vol. 101, pp. 59–135, 2007, doi: 10.1007/3-540-45613-9_2.

[58]   Kateryna Vyshnyakova, Gleb Yushin, Ludmila Pereselentseva, and Yury Gogotsi, "Formation of porous SiC ceramics by pyrolysis of wood impregnated with silica," *Int. J. Appl. Ceram. Technol.*, vol. 3, no. 6, pp. 485–490, 2006, doi: 10.1111/j.1744-7402.2006.02103.x.

[59]   Fumihiro Kawamura, Hisanori Yamane, Yamada Takahiro, Shu Yin, and Tsugio Sato, "Low-Temperature Fabrication of Porous b -SiC Ceramics in Sodium Vapor," *Am. Ceram. Soc.*, vol. 55, pp. 51–55, 2008, doi: 10.1111/j.1551-2916.2007.02021.x.

[60]   Mengning Ding and Alexander Star, "Synthesis of one-dimensional SiC nanostructures

from a glassy buckypaper," *ACS Appl. Mater. Interfaces*, vol. 5, no. 6, pp. 1928–1936, 2013, doi: 10.1021/am3031008.

[61] Lin Gao, "Synthesis of Nanocrystalline Tungsten and Tungsten Carbide Powders," Rutgers University, 1997.

[62] T. Iwai, I. Takahashi, and M. Handa, "Gibbs free energies of formation of molybdenum carbide and tungsten carbide from 1173 to 1573 K," *Metall. Trans. A*, vol. 17, no. 11, pp. 2031–2034, 1986, doi: 10.1007/BF02645000.

[63] Alexey S. Kurlov and Aleksandr I. Gusev, *Tungsten Carbides: Structure, Properties, and Application in Hardmetals*. New York: Springer International Publishing, 2013.

[64] Z. Q. Li, H. F. Zhang, X. B. Zhang, Y. Q. Wang, and X. J. Wu, "Nanocrystalline tungsten carbide encapsulated in carbon shells," *Nanostructured Materials*, vol. 10, no. 2–8. pp. 179–184, 1998, doi: 10.1016/S0965-9773(98)00054-3.

[65] Nicholas J. Welham, "Novel route to submicrometer tungsten carbide," *AIChE Journal*, vol. 46, no. 1. pp. 68–71, 2000, doi: 10.1002/aic.690460109.

[66] J. M. Gomes, A. E. Raddatz, and T. G. Carnahan, "Preparation of Tungsten Carbide by Gas Sparging Tungstate Melts," *Jom*, vol. 37, no. 12. pp. 29–32, 1985, doi: 10.1007/BF03259964.

[67] Andrey A. Rempel, "NONSTOICHIOMETRIC TRANSITION METAL COMPOUNDS," in *Proceedings of the 17th Israeli-Russian Bi-National Workshop*, 2018, pp. 167–189.

[68] Masaya Miyake, Minol Nakano, Takaharu Yamamoto, Akio Hara, Foreign Application, and Priority Data, "U . S . Patent Aug . 5 , 1980," no. 19, 1980.

[69] Primary Examiner-brooks H. Hunt, "United States Patent (19)," no. 19, 1981.

[70] Casimir J. Rosa, "Carbon diffusion in Mo2C as determined from carburization of Mo,"

Metall. Trans. A, vol. 14, no. 1, pp. 199–202, 1983, doi: 10.1007/BF02651616.

[71] Satyajeet Chaudhury, S. K. Mukerjee, V. N. Vaidya, and V. Venugopal, "Kinetics and mechanism of carbothermic reduction of MoO3 to Mo2C," *J. Alloys Compd.*, vol. 261, no. 1–2, pp. 105–113, 1997, doi: 10.1016/S0925-8388(97)00212-0.

[72] Alan W. Weimer, Kevin J. Nilsen, Gene A. Cochran, and Raymond P. Roach, "Kinetics of carbothermal reduction synthesis of beta silicon carbide," *AIChE J.*, vol. 39, no. 3, pp. 493–503, 1993, doi: 10.1002/aic.690390311.

[73] Giuseppe D'Amico, "Si-SiC based materials obtained by infiltration of silicon: study and applications," Politecnico di Torino, 2015.

[74] William Rafaniello, "Critical Powder Characteristics," in *Carbide, Nitride and Boride Materials Synthesis and Processing*, A. W. Weimer, Ed. London, 1997, pp. 43–76.

[75] A. W. P. Fung, A. M. Rao, K. Kuriyama, M. S. Dresselhaus, G. Dresseliiaus, and M. Endot, "Characterization of Activated Carbon Fibers," *MRS Proc.*, vol. 209, 1990, doi: 10.1557/proc-209-335.

[76] Manish Patel and J. Subrahmanyam, "Synthesis of nanocrystalline molybdenum carbide (Mo2C) by solution route," *Mater. Res. Bull.*, 2008, doi: 10.1016/j.materresbull.2007.09.025.

[77] Hans Swenson and Nicholas P. Stadie, "Langmuir's Theory of Adsorption: A Centennial Review," *Langmuir*, 2019, doi: 10.1021/acs.langmuir.9b00154.

[78] Rajendra Dongre, "Pb ({II}) {Ions} {Adsorption} onto {Biomaterial} {Chitosan} {Hydrogel} {Beads} - {Isotherm} {And} {Kinetic} {Studies}," vol. 6, no. March, 2017.

[79] Joseph Slcopp, "Derivation of the freundlich adsorption isotherm from kinetics," *J. Chem. Educ.*, vol. 86, no. 11, pp. 1341–1343, 2009, doi: 10.1021/ed086p1341.

[80] J. J. Cruywagen and H. F. de Wet, "Equilibrium study of the adsorption of molybdenum(VI) on activated carbon," *Polyhedron*, vol. 7, no. 7, pp. 547–556, 1988, doi: 10.1016/S0277-5387(00)86331-7.

[81] Eri Yamamoto, Jun Kobayashi, Keiko Kanamaru, Toshiaki Miura, Fujio Watanabe, Noriyuki Kobayashi, and Masanobu Hasatani, "Hydrophilication of activated carbon by impregnating silica into pores," *J. Chem. Eng. Japan*, vol. 36, no. 3, pp. 348–352, 2003, doi: 10.1252/jcej.36.348.

[82] C. Y. Tso and Christopher Y. H. Chao, "Activated carbon, silica-gel and calcium chloride composite adsorbents for energy efficient solar adsorption cooling and dehumidification systems," *Int. J. Refrig.*, vol. 35, no. 6, pp. 1626–1638, 2012, doi: 10.1016/j.ijrefrig.2012.05.007.

[83] Xiaofang Yang, Payman Roonasi, and Allan Holmgren, "A study of sodium silicate in aqueous solution and sorbed by synthetic magnetite using in situ ATR-FTIR spectroscopy," *J. Colloid Interface Sci.*, vol. 328, no. 1, pp. 41–47, 2008, doi: 10.1016/j.jcis.2008.08.061.

[84] Kofi Adu-Wusu and William R. Wilcox, "Kinetics of silicate reaction with gibbsite," *J. Colloid Interface Sci.*, vol. 143, no. 1, pp. 127–138, 1991, doi: 10.1016/0021-9797(91)90445-E.

[85] S. Kato, T. Yamaki, S. Yamamoto, T. Hakoda, K. Kawaguchi, T. Kobayashi, A. Suzuki, and T. Terai, "Preparation of tungsten carbide nanoparticles by ion implantation and electrochemical etching," *Nucl. Instruments Methods Phys. Res. Sect. B Beam Interact. with Mater. Atoms*, vol. 314, pp. 149–152, 2013, doi: 10.1016/j.nimb.2013.05.052.

[86] Vladimir M. Nikolic, Ivana M. Perovic, Nemanja M. Gavrilov, Igor A. Pašti, Aleksandra

B. Saponjic, Predrag J. Vulic, Slavko D. Karic, Biljana M. Babic, and Milica P. Marceta Kaninski, "On the tungsten carbide synthesis for PEM fuel cell application - Problems, challenges and advantages," *Int. J. Hydrogen Energy*, vol. 39, no. 21, pp. 11175–11185, 2014, doi: 10.1016/j.ijhydene.2014.05.078.

[87]   (StatEase), "Box-Cox Plot," *Design-Expert: General Sequence of Analysis*. [Online]. Available: https://www.statease.com/docs/v11/contents/analysis/box-cox-plot/.

[88]   Trenin K. Bayless, Jerome P. Downey, Grant C. Wallace, and Mark D. Aberle, *Density Separation of Mixed Carbide Colloids via Standing Wave Physics*. Springer International Publishing.

[89]   Grant C. Wallace, Jerome P. Downey, Jannette Chorney, Katie Schumacher, Trenin Bayless, Alaina Mallard, Auva Speiser, and Elizabeth Raiha, "Synthesis of Carbide Ceramics from Activated Carbon Precursors Loaded with Tungstate, Molybdate, and Silicate Anions," *Adv. Ceram. Environ. Funct. Struct. Energy Appl. Ceram. Trans.*, vol. 265, pp. 137–149, 2018.

[90]   Grant C. Wallace, Jerome P. Downey, Jannette Chorney, Katie Schumacher, and Alaina Mallard, "Synthesis of Nanocrytalline Carbide Ceramics Via Reduction of Anion-Loaded Activated Carbon Precursors," in *9th International Symposium on High-Temperature Metallurgical Processing*, 2018, pp. 125–134.

[91]   Grant C. Wallace, Jerome P. Downey, Jannette Chorney, Katie Schumacher, and Trenin Bayless, "Statistical Optimization of Tungsten Carbide Synthesis Parameters," in *10th International Symposium on High-Temperature Metallurgical Processing*, 2019, pp. 371–378.

[92]   Thomas W. Hansen, Andrew T. Delariva, Sivakumar R. Challa, and Abhaya K. Datye,

"Sintering of catalytic nanoparticles: Particle migration or ostwald ripening?," *Acc. Chem. Res.*, vol. 46, no. 8, pp. 1720–1730, 2013, doi: 10.1021/ar3002427.

[93] Grant C. Wallace, Jerome P. Downey, Jannette Chorney, and Katie Schumacher, "Optimization of Process Parameters for the Synthesis of Mo2C on an Activated Carbon Matrix," in *11th International Symposium on High Temperature Metallurgical Processing*, 2020, pp. 715–724, doi: 10.1007/978-3-030-36540-0_64.

[94] Stephen R. Shatynski, "The thermochemistry of transition metal carbides," *Oxid. Met.*, vol. 13, no. 2, pp. 105–118, 1979, doi: 10.1007/BF00611975.

9. Appendix A: Chemical Characteristics of Commercially Available WC (H.C. Starck CS50 Grade)

Component	Mass Fraction Limit (wt % or ppm)
C_{total}	6.10 – 6.15%
C_{free}	0.05% (Max.)
Al	15 ppm (Max.)
Ca	15 ppm (Max.)
Co	25 ppm (Max.)
Cr	80 ppm (Max.)
Cu	10 ppm (Max.)
Fe	150 ppm (Max.)
Mo	25 ppm (Max.)
Na	10 ppm (Max.)
Ni	70 ppm (Max.)
Si	20 ppm (Max.)
S	10 ppm (Max.)
Oxygen Content	0.40%

10. Appendix B: HSC Input Data

Active species:	W		A23		v	W		

	A	B	C	D	E	F	G	H
1	Species	Feed	Activity	Amount	Initial	Initial	Add	Ad
2	Formula	Temperature	Coefficient	Unit	Amount	Amount	X-amount	Z-am
3		°C	f			%		
5	CH4(g)	25	1	kmol	800	79.9999976		
6	CO(g)	25	1	kmol	100	9.9999997		
7	CO2(g)	25	1	kmol	0.00001	0.000001		
8	H2(g)	25	1	kmol	100	9.9999997		
9	H2O(g)	25	1	kmol	0.00001	0.000001		
10	N2(g)	25	1	kmol	0.00001	0.000001		
11	AQUA		Mixture		300.00001	100	0	
12	H(+a)	25	1	kmol	200	66.66666444		
13	WO4(-2a)	25	1	kmol	100	33.33333222		
14	H2O	25	1	kmol	0.00001	3.33333E-06		
15	CARBIDE		Pure		2000.00002	100	0	
16	C	25	1	kmol	2000	99.999999		
17	WC	25	1	kmol	0.00001	0.0000005		
18	W2C	25	1	kmol	0.00001	0.0000005		
19	OXIDE		Pure		0.00002	100	0	
20	WO2	25	1	kmol	0.00001	50		
21	WO3	25	1	kmol	0.00001	50		
22	PURE		Pure		0.00001	100	0	
23	W	25	1	kmol	0.00001	100		

11. Appendix C: Experimental Results for the W-Carburization Statistical Model

Std	Time (h)	Temperature (°C)	Activated C Content (% AC)	Gas Composition (CH₄:H₂)	Rel Wt % WC (%)
1	6	850	20	2	72.1
2	8	850	20	2	73.0
3	6	950	20	2	81.9
4	8	950	20	2	84.4
5	6	850	50	2	61.8
6	8	850	50	2	70.5
7	6	950	50	2	69.1
8	8	950	50	2	69.5
9	6	850	20	8	69.3
10	8	850	20	8	79.1
11	6	950	20	8	93.8
12	8	950	20	8	86.9
13	6	850	50	8	74.9
14	8	850	50	8	81.8
16	8	950	50	8	79.9
17	7	900	35	5	78.7
15	6	950	50	8	65
18	7	900	35	5	78.9
19	7	900	35	5	79

12.   Appendix D: Additional Statistical Diagnostics for the W-Carburization Model

(Rel Wt % WC)^2.07

Current transform:
Power

Current Lambda = 2.07
Best Lambda = 2.07
CI for Lambda: (-1.61, 5.32)

Recommended transform:
None
 (Lambda = 1)

Box-Cox Plot for Power Transforms
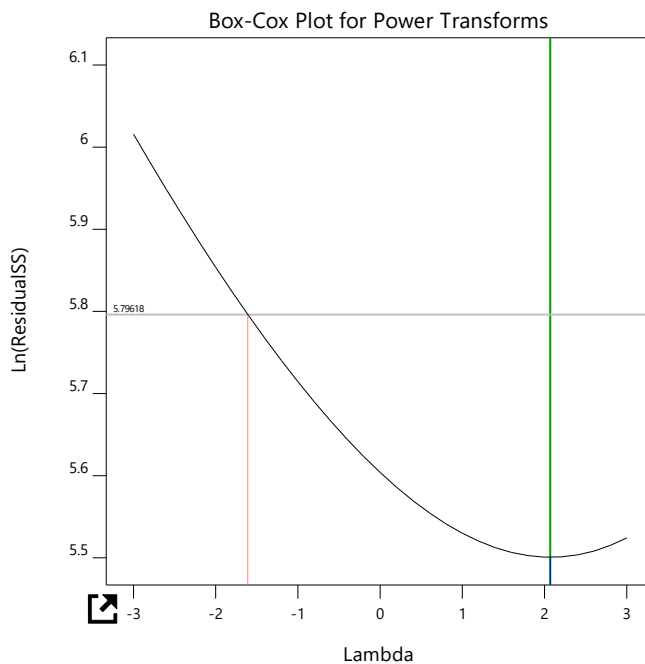
(Rel Wt % WC)^2.07

Color points by value of
Rel Wt % WC:

5097.368 ████ 12090.931

Residuals vs. Run
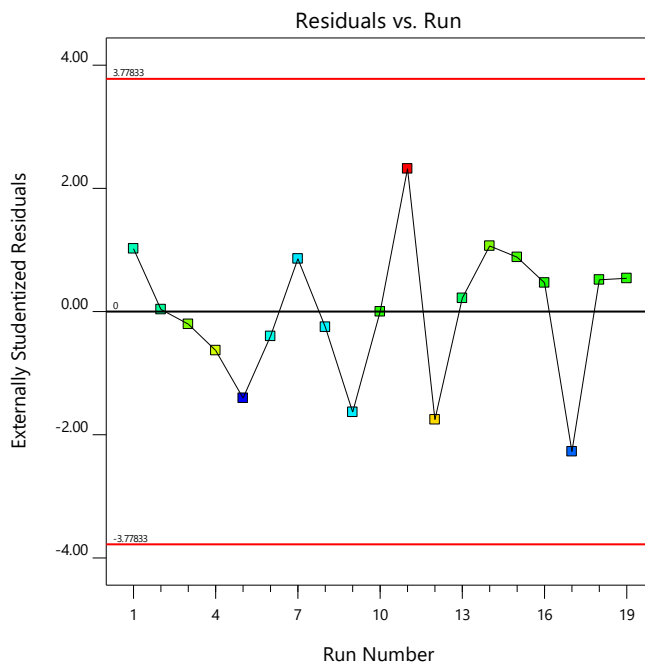
13. Appendix E: Experimental Data for the Mo-Carburization Statistical Model

Sample Name	Time (h)	Temperature (ºC)	Gas Composition ($CH_4:H_2$)	Mo_2C Content (wt %)
Mo_DM1	1	500	2.9	0
Mo_DM2	8	500	2.9	0
Mo_DM3	1	850	2.9	89.6
Mo_DM4	8	850	2.9	90.1
Mo_DM5	1	500	8	0
Mo_DM6	8	500	8	0
Mo_DM7	1	850	8	85.3
Mo_DM8	8	850	8	72.0
Mo_DM9	4.5	675	5	36.6
Mo_DM10	4.5	675	5	11.1
Mo_DM11	4.5	675	5	25.3

14. Appendix F: Additional Statistics for Mo-Carburization Model

Sqrt(Mo2C Content)

Current transform:
Square Root

Current Lambda = 0.5
Best Lambda = 0.39
CI for Lambda: (0.2, 0.57)
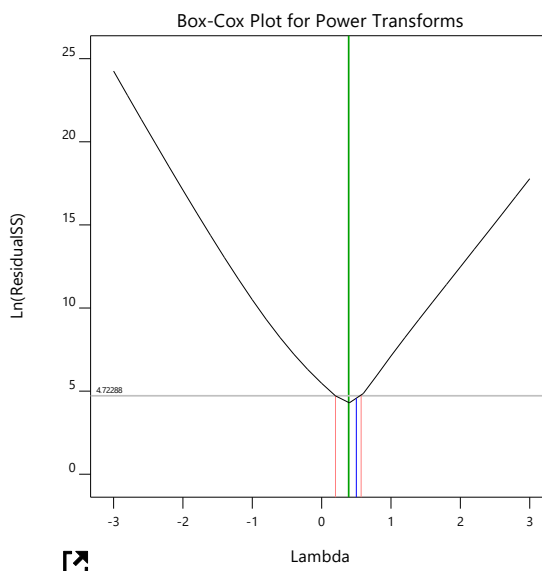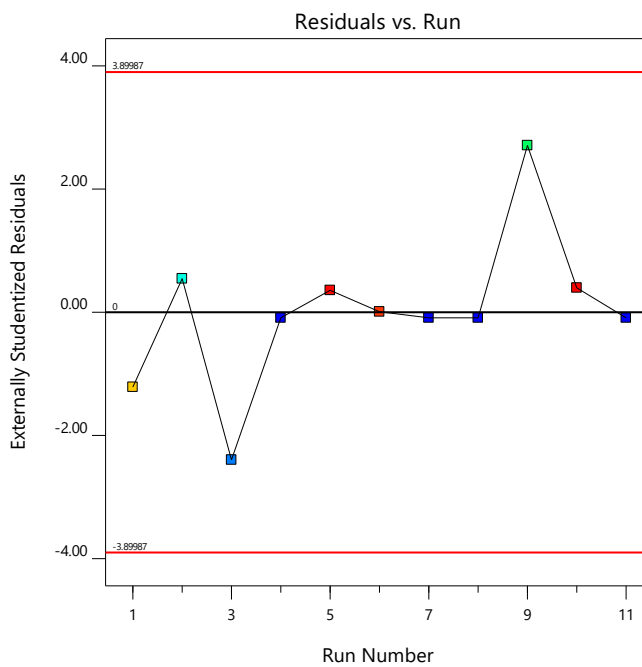
Recommended transform:
Square Root
 (Lambda = 0.5)

k = 0.0901
(used to make response
values positive)

Sqrt(Mo2C Content)

Color points by value of
Mo2C Content:
0.000 — 9.492

15. Appendix G: Experimental Data for the W-Adsorption Statistical Model

Std.	W Conc (mg/L)	Time (h)	Temp. (°C)	pH	W Loading (mg/L)	Na Loading (mg/L)	% W Loading (%)	% Na Loading (%)	W Loading (g W/g C)
1	998.799	1	20	2	998.447	437.135	99.9648	9.05797	0.0407167
2	19731.8	1	20	1.98	13408.4	1511.25	67.9533	15.9194	0.54438
3	1006.4	24	20	2.03	1006.05	987.761	99.9655	20.5469	0.0410067
4	19813	24	20	1.95	13214.2	1158.41	66.6945	12.1841	0.530238
5	992.432	1	60	2.03	991.73	486.949	99.9292	10.1333	0.0401452
6	19797.3	1	60	2.08	11537.3	1425.26	58.2771	14.9665	0.466799
7	984.265	24	59	2.03	983.544	653.457	99.9268	13.6822	0.0400106
8	19724.9	24	59	2.07	12478.5	1334.3	63.2629	14.0795	0.506128
9	1034.5	1	20	5.98	1033.97	708.488	99.9493	14.6061	0.0413383
10	19833.3	1	20	5.66	6361.85	1009.59	32.0766	10.5836	0.257019
11	1015.59	24	20	6.08	1012.01	875.717	99.648	17.9415	0.040521
12	19840.2	24	20	6.01	4938.96	917.44	24.8937	9.61734	0.199732
13	1008.46	1	60	6.04	999.718	711.992	99.1336	14.6678	0.0400687
14	19858.2	1	60	6.11	5088.62	1302.1	25.6249	13.6506	0.20558
15	1002.68	24	59	6.05	999.274	410.522	99.6608	8.53544	0.0403707
16	19867.5	24	58	5.74	6219.91	1661.62	31.3069	17.4141	0.250538
17	1001.12	12.5	38	4.16	991.725	599.837	99.0613	12.4369	0.039907
18	19773.7	12.5	40	4	6883.95	1170.92	34.8136	12.3386	0.278662
19	10453.9	1	39	4.14	5253.44	1298.33	50.2534	18.0525	0.211398
20	10452.6	24	38	4.03	5298.89	917.738	50.6947	12.7639	0.213333
21	10428.3	12.5	20	3.16	6066.32	1521.49	58.1716	21.1501	0.244837
22	10442.9	12.5	58	4.04	4536.08	875.483	43.4368	12.1788	0.182713
23	10431.5	12.5	38	2.11	7319.97	1280.12	70.1719	17.8396	0.295141
24	10508.1	12.5	38	5.82	3012.19	1436.26	28.6654	19.9019	0.12109
25	10467.9	12.5	37	4.23	5129.07	1386.46	48.9983	19.2411	0.206599
26	10463.2	12.5	37	4.07	5220.37	1063.21	49.8926	14.7717	0.210381
27	10489.9	12.5	38	3.75	6032.32	1413.62	57.506	19.5991	0.242741
28	10480.5	12.5	38	3.98	5813.88	1512.3	55.4735	20.9901	0.233951
29	10506	12.5	38	4.19	5173.63	1327.13	49.2443	18.4172	0.208394
30	10496.1	12.5	39	3.96	5417.31	1073.94	51.6127	14.9015	0.218209

16. Appendix H: Additional Statistical Diagnostics for the W-Adsorption Model

1/Sqrt(gW/gAC)

Current transform:
Inverse Sqrt

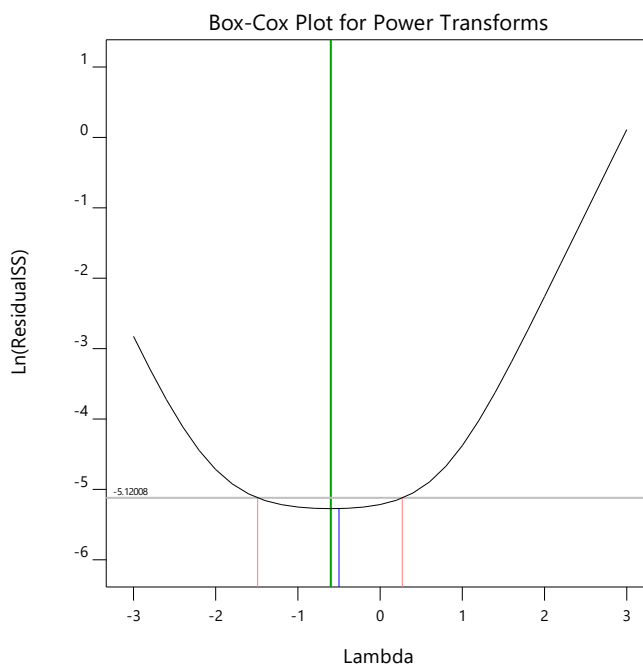Current Lambda = -0.5
Best Lambda = -0.6
CI for Lambda: (-1.49, 0.27)
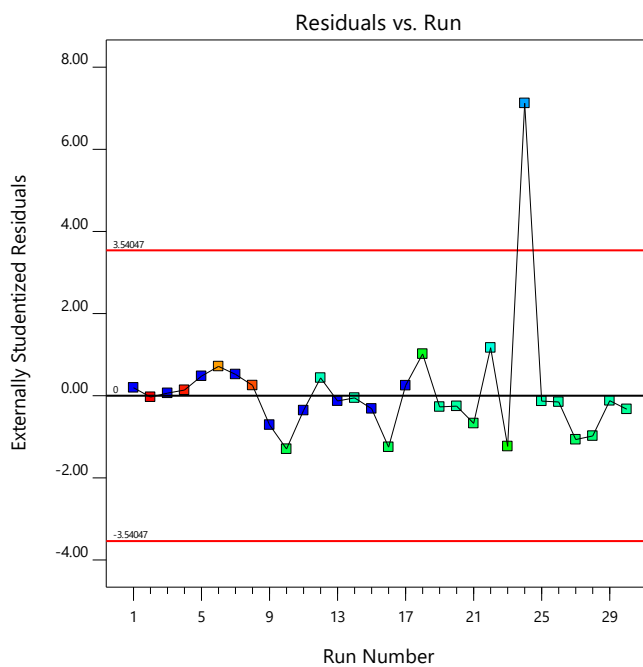
Recommended transform:
Inverse Sqrt
 (Lambda = -0.5)

Box-Cox Plot for Power Transforms

1/Sqrt(gW/gAC)

Color points by value of
gW/gAC:
5.006   1.355

Residuals vs. Run

17.   Appendix I: Experimental Data for the Mo-Adsorption Statistical Model

| Std.	Mo Conc. (mg/L)	Reaction Time (h)	pH	Temp. (°C)	Mo Loading (g Mo/g C)
1	1002.4	1	2.03	20	0.0397654
2	19419.1	1	2	20	0.357744
3	1002.61	24	2.06	20	0.0395808
4	19420.6	24	2.01	20	0.327978
5	1002.01	1	2.01	60	0.0397532
6	19381.5	1	2.01	60	0.320889
7	1007.55	24	2	60	0.0399796
8	19458.4	24	2	60	0.303812
9	1008.95	1	5.7	20	0.01205
10	19882	1	6	20	0.103658
11	1003.01	24	5.83	20	0.0131374
12	19902.6	24	6	20	0.0675585
13	1008.55	1	5.95	60	0.0131712
14	19802.5	1	6	60	0.0612651
15	996.817	24	5.95	60	0.0133488
16	19861.8	24	6	60	0.0947325
17	1005.78	12.5	3.97	40	0.0369149
18	19516.5	12.5	3.99	40	0.153116
19	10370.4	1	3.99	40	0.129843
20	10357.8	24	3.97	40	0.118347
21	10379.1	12.5	3.99	20	0.123548
22	10359.8	12.5	4.01	60	0.119116
23	10339.4	12.5	2.01	40	0.247473
24	10493.1	12.5	6.01	40	0.048334
25	10400	12.5	4	40	0.124772
26	10400	12.5	4	40	0.116409
27	10400	12.5	4	40	0.140086
28	10400	12.5	4	40	0.126734
29	10400	12.5	4	40	0.125347
30	10400	12.5	4	40	0.118185

18. Appendix J: Additional Statistical Diagnostics for the Mo-Adsorption Model
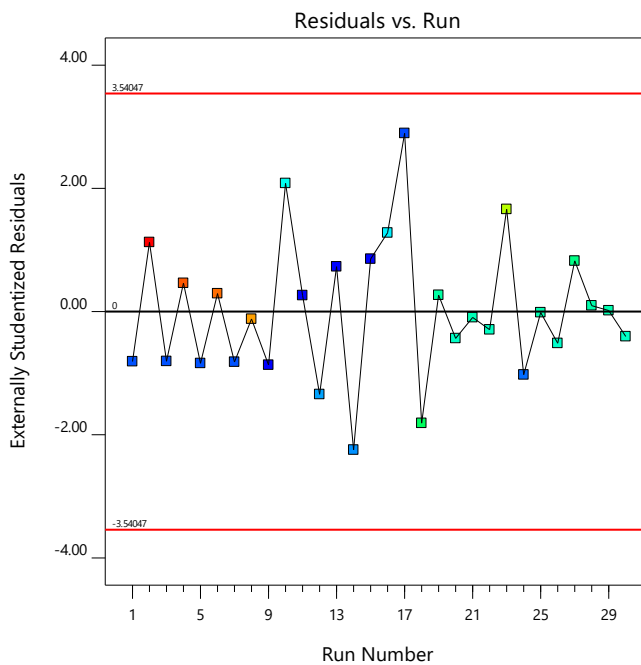
Log10(Mo Adsorbed)

Current transform:
Base 10 Log

Current Lambda = 0
Best Lambda = -0.05
CI for Lambda: (-0.18, 0.07)

Recommended transform:
Log
 (Lambda = 0)

Box-Cox Plot for Power Transforms
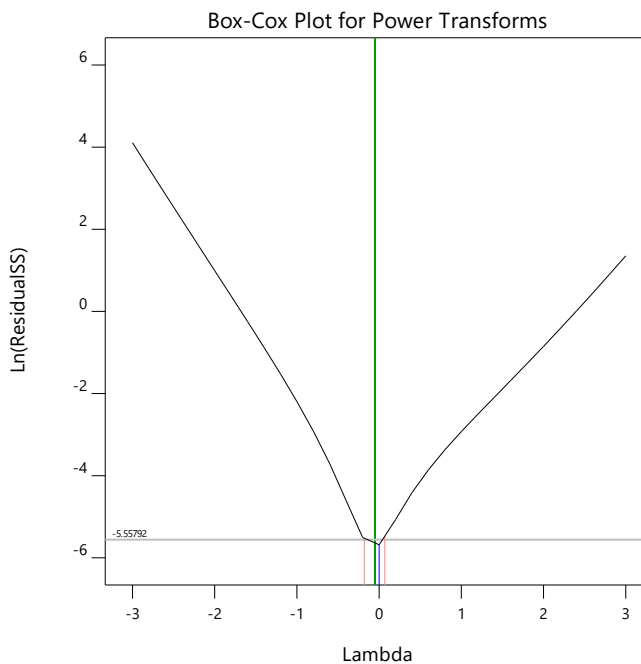
Log10(Mo Adsorbed)

Color points by value of
Mo Adsorbed:
-1.919 ▮▮▮ -0.446

Residuals vs. Run

19. Appendix K: Experimental Data for the Si-Adsorption Statistical Model

Std.	Reaction Time (h)	Temp. (°C)	Si Conc. (mg/L)	Si Loading (g Si/g C)
1	1	20	10000	0.0701048
2	12	20	10000	0.0454029
3	1	60	10000	0.0599353
4	12	60	10000	0.0456857
5	1	20	50000	0.167078
6	12	20	50000	0.29655
7	1	60	50000	0.222453
8	12	60	50000	0.164555
9	1	40	30000	0.0711782
10	12	40	30000	0.128567
11	6.5	20	30000	0.110764
12	6.5	60	30000	0.100874
13	6.5	40	10000	0.0384057
14	6.5	40	50000	0.408807
15	6.5	40	30000	0.094677
16	6.5	40	30000	0.099969
17	6.5	40	30000	0.115495
18	6.5	40	30000	0.107219
19	6.5	40	30000	0.0662402
20	6.5	40	30000	0.143785

20. Appendix L: Additional Statistical Diagnostics for the Si-Adsorption Model

1/Sqrt(gSi/gC)

Color points by value of
gSi/gC:

5.103 [color scale] 1.564

Residuals vs. Run
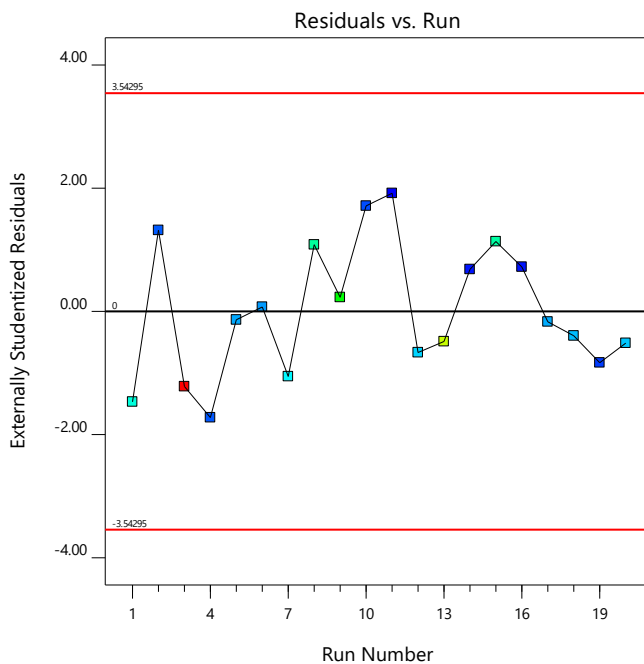
1/Sqrt(gSi/gC)

Current transform:
Inverse Sqrt

Current Lambda = -0.5
Best Lambda = -0.28
CI for Lambda: (-0.74, 0.15)

Recommended transform:
Inverse Sqrt
 (Lambda = -0.5)

Box-Cox Plot for Power Transforms